

Synthesis and Characterization of Core-Shell Metal Oxide Nanoparticles for Efficient Electrochemical Water Splitting

vorgelegt von

M.Sc. Hong Nhan Nong

aus

Tuyen Quang, Vietnam

Von der Fakultät II – Mathematik und Naturwissenschaften
der Technischen Universität Berlin
zum Erlangen des akademischen Grades

Doktorin der Naturwissenschaften

Dr. rer. Nat.

genehmigte Dissertation

Promotionsausschuss:

Vorsitzender: Prof. Dr. Roderich Süssmuth (TU Berlin)

Berichter: Prof. Dr. Peter Strasser (TU Berlin)

Berichter: Prof. Dr. Christina Roth (FU Berlin)

Tag der wissenschaftlichen Aussprache: 05.11.2015

Berlin 2016

Table of Contents

Table of Contents	i
Acknowledgment	iii
Abstract	iv
Zusammenfassung	v
1. Introduction	1
1.1. Electrocatalytic water splitting	1
1.2. OER mechanisms and rate determining steps in acid and alkaline conditions	6
1.3. Atomistic surface descriptors for the design of improved OER oxide catalyst materials	8
1.4. OER electrocatalysts in acidic environment - State of the art	12
1.5. Goal and objectives	14
2. Experimental Procedures	17
2.1. Synthesis procedures	17
2.1.1. Synthesis of mesoporous antimony-doped tin oxide (Meso-ATO)	17
2.1.2. Synthesis of supported Ir nanoparticles as benchmark catalysts	17
2.1.3. Synthesis of supported IrNi _x bimetallic nanoparticles using different methods	18
2.1.4. Optimizing conditions of polyol method for synthesis of supported IrNi _x nanoparticles	19
2.2. Structure and composition characterization	21
2.2.1. X-ray diffraction (XRD)	21
2.2.2. Inductively coupled plasma optical emission spectroscopy (ICP-OES)	22
2.2.3. Transmission electron microscopy (TEM)	22
2.2.4. Scanning transmission electron microscopy and energy dispersive X-ray spectroscopy (STEM-EDX)	23
2.2.5. X-ray photoelectron spectroscopy and X-ray absorption near edge structure (XPS-XANES)	23
2.2.6. High energy X-ray diffraction and atomic pair distribution functions (HE XRD-atomic PDFs)	25
2.3. Electrochemical characterization	27
2.3.1. Preparation of catalytic ink	28
2.3.2. Preparation of working electrode	29
2.3.3. Electrochemical protocols	29
3. Optimizing Synthesis Conditions of Supported Homogeneous IrNi _x Alloy Nanoparticles	35
3.1. Comparison of different methods for the synthesis of IrNi _x (nominal IrNi ₃) alloy nanoparticles	35
3.2. Impact of reaction conditions in polyol method based synthesis of IrNi alloy nanoparticles	37
3.3. Summary	42
4. Synthesis and Characterization of IrNiO _x Core-Shell Nanoparticles as Oxygen Evolution Electrocatalysts	43
4.1. Experimental	44
4.2. IrNi _x precursor alloys (PA-IrNi _x)	45
4.3. Preparation of dealloyed IrNi@Ir metallic core-shell nanoparticles ("D-IrNi _x ")	48

Table of Contents

4.4.	Preparation of SO-IrNi@IrO _x and DO-IrNi@IrO _x hybrid core-shell nanoparticles	51
4.4.1.	Electrochemistry of the oxidized core-shell nanoparticles	51
4.4.2.	XPS studies of PA-, SO-, and DO-IrNi _x nanoparticles confirm the metal-oxide hybrid core-shell structure hypothesis	53
4.5.	Electrochemical OER activity of IrNi@IrO _x core-shell nanoparticles	61
4.6.	Summary	65
5.	Oxide-Supported IrNiO _x Core-Shell Particles as Efficient, Cost-Effective, and Stable Catalysts for Electrochemical Water Splitting	67
5.1.	Structure evolution of IrNi _x /Meso-ATO precursor alloys under thermal treatment	68
5.2.	Structure confirmation of IrNiO _x core-shell nanoparticles	73
5.3.	Electrochemical catalytic activity and stability for the oxygen evolution reaction of core-shell IrNiO _x /Meso-ATO	77
5.4.	Summary	81
6.	Impact of the Support Materials on OER Activity and Structure Evolution of IrNiO _x Core-Shell Nanoparticles	83
6.1.	Structure evolution during electrochemical dealloying and oxidation	83
6.2.	Evolution of IrO _x shells upon electrochemical oxidation	90
6.3.	Impact of electrochemical pretreatment on the OER activity of IrNiO _x core-shell nanoparticles supported on different materials	95
6.4.	Summary	98
7.	IrNi _x Nanoparticles Supported on Mesoporous ATO-Impact of Ni Content in Precursor Alloys	99
7.1.	Precursor alloy IrNi _x nanoparticles supported on mesoporous ATO (PA-IrNi _x /Meso-ATO) with different Ni contents	99
7.2.	ATO supported IrNiO _x core-shell nanoparticles synthesized from precursor alloys with different initial Ni contents	104
7.2.1.	The surface electrochemistry of IrNiO _x core-shell nanoparticles	104
7.2.2.	Surface chemical state and composition of IrNiO _x core-shell nanoparticles after oxidation and OER tests	107
7.3.	Oxygen evolution reaction activities of the oxidized IrNi _x nanoparticles correlated to Ni content in the corresponding precursor alloys	113
7.4.	Summary	116
8.	Conclusions and Perspectives	117
8.1.	Conclusions	117
8.2.	Perspectives	119
	List of references	121
	List of publications during PhD	122
	Bibliography	123
	Abbreviations	I
	List of Figures	IV
	List of Tables	XI

Acknowledgment

I would like to express my sincere gratitude to my supervisor Prof. Dr. Peter Strasser for giving me the opportunity to do research in his group and for his guidance and continuous support during my Ph.D.

I would also like to thank Prof. Dr. Christina Roth, my second supervisor and Prof. Dr. Roderich Süßmuth, the chairman of my thesis committee, for their valuable and insightful feedback.

My sincere thanks go to Dr. Detre Teschner for the collaboration within the SPP 1613 project and for the XPS measurements and their detailed evaluation, to Prof. Dr Valeri Petkov for the HE XRD atomic PDFs analysis, to Dr. Elena Willinger for the collaboration regarding the STEM-EDX analysis. I would also like to thank Dr. Lin Gan, Dr. Rameshwori Loukrakpam Jalan and Mr. Manuel Gliech for acquiring TEM images and Dr. Hyung-Suk Oh for helping me with experimental aspects of oxide support material and synchrotron measurements.

I am also grateful to Mr. Arno Bergmann and Mr. Camillo Spöri for their help during synchrotron beamtimes and the correction of my thesis and to Ms. Vera Beermann for help with experiments during her internship. I would also like to thank Mrs. Annette Wittebrock for helping me order chemicals and lab wares, and Mrs. Astrid Müller-Klauke for measuring ICP-OES.

The Zentraleinrichtung für Elektronenmikroskopie (Zelmi) of the Technical University Berlin is acknowledged for their support with TEM technique. I would like to acknowledge financial support by the Ministry of Education and Training of The Socialist Republic of Vietnam (MOET) and the German Academic Exchange Service (DAAD). Financial support by the German Research Foundation (DFG) through grant STR 596/3-1 under the Priority Program 1613 is also gratefully acknowledged.

I would like to thank everyone at the Strasser's group for making my stay here a very pleasing and rewarding experience.

To Tobias Reier, my Chuột Ngọt, thank you for your invaluable support during my work, for helping me with the correction of the thesis and the translation of the abstract, for the encouragement, and for being always supportive and caring.

Lastly, I would like to thank my family - my parents and my sister - for being there for me through thick and thin.

Thank you!

Abstract

Electrocatalytic water splitting is expected to emerge as a key technology for the storage of excess electricity from renewable sources in form of hydrogen or for production of sustainable hydrogen fuel as part of a solar refinery. In particular, polymer electrolyte membrane (PEM) electrolyzers, owing to their high voltage efficiency, high current density, good partial loading range, compact system design, high gas purity and rapid system response, will likely play a critically important role to store excess electricity in form of hydrogen. However, high catalyst cost and limited catalyst durability of PEM electrolyzer electrodes, especially at the anode side, where the oxygen evolution reaction (OER) takes place, have long hindered a broader dissemination of PEM electrolyzers. Typical OER electrocatalysts for PEM electrolyzers make use of RuO_x and/or IrO_x as catalytically active components. In order to reduce the catalyst costs, non-noble metal oxides, such as SnO_2 , Sb_2O_5 , Ta_2O_5 , Nb_2O_5 , TiO_2 and SiO_2 , have been mixed with IrO_2 , allowing the reduction of the noble metal content without a significant decrease in the catalytic activity and electronic conductivity. However, the noble metal content in these types of OER catalysts still remains very high.

The overarching goal of this thesis is the rational design of oxide-supported IrNi_x nanoparticle catalysts with drastically reduced noble metal loadings for the electrocatalytic oxidation of water in acidic environments. In order to achieve this goal, different strategies were pursued: i) application of corrosion-resistant high surface-area supports, ii) design of IrM@IrO_x metal-oxide hybrid core@shell nanoparticle architectures, where M represents a non-noble metal that helps to tune the intrinsic electrocatalytic activity and lower the noble metal content alike. In this work, the synthetic conditions were optimized in order to prepare homogenous IrNi_x nano alloys with controlled composition as intermediate state for the synthesis of IrNi@IrO_x architectures. The IrNi_x and IrNi@IrO_x nanoparticles were comprehensively studied using a wide range of characterization techniques including powder X-ray diffraction (XRD), transmission electron microscopy (TEM), scanning TEM combined with energy dispersive X-ray spectroscopy (EDX), depth-resolved X-ray photoelectron spectroscopy (XPS), and high energy XRD coupled with atomic pair distribution functions (PDFs). The IrNi@IrO_x core-shell nanoparticles showed a $\sim 10x$ higher Ir-mass based activity at 250 mV overpotential compared to a rutile-type IrO_2 nanoparticle benchmark catalyst. Moreover, oxide supported IrNi@IrO_x nanoparticles provided an excellent stability under OER conditions demonstrated by a negligible degradation during a 20 hour stability test unlike various other Ir materials. Correlating the structural characteristics of the IrNi@IrO_x core-shell nanoparticles with their OER activity it is proposed that the lattice contraction is responsible for the exceptional reactivity.

Zusammenfassung

Die elektrokatalytische Wasserspaltung hat ein großes Potential für die Speicherung überschüssigen Stroms aus erneuerbaren Quellen in Form von Wasserstoff und kann so für die Produktion großer Wasserstoffmengen als Teil einer nachhaltigen Versorgung mit Treibstoffen dienen. Die vielversprechendste Technologie in diesem Zusammenhang ist der Polymer Elektrolyt Membran (PEM) Elektrolyseur, da sie eine hohe Spannungseffizienz aufweisen, große Stromdichten erlauben, einen großen Teillastbereich abdecken, eine kompakte Bauform besitzen, hohe Gasreinheiten liefern und über kurze Ansprechzeiten verfügen. Allerdings schränken zurzeit noch hohe Kosten und eine beschränkte Lebensdauer im Bereich der Katalysatoren die großflächige Verbreitung dieser Technologie ein. Dies gilt insbesondere für den Katalysator an der Anode, an dem die Sauerstoffevolutionsreaktion (engl.: Oxygen Evolution Reaction-OER) abläuft. Als aktive Komponenten für den Katalysator an der Anode werden üblicherweise RuO_x und IrO_x eingesetzt. Zur Senkung der Kosten wird dabei IrO_2 teilweise durch SnO_2 , Sb_2O_5 , Ta_2O_5 , Nb_2O_5 , TiO_2 oder SiO_2 substituiert, wobei die katalytische OER Aktivität und die elektrische Leitfähigkeit des Katalysators nicht signifikant verringert werden. Nichtsdestotrotz ist der Edelmetallanteil immer noch vergleichsweise groß.

Das übergeordnete Ziel dieser Arbeit ist die rationale Gestaltung und Optimierung von oxid-geträgerten nanopartikulären IrNi_x Katalysatoren mit drastisch reduziertem Edelmetallgehalt für die elektrokatalytische Oxidation von Wasser im sauren Milieu. Um dieses Ziel zu erreichen wurden die nachstehend genannten Strategien verfolgt: i) Einsatz eines korrosionsbeständigen oxidischen Trägermaterials mit großer Oberfläche, ii) Entwicklung von IrM@IrO_x Metalloxid Hybrid Kern@Schale Nanopartikeln, wobei M ein nicht edles Metall darstellt mit dessen Hilfe die intrinsische OER Aktivität gesteigert und gleichzeitig der Edelmetallgehalt des Katalysators gesenkt werden kann. In dieser Arbeit wurden die Bedingungen der IrNi_x Nanopartikelsynthese optimiert, um homogen legierte Nanopartikel mit kontrollierter Zusammensetzung als Zwischenstufe für die Synthese von IrNi@IrO_x Nanoarchitekturen zu erhalten. Die IrNi_x und IrNi@IrO_x Nanopartikel wurden durch eine Vielzahl von Techniken umfassend charakterisiert. In diesem Zusammenhang sind folgende Techniken besonders hervorzuheben: Röntgenbeugung, Transmissionselektronenmikroskopie, Rastertransmissionselektronenmikroskopie zusammen mit Energiedispersiver Röntgenspektroskopie, tiefenaufgelöste Röntgenphotoelektronenspektroskopie und hochenergetische Röntgenbeugung in Kombination mit atomaren Paarverteilungsfunktionen. Die IrNi@IrO_x Katalysatoren zeigten eine 10-fach höhere iridiumbasierte Massenaktivität bei einem Überpotential von 250 mV als ein reiner IrO_2 Referenzkatalysator. Darüber hinaus zeigten oxidgeträgerte IrNi@IrO_x Nanopartikel eine hervorragende Stabilität, sodass während eines 20-stündigen Stabilitätstests nur eine geringfügige Degradation zu beobachten war. Durch den Vergleich der strukturellen Eigenschaften der IrNi@IrO_x Nanopartikel mit deren OER Aktivität konnte die Gitterkontraktion als wahrscheinlichste Ursache für die erhöhte OER Aktivität identifiziert werden.

1. Introduction

1.1. Electrocatalytic water splitting

The world energy demand increased drastically in the past decades, whereby the energy is mainly supplied by fossil fuels and, to a small extent, nuclear power, while renewable energy holds less than 15% of total primary energy supply.¹ However, in the scenario of increasing air pollution and the greenhouse effect caused by combustion of unsustainable fossil fuels, challenges in the management of radioactive wastes and high risks of nuclear power plants, these electricity generation technologies should be restricted and eventually replaced by renewable technologies such as photovoltaics, wind turbines and hydropower. In Europe, electricity generated by renewable energies has been increasing remarkably over the past 10 years (Figure 1).² In 2014, renewable energies reached a share of about 42 % of the total electricity generation in Spain and Italy.

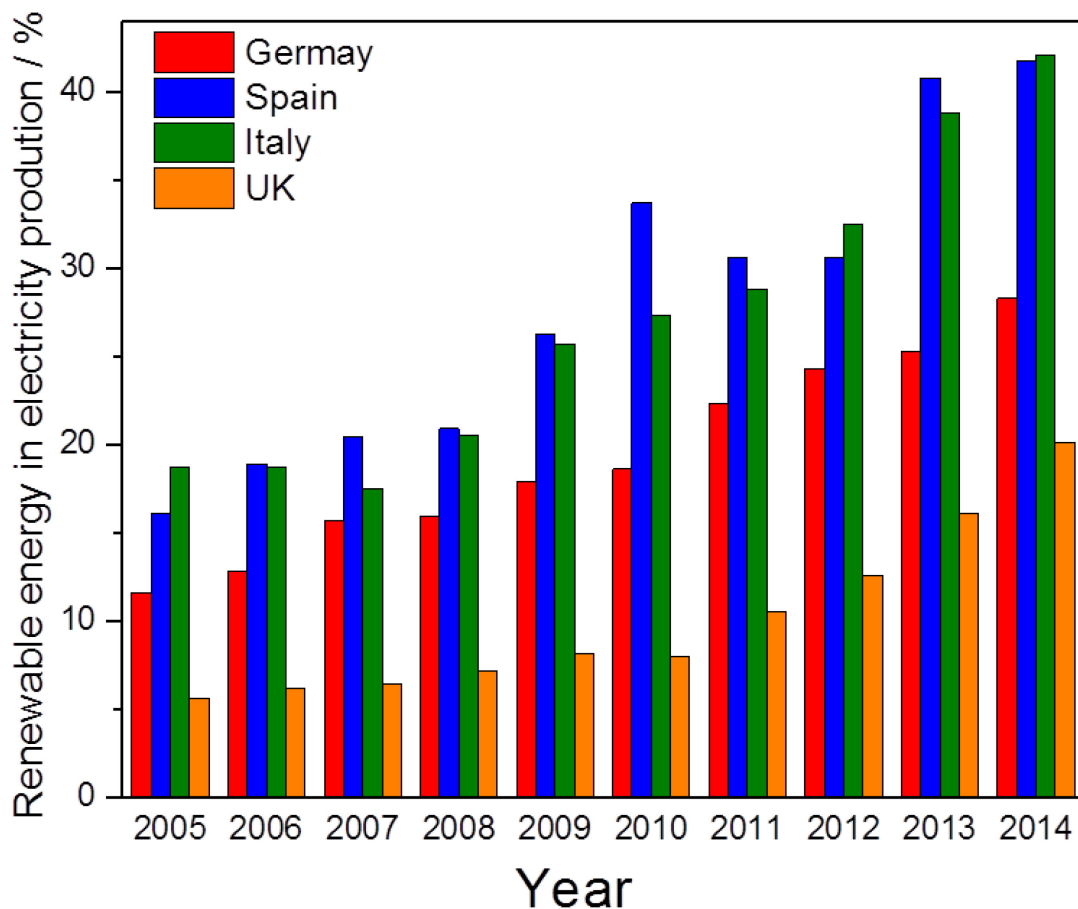


Figure 1. Percentage of renewable energy in the electricity production of some representative countries in Europe over the past 10 years. Data obtained from Ref. 2.

Particularly, in Germany, the Federal Government³ plans to gradually withdraw from nuclear power by 2022, cut greenhouse gas emissions by 40 % by 2020, and by at least 80 % by 2050. Renewable energies are, therefore, to be expanded to become the mainstay of the energy supply. The aim is to increase their share in gross final energy consumption from roughly 10 % in 2010 to 60 % in 2050. The share of renewable energies in electricity supply is supposed to grow up to a level of 80 % by 2050. Nevertheless, a significant disadvantage of most renewable energies is that they are intermittent on daily, seasonal and also regional scales with considerable variability in supply,⁴ and are not necessarily aligned with patterns of human energy demand,⁵ therefore, energy storage is focused on the development of renewable energies.

Hydrogen, a clean energy carrier, appears as a promising solution for energy storage. Hydrogen is emission-free at the point of final use and thus avoids the transport-induced emissions of both CO₂ and air pollutants, being a secondary energy carrier that can be produced from any (locally available) primary energy carrier (unlike other alternative fuels, except electricity), hydrogen can contribute to a diversification of automotive fuel sources and supplies.⁶ Hydrogen can be produced from electricity using electrocatalytic water splitting. Combined with renewable electric power generation technologies, electrocatalytic water splitting is expected to emerge as a low-emission method for storing excess electricity or for producing abundant quantities of sustainable hydrogen fuel as part of a solar refinery.⁷⁻¹²

In general, electrocatalytic water splitting can be carried out by alkaline, solid oxide, or polymer electrolyte membrane (PEM) electrolyzers.¹³ Advantages of alkaline electrolyzers include that they constitute a well established technology, the use of non noble metal catalysts, long-term stability and relative low cost; however, three major disadvantages associated with alkaline electrolyzers are their low partial load range, limited current density and low operating pressure. Solid oxide electrolysis, also using non noble metal catalysts, can produce hydrogen with high efficiency at low voltage under high pressure condition; nonetheless, solid oxide electrolyzer cells (SOECs) are still under development at the laboratory stage, and issues related to the durability of the ceramic materials at high temperature and long-term operation as well as to the system design need to be solved. Acidic PEM electrolyzers show many important positive aspects. PEM electrolyzers can operate at high current densities

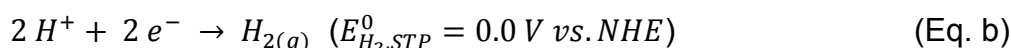
(more than 2 A cm^{-2}),¹⁴ which reduces the operational costs and potentially the overall cost of electrolysis. The low gas crossover rate of the polymer electrolyte membrane (yielding hydrogen with high purity), allows the PEM electrolyzers to work in a wide load range. The solid electrolyte allows a compact system design with strong/resistant structural properties, in which high operational pressures (equal or differential across the electrolyte) are achievable. PEM electrolyzers have some disadvantages, including high cost of components, especially noble metal catalysts and possibly low durability due to acidic corrosive environment. Nevertheless, considering the intermittency of renewable electricity production, a large partial load range is a crucial requirement for water electrolysis, which PEM electrolyzers can satisfy.

The overall chemical water splitting (ws) process¹⁵ is given by

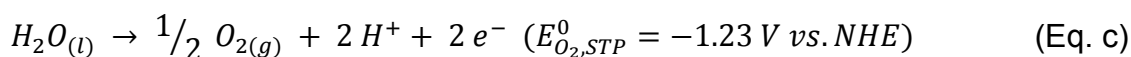


Under the standard temperature and pressure (STP) condition, the Gibbs free energy of the reaction in (Eq. a) is $+ 237 \text{ kJ mol}^{-1}$.

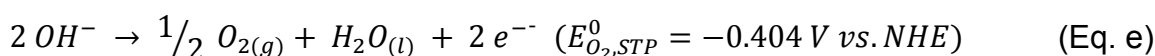
Water splitting can be divided into two half-cell redox reactions. In acidic environment, the reduction process at the cathode (hydrogen evolution reaction, HER) proceeds according to



while the (water) oxidation process (oxygen evolution reaction, OER) at the anode of the electrolyzer reads



In alkaline media, HER and OER proceed according to



At equilibrium, the minimum electrical energy required to split one mole of water under STP is related to the Gibbs free energy as

$$\Delta G_{ws,STP}^0 = -nFV_{rev,STP}^0 = -2 \cdot 96485 \frac{C}{mol} \cdot (-1.23 V) = 237 \frac{kJ}{mol} \quad (\text{Eq. f})$$

where

n is number of electrons transferred in the reaction, here $n = 2$, means two electrons are transferred per mole of water converted.

F is the Faraday constant ($96\,485\text{ C mol}^{-1}$)

$V_{rev,STP}^0$ is the cell voltage ($V_{rev,STP}^0 = E_{H_2,STP}^0 + E_{O_2,STP}^0$).

Here, the negative sign of the cell voltage indicates that the water splitting reaction does not occur spontaneously under STP condition. Considering only the absolute value of the cell voltage, $V_{rev,STP}^0 = 1.23\text{ V vs. NHE}$ at STP and is referred to as the reversible electrolysis cell voltage at STP.¹²

The challenge in electrocatalytic water splitting is the anodic multi-electron OER with its extremely sluggish surface kinetics on virtually all known materials. There can be only one electron transferred in each elementary step, so that all single-step reactions involve the transfer of only one electron.¹⁶ In order to form one molecule of O_2 in the OER, four electrons need to be transferred crossing the electrocatalytic interface, meaning that the OER occurs in at least four steps, requiring significant molecular reorganization and high activation energy, therefore, the OER exhibits an extremely small exchange current density, j_0 , near the reversible potential compared to, for instance, the HER even using the best known OER catalysts. To make matters worse, a reversible OER potential is typically not observed due to mixed electrode potentials. Mixed potentials form, when the electrode material suffers from faradaic anodic corrosion while a redox O_2/H_2O system is approaching equilibrium. A mixed rest (open circuit) potential is the result. An important consequence of the low reaction rate of the electrochemical OER is that the OER is currently considered as a major bottleneck, hampering the application of photo electrochemical devices to convert light into storable fuels.¹² This is why the understanding of this reaction process and the identification of an efficient and stable OER electrocatalyst is of utmost and primary importance in water splitting research.

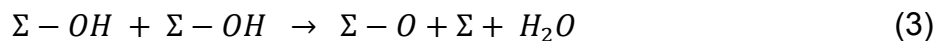
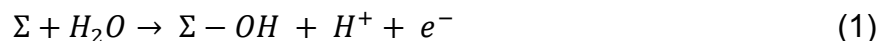
In principle, the electrochemical OER can be carried out under a wide range of pH conditions, from alkaline, neutral to acid environments.^{10,17-22} The selection of suitable materials as electrocatalysts is critically dependent on the pH of the

electrolyte. Performing OER under neutral conditions resembles the “green” concept of an artificial photosynthesis, however, creates challenges in terms of the ohmic losses inside the electrolyte due to the limited conductivity. Importantly, the formation of stoichiometric amounts of protons at the anode leads to a strong drop in local pH at the catalyst material which causes rapid corrosion. This is why during OER in neutral conditions a strong buffer system must be present in the electrolyte at all times, which is inconvenient compared to a polymer electrolyte solution. The biggest advantage of neutral OER conditions is the fact that they allow for the use of non-noble metal oxide catalysts. Cobalt based electrocatalysts were studied for OER in neutral conditions,²³⁻²⁶ while the catalysts have shown some degree of self-healing in the presence of the respective metal ion in the electrolyte, most non-noble metal catalysts also suffer from dissolution and degradation in metal free electrolytes. In alkaline media, Ni, Mn, Co, or Pb oxides with rutile-type,²⁷ perovskite-type^{28,29} and spinel-type structures have been considered in the past. The greatest disadvantage of these metal oxides is their high overpotential for OER, that is, their low electrocatalytic activity and efficiency.

Acidic conditions are, however, demanding in terms of electrode corrosion stability, requiring chemically and structurally stable catalysts. These materials must not only resist the harsh corrosive low pH condition, but also sustain the high applied overvoltage, especially at high current densities. This is why OER electrocatalysts for acidic conditions typically contain noble metal oxides, such as RuO_x or IrO_x . This makes them expensive and of limited sustainability. Since Beer’s early pioneering work,^{30,31} Ti-supported annealed films of bulk mixed-metal oxide of RuO_x , IrO_x and TiO_x have proven to be the most active and most stable OER electrocatalyst known to date. This family of bulk catalyst came to be known as the “dimensionally stable anode” (DSA). Suitable Ru-Ir mixed metal catalysts show overpotentials of only about 200 mV. Since the early days, DSAs represents the catalyst solution of choice for virtually all commercial PEM electrolyzers.³²⁻³⁵

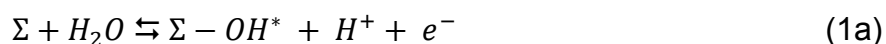
1.2. OER mechanisms and rate determining steps in acid and alkaline conditions

Despite much work on the OER, experimentally verified mechanistic models have remained scarce. Over the course of five decades, proposed mechanisms, conclusions as to the rate determining step, and experimental approaches have evolved very little. A severe hurdle to more direct atomic-scale insight in OER is the fact that reactive intermediates have largely eluded direct spectroscopic observations. Most early mechanistic work relies on classical current-potential-time analyses and the derived Tafel slopes. Tafel slopes are derived from semi-logarithmic potential current plots and have been frequently used to obtain information on the mechanism and the rate determining step of the overall half-cell reaction. An early mechanistic scheme of electrochemical water splitting on grounds of experiments on RuO₂ based electrodes in acidic environments reads³⁶



In this mechanistic hypothesis, Σ denotes a catalytically active surface site. Equations (1), (2), (4) on the one hand and (1), (3), (4) on the other hand represent parallel reaction pathways.

A very similar scheme was proposed for well-defined Ru(110) single crystal oxide surfaces.³⁷ RuO₂ (110) single crystals were reported with a near 60 mV/decade at low overpotential, while that of polycrystalline samples was reported to equal 40 mV. Based on that, an additional retarded chemical step according to:



was proposed to account for the larger experimental Tafel slopes on single crystals, where $\Sigma - OH^*$ indicated an intermediate surface complex undergoing some rearrangement before further oxidation, and the reaction sequence at low

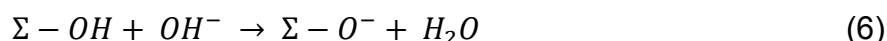
overpotential now being: (1a), (1b), (2), (4), with (1a) at equilibrium and (1b) being the rate determining step (rds). The 120 mV Tafel slope of RuO₂ (110) single crystals at high overpotential was explained based on a change of the rds within the same mechanism, i.e. from (1b) to (1a). The 40 mV Tafel slope of polycrystalline samples indicated that the reaction rate is limited by the transfer of the second electron, meaning the reaction sequence is (1), (2), and (4) with (1) is at equilibrium and (2) is the rds.

A very similar reaction mechanism to equations (1) - (4) was suggested for IrO₂.³⁸ A large number of studies considered the influence of the preparation conditions applied for Ru-oxide and Ru-Ir bimetallic oxide films on the OER activity and mechanism.^{27,39-43} Due to the lack of a single parameter controlling trends in OER activity or mechanism, many studies resorted to correlations of synthesis parameters, voltammetric charge q^* , OER activity (Tafel slopes), macroscopic structure, and morphology, often introducing somewhat arbitrary descriptors for catalyst morphology such as cracked, smooth, compact, or rough. Sol-gel type Ru oxide films followed the Tafel slope pattern of single crystals, while other synthetic methods resulted in deviating slopes.

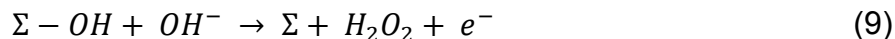
In alkaline electrolytes, non-noble metal oxides of Ni, Mn, Co, or Pb with rutile-type,²⁷ perovskite-type^{28,29,44}, and spinel-type structures were investigated in terms of their reaction mechanism for the OER. An initial discharge of hydroxide ions was agreed to be the first step in the reaction sequence



Subsequent steps leading to O₂ evolution are, however, controversial.⁴⁵ The scheme original proposed by Bockris⁴⁶ (the electrochemical oxide path) and later adopted with minor modifications by Krasilshchikov⁴⁷ and Damjanovic⁴⁸ suggested the step described by Equation (5) is followed by a deprotonation and subsequent discharge



or by a slow bond breaking of Σ -OH to form a peroxide species,



which subsequently decomposes into O₂.

Tafel slopes were calculated for different rds,^{46,28} resulting in Tafel slope of 2.3*2RT/F, 2.3*RT/F, 2.3*2RT/3F, or 2.3*RT/4F when (6), (7), or (8) is the rds, respectively. Similar to studies in acidic environments, synthesis conditions and Tafel slopes varied widely. Bockris presented a detailed study^{28,29,44} where he correlated the OER activity with a large number of microscopic and material specific parameters. His findings suggested that the catalytic OER activity correlated inversely with the surface bond energy of OH, from which he concluded that desorption of OH or oxygenated species may be the rate determining step in the OER under his conditions.

1.3. Atomistic surface descriptors for the design of improved OER oxide catalyst materials

A concept introduced by Ruetschi and Delahay,⁴⁹ later extended by Bockris^{28,29,44} and Trasatti²⁷ involves the hypothesis that a small set of catalyst parameters, for instance the molar enthalpy of formation of a metal oxide, could be a suitable descriptor to correlate with the OER reactivity to explain or predict observed activity trends. To investigate this hypothesis, Trasatti reported a volcano plot of the OER activity (overpotential) versus the enthalpy of formation of higher oxides (**Figure 2**) building on Sabatier's principle of balanced intermediate adsorption in catalysis.

According to Trasatti, on the one hand, oxides which are oxidized with difficulty are not very active because intermediates adsorb too weakly, then water discharge is the rate determining step in this case. On the other hand, oxides which are oxidized too easily are also not very active because intermediates are adsorbed too strongly; therefore, removal of oxygenated species is the rate determining step for these electrodes. The oxides nearest to the top of the volcano plot are RuO₂ and IrO₂, which are of the most active OER catalysts known to date.

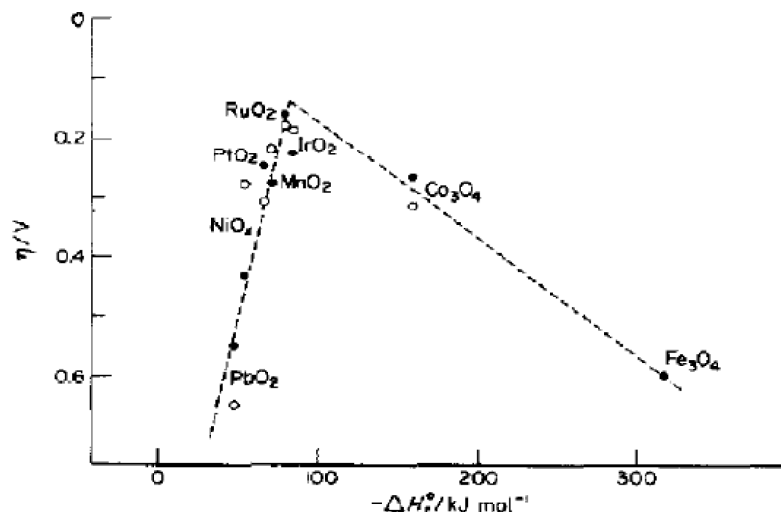
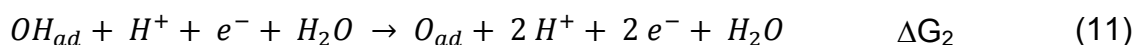
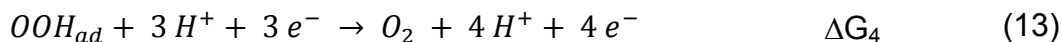


Figure 2. Electrocatalytic O₂ evolution activity at various oxide electrodes as a function of the enthalpy change associated with the transition of a lower to a higher oxide state. (○) Alkaline and (●) acid solutions are indicated. Reprinted from Ref. 27 with permission of Elsevier, copyright (1984).

More recently, the concept of microscopic molecular descriptors to understand and predict the surface catalytic reactivity was revisited, significantly extended, and improved using modern theoretical-computational tools.⁵⁰⁻⁵⁵ Norskov and his group identified band structure characteristics of catalysts, in particular the center energy of their metal projected d-bands, as a key factor describing and controlling trends in reactivity. The d-band center, in turn, directly controls the chemisorption energy of reactive intermediates. Hence, reactivity trends on different surfaces for a given reaction can be described and qualitatively understood in terms of trends in bond strength of adsorbed intermediates and surface atoms. Verified for selected heterogeneously catalysed processes⁵⁵ over a decade ago, the d-band model was recently verified for the electro reduction of oxygen (ORR), a key process at fuel cell cathodes, which is the reverse reaction of the OER.⁵⁶

Lately, Rossmeisl et al. reported density functional theory (DFT)-computational studies^{54,57-60} of OER reactivity trends on metal oxides in terms of oxygen chemisorption energies. The OER mechanism underlying his study consisted of four consecutive single-electron charge transfer steps according to





Rossmeisl analyzed the thermochemistry of this mechanism and created predictive OER reactivity volcano plots (Figure 3).⁵⁸

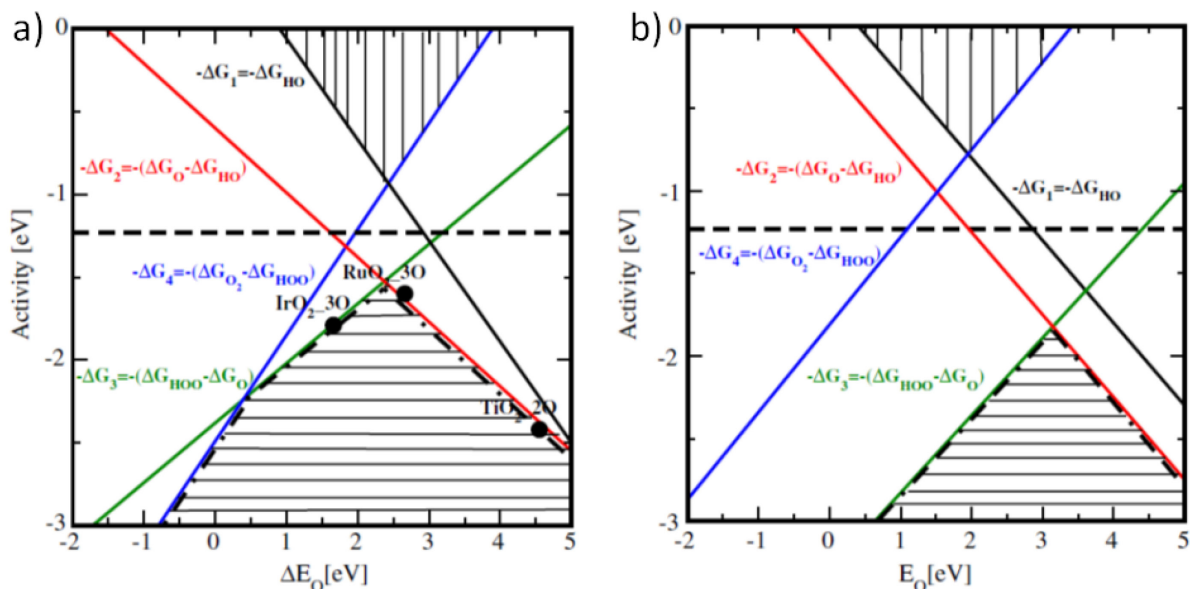


Figure 3. The theoretical activity of the four charge transferring steps of oxygen evolution is depicted as function of the oxygen binding energy for a) oxide surfaces, and b) metal surfaces. The y-axis is the activity defined as $-\Delta G_i$ of the different reaction steps, calculated from the linear relations: $\Delta G_1 = \Delta G_{HO} - \Delta G_{water} = \Delta E_{HO} + 0.35 \text{ eV}$, $\Delta G_2 = \Delta G_O - \Delta G_{HO} = \Delta E_O + 0.05 \text{ eV} - \Delta E_{HO} - 0.35 \text{ eV}$, $\Delta G_3 = \Delta G_{HOO} - \Delta G_O = \Delta E_{HOO} + 0.40 \text{ eV} - \Delta E_O - 0.05 \text{ eV}$, $\Delta G_4 = \Delta G_{O_2} - \Delta G_{HOO} = 4.96 \text{ eV} - \Delta E_{HOO} - 0.40 \text{ eV}$. The resulting volcano is indicated with dash-dot lines and the hatched areas. For the metal surfaces interaction with water has been taken into account, it results in a stabilization of HO and HOO compared to O. For the oxides the interaction with water is small. The best possible material would fall on the horizontal dashed line representing the equilibrium potential 1.23 eV. Optimal oxide catalysts are very close to this value (like RuO₂ and IrO₂). Reprinted from Ref. 58 with permission of Elsevier, copyright (2007).

Based on universal scaling relations between the chemisorption energies of the three principle adsorbates, Rossmeisl displayed the thermochemical activity of the overall OER process as a function of only one molecular chemisorption parameter. The predictions suggested that the overall OER rate is limited by reaction (12) for strong oxygen binding (green line), yet by reaction (11) for weak oxygen binding (red line). The intersection point of both lines represents the catalyst with the highest possible OER reactivity, under the given assumptions. RuO₂ is fairly close to the maximum of

the volcano plot, binding oxygen a little too weakly. IrO₂ is binding too strongly and is far off the top of the volcano. From Rossmeisl's analysis, oxide materials should exist with more favorable chemisorption energy and OER reactivity than RuO₂.

In order to optimize OER catalysts beyond the volcano plot, the scaling relations need to be broken. Breaking the scaling relations means that the binding energies of individual reactive intermediates can be tuned without affecting other intermediates. This can be achieved on RuO₂ by incorporation of Ni or Co into the surface, which activates a proton donor-acceptor functionality on the otherwise inactive oxygen bridge surface sites on the oxide surface.⁶¹ The activation of the bridge site introduces a second tunable parameter of the oxygen evolution process as the bridging O easily accepts and adsorbs hydrogen from the *OH and *OOH species, lowering the energies of these states compared to conventional ruthenia. The reactivity of the coordinatively unsaturated surface (cus) sites and the oxygen bridge site proton donor-acceptor potential are still weakly correlated via a hydrogen bond, which affects the oxidation potential of the bridge site if oxygen is present on the adjacent cus site. For Ni and Co modified ruthenia, the theoretical potentials for removing the proton from the bridging oxygen atoms in presence of adjacent molecular oxygen on the ruthenium cus site are more positive than if oxygen is absent on adjacent cus sites. The activation of the bridge sites (proton donor-acceptors) removes the problem of the universal free energy scaling of different intermediates, providing the necessary degree of freedom to approach a global optimum via a new reaction pathway. In essence, the activation of the bridge oxygens causes a change in the rds and eliminates energy scaling between oxygenated intermediates. This enhances the oxygen evolution activity of the modified catalysts significantly compared to conventional RuO₂ (**Figure 4**).

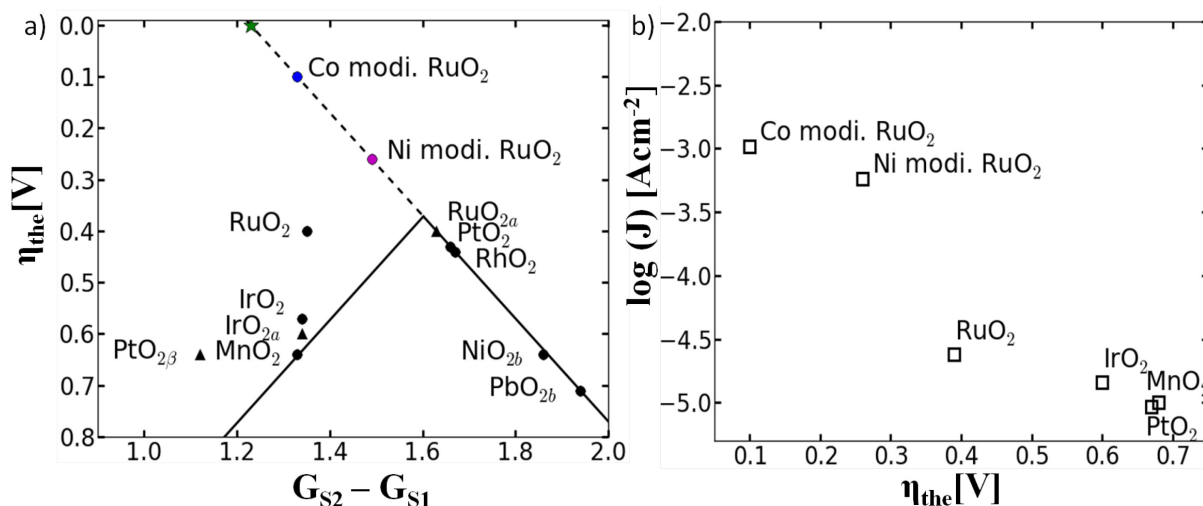


Figure 4. a) Volcano curve of the theoretical overpotential for the oxygen evolution process based on DFT calculations described in the literature⁵⁷ using the second charge transfer reaction as a descriptor. The star marks the position of an ideal catalyst, the magenta circle corresponds to Ni modified ruthenia and the blue circle to Co modified ruthenia, b) The correlation between the measured current density obtained at 1.6 V (vs. RHE) and the theoretical overpotential for different oxides. For the mixed oxides a concentration of Ni or Co of 0.05 is chosen to represent the activity per site for the cation modified ruthenia. Reproduced from Ref. 61 with permission of The Royal Society of Chemistry, copyright (2014).

From DFT calculations, OER overpotentials of Ni-modified and Co-modified RuO₂ are much lower than that of unmodified RuO₂ and stay far above the maximum of the volcano plot. Experimentally, the OER activity at 1.6 V vs. reversible hydrogen electrode (RHE) of Ni-modified and Co-modified RuO₂ is much higher than that of conventional RuO₂, following the predicted trend.

1.4. OER electrocatalysts in acidic environment - State of the art

As mentioned above, in acidic media, Ir and Ru are still materials of choice for OER electrocatalysts. Iridium has been preferentially used as an anode electrocatalyst because of its higher corrosion resistance under PEM water electrolyzer conditions compared to ruthenium, although its electrochemical OER activity is slightly lower than that of ruthenium.^{9,35,62} Mixing RuO₂ and IrO₂ should retain beneficial properties of both components, meaning high activity of RuO₂ and stability of IrO₂.^{62,63} In order to lower the noble metal content, non-precious oxides, such as SnO₂,⁴³ Sb₂O₅,⁶⁴ Ta₂O₅,⁶⁵ Nb₂O₅,⁶⁶ TiO₂⁶⁷ and SiO₂⁶⁸ were added to IrO₂, allowing the reduction of noble metal content without a significant decrease in the catalytic OER activity and

electronic conductivity.⁶⁹ For example, De Pauli and Trasatti⁴⁰ reported a volcano-type OER activity plot for IrO₂-SnO₂ mixed oxides with a maximum of ~4.5 mA cm² at 1.49 V vs. RHE (260 mV overpotential) in 0.5M H₂SO₄ for 40 % molar IrO₂-SnO₂ mixed oxide, higher than those of pure IrO₂ (~1.75 mA cm⁻²) and other IrO₂-SnO₂ mixed oxides. All samples were prepared by thermal decomposition of precursor salts (SnCl₂·2H₂O and IrCl₃·3H₂O). In contrast, according to Marshall et al.,²¹ Ir_xSn_{1-x}O₂ nanocrystals synthesized by reduction of metal precursors (H₂IrCl₆·4H₂O and SnCl₂·2H₂O) in ethylene glycol followed by thermal treatment in air showed decreased activity with increasing Sn content. The geometric OER activity of Ir_{0.8}Sn_{0.2}O₂ at 1.49 V vs. RHE was 1 mA cm⁻². Nanostructured ternary SnO₂-IrO₂-Ta₂O₅ composites showed a current density of 2 mA cm⁻² mg⁻¹ at 1.6 V in 0.1M HClO₄.⁷⁰

In the search of highly active and cost-effective OER electrocatalysts, the OER activities of many catalysts have been screened on a geometric current basis, where electrodes can have vastly different catalyst mass loadings and real active surface areas. This makes a direct comparison of catalysts on the basis of geometric currents challenging; therefore, real-surface-area-normalized and mass-normalized OER activities are required to establish meaningful activity descriptors that are capable for comparisons.⁷¹ For this purpose, Lee et al.⁷¹ reported OER activities of pure rutile RuO₂ and IrO₂ nanoparticles as OER benchmark catalysts. Quantitatively, the intrinsic OER activities of rutile-type IrO₂ nanoparticles are ~4 μA cm⁻²_{real} in acid and ~2 μA cm⁻²_{real} in alkaline, while rutile-type RuO₂ nanoparticles show OER activities of ~10 μA cm⁻²_{real} in acid and ~3 μA cm⁻²_{real} in alkaline at η = 0.25 V (1.48 V vs RHE). The noble metal-mass based OER activity of rutile-type RuO₂ and rutile-type IrO₂ were 14.5 A g⁻¹_{Ru} and 3.5 A g⁻¹_{Ir}, respectively at 250 mV overpotential in 0.1M HClO₄. More recently, H.S. Oh et al.⁷² reported a high OER activity of Ir nanodendrites, i.e. ~70 A g⁻¹_{Ir} at 280 mV overpotential and 693 A g⁻¹_{Ir} cm⁻² at 370 mV overpotential (1.6 V vs. RHE), which is a 2.3 times higher mass- and geometry- normalized current density as measured for colloidal IrO₂ (300 A g⁻¹_{Ir} cm⁻²).

1.5. Goal and objectives

The overarching goal of this thesis is the rational design, the preparation, characterization, and catalytic performance testing of oxide-supported IrNi_x nanoparticle catalysts with drastically reduced noble metal loadings for the electrocatalytic oxidation of water in acidic environments.

On the way to make PEM electrolyzer OER (RuO_x and IrO_x-containing) catalysts more efficient on both a thermodynamic and cost basis, new materials are sought with i) reduced noble metal content and ii) lowered overpotential (higher catalytic activity). In order to lower the noble metal content, nano-structuring of the active phase is a promising strategy which has attracted much attention.^{9,71,73-76} RuO₂ nanoparticles offer the lowest overpotentials for the OER, yet IrO₂ nanoparticles show comparable activities and are far more stable,⁹ hence, IrO₂ nanoparticles are of great interest. Still, the extremely scarce nature of Ir renders Ir nanoparticle architectures alone hardly viable, which is why novel strategies are critically needed to further reduce the amount of Ir in nanoparticle architectures.

Going beyond pure metal oxide electrocatalysts, other known correlations between structure and chemisorption can be invoked and combined with Rossmeisl's concepts to design improved OER catalysts. For instance, it is known that coordinatively undersaturated surface atoms at defects, steps or kinks of surfaces tend to show stronger chemisorption compared to terrace atoms.^{52,77-85} This is why Ru oxides nanoparticles with their higher degree of coordinative undersaturation should display increased chemisorption and should be shifted in direction of the top of the volcano plot. Conversely, mixing IrO₂ with oxide components which bind oxygen more weakly could result in a significant improvement in the OER activity on Ir mixed metal oxides. Tuning the d-band structure of RuO_x and IrO_x surfaces through non-noble transition metal atoms in underlying atomic layers is expected to be an effective way to enhanced catalytic activities.⁸⁴ This may be based on short-range electronic interaction or based on longer-range geometric strain effects.⁸⁶ IrO_x modified with transition metals might also break scaling relations and can be a promising method to improve the OER activity of Ir oxides.

Our strategies to minimize Ir content in OER catalysts involves the well-known use of suitable corrosion-resistant high surface-area supports that help to enhance the

surface active area due to high dispersion of the nanoparticles, and the design of IrM@IrO_x metal-oxide hybrid core@shell nanoparticle architectures, where M represents an inexpensive abundant transition metal that helps to tune the intrinsic electrocatalytic activity and lower the noble metal content alike. Moreover, concentrating Ir in thin shells of the nanoparticles reduces the required amount of the scarce metal significantly.

To achieve the overall goal mentioned above, this project involves a number of specific scientific objectives.

- **Objective 1:** Development of robust synthetic methods for homogeneously alloyed IrNi_x nanoparticles to be used as precursor alloys for the synthesis of metal-oxide hybrid core-shell catalysts. This involves the preparation of IrNi_x nanoparticles and the controlled deposition of nanoparticles on different support materials with controlled loading and composition of the nano alloys.
- **Objective 2:** Uncovering the correlation between physical properties and OER activity of supported IrNi@IrO_x core-shell catalysts aiming at an understanding of what controls the OER reactivity on the metal-oxide hybrid catalysts.
- **Objective 3:** Establish and utilize structure-activity-stability relationships of supported core-shell OER nanoparticle electrocatalysts.

In this work, we have optimized synthetic conditions for the preparation of homogenous IrNi_x nano precursor alloys with controlled composition and metal loading. The metal-oxide hybrid core-shell structure hypothesis was confirmed using a wide range of characterization techniques including powder XRD, TEM, STEM-EDX, depth-resolved XPS, and high energy XRD coupled with atomic PDFs. The final nanoparticle catalysts had a few atomic layers to ~1 nanometer of almost pure IrO_x representing the outer shell, while the inner core region became either increasingly metallic Ir and richer in Ni or hollow, depending on the size of the precursor alloy nanoparticles. The carbon supported core-shell nanoparticles showed **~10x higher Ir-mass based activity** at 250 mV overpotential compared to rutile-type IrO₂ nanoparticle benchmark catalysts⁷¹ mentioned above. The oxide supported core-shell catalysts also performed substantially more active, they offered an about **2x higher specific (intrinsic) activity**, and **5x higher Ir-mass based activity** compared to electrochemically oxidized Ir nanoparticles at a constant overpotential,

and allow, thus, a more energy-efficient oxygen evolution on a noble metal mass and an active site basis. The oxide supported IrNi@IrO_x nanoparticles showed **negligible degradation during 20 hours of stability test** unlike various Ir benchmark materials. Correlating the structural characteristics with the OER activity we proposed that the lattice contraction rather than Ni-promoted sites is responsible for the exceptional reactivity of the core-shell catalysts. The NiO phase segregation which occurred under certain conditions during the thermal treatment showed detrimental effects on the OER activity. Therefore, the annealing step plays an important role for oxide-supported nanoparticles in retaining high the activity of the supported core-shell nanoparticles.

2. Experimental Procedures

2.1. Synthesis procedures

2.1.1. Synthesis of mesoporous antimony-doped tin oxide (Meso-ATO)

1.28 g of tetradecylamine (TDA, 95.0 %, Sigma Aldrich) was added to a mixture of ethanol and water (65 mL of ethanol, Sigma Aldrich, and 160 mL of ultrapure water) and stirred for 3 hours at room temperature. 4.794 g of SnCl₄ (99.0%, Sigma Aldrich) and 0.48 g of Sb(CH₃COO)₃ (99.99%, Sigma Aldrich) were dissolved in 20 ml of ethanol and added to the TDA solution and further stirred for 1 hour. Afterwards, the mixture was poured in 200 ml ammonium hydroxide solution (1.5 mmol L⁻¹) and stirred for 1 hour. Subsequently, the solution was refluxed for 72 hours at 80 °C and then cooled down to room temperature. The yellow precipitate was separated from the solution by centrifugation at 5000 rpm for 10 min and then washed with ultrapure water and centrifuged 5 times. The as-prepared wet samples were transferred to a glass-lined stainless-steel autoclave and hydrothermally treated at 120 °C for 24 hours. In order to remove excess surfactant, the hydrothermal treated product was washed with ethanol for 5 times using centrifuge. After freeze drying for ~20 hours, the dried white powder was subsequently calcinated at 400 °C for 3 hours in air. The obtained mesoporous antimony-doped tin oxide was denoted as Meso-ATO.

2.1.2. Synthesis of supported Ir nanoparticles as benchmark catalysts

In a typical synthesis of Ir nanoparticles supported on high surface area carbon black (Vulcan® XC72, Cabot), 0.080 g of Ir(CH₃COO)₃ (≥ 48% wt. Ir, Chempur) was dissolved in 40 mL of a 0.15 M solution of sodium hydroxide in ethylene glycol. The solution was degassed with nitrogen for 5 min and then heated under nitrogen flow, stirring and reflux to 160 °C and kept at this temperature for 30 min. Afterwards the reaction mixture was cooled down rapidly using water bath. 192.2 mg of high surface area carbon Vulcan® XC72 were suspended in 30 ml of ultrapure water and 5 ml of concentrated CH₃COOH in a conical flask by sonication for 10 min. The Ir nanoparticle suspension was then added to this mixture, followed by stirring for 24 hours. The suspension was then centrifuged (10 min, 7700 rpm) and washed several times with ultrapure water. Accordingly, the collected Ir/support slurry then

was freeze dried for 20 hours. After freeze drying, the received powder is heat treated at 180 °C in N₂ atmosphere for 2 hours to remove remained organic substances, then the supported nanoparticles were annealed further at 400 °C for 4 hours in H₂ (4 vol% in Ar). The Ir nanoparticles supported on carbon are referred to as Ir/C.

Ir nanoparticles supported on mesoporous antimony doped tin oxide (denoted as Ir/Meso-ATO) or commercial ATO (denoted as Ir/com.-ATO) were synthesized similar to Ir/C, except that 192.2 mg of Meso-ATO or com.-ATO was introduced in the Ir(CH₃COO)₃ mixture before starting the reducing reaction, and the nanoparticles were annealed only at 180 °C in N₂ for 7 hours in order to avoid the reduction of ATO.

2.1.3. Synthesis of supported IrNi_x bimetallic nanoparticles using different methods

Conventional co-impregnation method. IrNi_x-IMP

0.060 g of Ir(CH₃COO)₃ (≥ 48% wt. Ir, Chempur) and 0.112 g of Ni(CH₃COO)₂·4H₂O (99.999%, Alfa Aesar) were dissolved in 3 mL of ultrapure water using sonication. 89.3 mg of Vulcan® XC72 were then added to the metal salt solution. The suspension was ultrasonicated for 5 min using a Branson Sonifier 150D with a power output of 7-8. The light viscous slurry was then frozen in liquid nitrogen for 15 min and freeze-dried (LABCONCO, Freezone 6) for 1 day. Finally, the dried, impregnated powder was annealed in a tube furnace at a temperature of 400 °C for 4 hours in 4 vol% / 96 vol% hydrogen/ argon atmosphere (quality of 5.0, supplied by AirLiquide) with a flow rate of 70 ml min⁻¹. Before the heating process started, the hydrogen/ argon had been previously flown through the quartz tube at room temperature for 30 minutes to remove oxygen. The temperature was increased to 400 °C and held at 400 °C for 4 hours to decompose the precursor anions. When the room temperature had been achieved, the reductive gas flow was stopped and switched to N₂ (quality of 5.0, supplied by AirLiquide) to prevent the carbon burning.

Polyol method in the presence of capping agents. IrNi_x-PO

0.075 g of Ni (II) acetate tetrahydrate (99.999%, Alfa Aesar), 0.113 g of 1,2-tetradecanediol (90%, Sigma Aldrich), 0.3 ml oleylamine (70%, Sigma Aldrich) and 0.3 ml oleic acid (99%, Alfa Aesar) were added to 30 ml dibenzyl ether (≥ 98%, Sigma Aldrich) in a three-neck flask. The mixture was then heated to 80 °C and

maintained at this temperature for 30 minutes under nitrogen flow to remove trace water. The temperature was then increased to reaction temperature 240 °C, and then 0.060 g of $\text{Ir}(\text{CH}_3\text{COO})_3$ ($\geq 48\%$ wt. Ir, Chempur) in a co-solvent was added to the reaction flask. The reaction solution was held at 240 °C for 1 hour and then cooled down to room temperature. 7 ml dichloromethane (99.8%, Merck) and 40 ml absolute ethanol (99.5%, Merck) were added to the reaction mixture. In parallel, 59.56 mg of Vulcan® XC72 carbon black was ultrasonically dispersed in 20 mL of toluene in a conical flask. The as-prepared IrNi_x nanoparticle suspension was added into Vulcan® XC72 carbon black in the toluene and stirred overnight. The supported catalyst was washed with absolute ethanol several times and collected by centrifuge at 7700 rpm for 10 minutes. The slurry then was freeze dried for 20 hours. To remove the remained surfactants, supported IrNi_x nanoparticles were heated at 180 °C in synthetic air (25% Vol. of O_2 and 75% Vol. of N_2) for 2 hours. Then N_2 was purged into the furnace for 1 hour at 180 °C to remove O_2 , after which the catalyst powders were further annealed at 400 °C in H_2 (4 vol% in Ar) for 4 hours.

Surfactant free or ethylene glycol method. IrNi_x -EG

0.060 g of $\text{Ir}(\text{CH}_3\text{COO})_3$ ($\geq 48\%$ wt. Ir, Chempur) and 0.112 g of $\text{Ni}(\text{CH}_3\text{COO})_2 \cdot 4\text{H}_2\text{O}$ (99.999%, Alfa Aesar) are dissolved in 40 ml of a 0.15 M solution of sodium hydroxide in ethylene glycol. The solution was degassed with nitrogen for 5 min and then heated under nitrogen flow, stirring and reflux to 160 °C and kept at this temperature for 30 min. Afterwards the reaction mixture was cooled down rapidly. 156.8 mg of Vulcan® XC72 were suspended in 70 mL of ultrapure water and 10 ml of concentrated acetic acid in a conical flask using sonifier. Nanoparticle suspension was then added to carbon suspension under stirring. The mixture was stirred overnight, followed by centrifugation and washing with ultrapure water. The collected Ir-Ni/support slurry then is freeze dried for 24 hrs. The received powder is heat treated in the tube furnace for 2.5 hrs at 250 °C under nitrogen atmosphere.

2.1.4. Optimizing conditions of polyol method for synthesis of supported IrNi_x nanoparticles

In a typical synthesis of IrNi_3 nanoparticles using the polyol method, 0.112 g of $\text{Ni}(\text{CH}_3\text{COO})_2 \cdot 4\text{H}_2\text{O}$ (99.999% Alfa Aesar), 0.169 g of 1,2-tetradecanediol (90%, Sigma Aldrich), 0.45 ml oleylamine (70%, Sigma Aldrich) and 0.45 ml oleic acid (99%, Alfa Aesar) were added to 45 ml dibenzyl ether ($\geq 98\%$, Sigma Aldrich) in a

three-neck flask. The mixture was then heated to 80 °C and maintained at this temperature for 30 minutes under nitrogen flow to remove trace water. The temperature was then increased to T °C (reaction temperature), and then 0.060 g of Ir(ac)₃ (≥ 48% wt. Ir, Chempur) was added to the reaction flask. The reaction solution was held at T °C for 1 hour and then cooled down to room temperature. 10 ml dichloromethane (99.8%, Merck) and 60 ml absolute ethanol (Merck) were added to the reaction mixture. In order to get the other desired Ir : Ni molar ratios in final products, the initial Ni and Ir precursor ratios were changed accordingly.

The as-synthesized IrNi_x nanoparticles were then supported on high surface area carbon to be used as electrocatalysts. In brief, a certain amount of Vulcan® XC72 carbon black (amount of carbon was calculated in order to obtain nominal Ir loading of 20 wt. %) was ultrasonically dispersed in 30 mL of toluene in a conical flask. After that, the as-prepared IrNi_x nanoparticle suspension was added into Vulcan® XC72 carbon black in the toluene and stirred overnight. The supported catalyst was washed with absolute ethanol several times and collected by centrifuge at 7700 rpm for 10 minutes. The wet sample then was freeze dried for 20 hours. The dried powder was then undergone an annealing protocol. First, to remove the surfactants, supported IrNi_x nanoparticles were heated at 180 °C in synthetic air (25% Vol. of O₂ and 75% Vol. of N₂) for 2 hours. Then N₂ was purged into the furnace for 1 hour at 180 °C to remove O₂, after which the catalyst powders were further annealed at 400 °C in H₂ (4 vol% in Ar) for 4 hours in order to reduce possible oxidized Ni on the surface and enhance the atomic mixing of Ni and Ir.

In order to optimize the reaction conditions for polyol method, first we synthesized IrNi nanoparticles at different reaction temperatures T °C (T = 200 °C, 220 °C, or 240 °C). Furthermore, effects of different co-solvents for dissolution of Ir(CH₃COO)₃ precursor, including 1,2-dichlorobenzene, dimethylacetamide (DMA), and N-methyl-2-pyrrolidone (NMP) were also investigated. Composition and structure of obtained nanoparticles correlated to synthetic conditions were compared in order to find out the most suitable conditions for synthesis of homogeneous IrNi alloyed nanoparticles.

IrNi_x nanoparticles supported on mesoporous antimony doped tin oxide (IrNi_x/Meso-ATO) were synthesized similar to IrNi_x/C with optimized conditions, except that Meso-ATO was introduced in the Ni(CH₃COO)₂.4H₂O mixture before starting the reducing reaction. The annealing protocol applied for IrNi_x/Meso-ATO was different from

IrNi_x/C in order to avoid reducing of the oxide support (Meso-ATO). In particular, to remove the surfactants, Meso-ATO supported IrNi_x nanoparticles were treated at 180 °C in synthetic air (25% Vol. of O₂ and 75% Vol. of N₂) for 2 hours. Then N₂ was purged into the furnace for 1 hour at 180 °C to remove O₂, after which the catalyst powders were further annealed at T °C in N₂ for 4 hours (T = 180, 250, 300, 400, or 500 °C) in order to investigate the impact of the thermal treatment on structure and OER activities of the oxide supported catalysts.

The Ir metal loading in all supported catalysts was controlled to be ~ 20 wt% Ir by adjusting the nominal weight ratio of Ir to the support (or support and Ni, in case of IrNi alloys). The actual Ir metal loadings and Ni/Ir ratios in the as-prepared materials were then evaluated by ICP-OES measurements.

2.2. Structure and composition characterization

2.2.1. X-ray diffraction (XRD)

X-ray diffraction is the elastic scattering of X-ray photons by atoms in a periodic lattice.⁸⁷ The scattered monochromatic X-rays that are in phase give constructive interference. **Figure 5** illustrates how diffraction of X-rays by crystal planes allows one to derive lattice spacings by using the Bragg relation:

$$n\lambda = 2d\sin\theta; \quad n = 1, 2, \dots \quad (14)$$

where

λ is the wavelength of the X-rays

d is the distance between two lattice planes

θ is the angle between the incoming X-rays and the normal to the reflecting lattice plane

n is an integer called the order of the reflection.

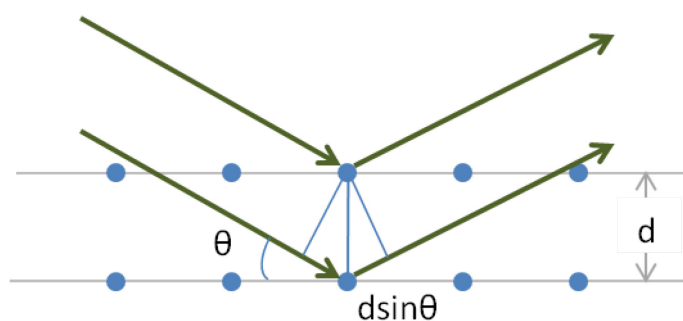


Figure 5. Schematic visualization of the Bragg equation.

If one measures the angles under which constructively interfering X-rays leave the crystal, the Bragg relation gives the corresponding lattice spacings, which are characteristic of a given compound.

XRD profiles were measured in Bragg-Brentano geometry in a D8 Advance X-ray diffractometer (Bruker AXS) using a Cu K α source, variable divergence slit, and a position sensitive device as detector. Data were collected in a 2θ range of 20° to 95° with an increment of 0.05° , a measuring time of 5 s per step, and a sample rotation rate of 15 rotations per minute.

2.2.2. Inductively coupled plasma optical emission spectroscopy (ICP-OES)

Sample preparation. 8 to 10 mg of the as-prepared catalyst was balanced in a closable quartz tube, afterward, 30 to 40 mg of NaClO₃ was added to the catalyst, followed by adding of 8 mL concentrated HCl 36%. The tube was closed with an acid resistant cap and treated in a microwave at 180 °C, upper limited pressure 18 bars for 20 minutes. The dissolved sample was cooled down, filtered and diluted with ultrapure water to get finally 500 mL solution. 10 mL of the final solution was transferred to a sample tube and measured by ICP-OES.

Compositional analysis was performed using a 715-ES-inductively coupled plasma (ICP) analysis system (Varian). The standard concentrations were 1, 2, 4 and 6 ppm for Ir and Ni. The chosen wavelengths for concentration determination were 212.681, 224.268, 236.804, 254.397, and 263.971 nm for Ir and 216.555, 221.648, 222.295, 227.021, 230.299, and 231.604 nm for Ni.

2.2.3. Transmission electron microscopy (TEM)

TEM micrographs were acquired using a FEI TECNAI G² 20 S-TWIN equipped with LaB6 cathode and GATAN MS794 P CCD camera. The microscope was operated at

an acceleration voltage of 200 kV. In order to prepare TEM samples, the catalyst powders were suspended in ethanol using sonifier to form a grayish suspension; then the suspension was pipetted onto a carbon coated copper grid (400 mesh, Plano). Particle size distributions were determined by measuring around 200 particles using the ImageJ 1.46 software (U.S. National Institutes of Health).

High-resolution transmission electron microscopy (HRTEM) micrographs were acquired using a FEI TITAN 80-300 electron microscope (300 kV).

2.2.4. Scanning transmission electron microscopy and energy dispersive X-ray spectroscopy (STEM-EDX)

Scanning transmission electron microscopy (STEM) and energy dispersive X-ray spectroscopy (EDX) line analysis discussed in chapter 4 were performed in FEI TITAN 80-300 electron microscope (300 kV) equipped with an image corrector (CEOS) and a high-angle annular dark field (HAADF) detector. The point resolution is 0.14 nm in HAADF-STEM mode. EDX spectra were collected across individual nanoparticle with drift correction at an acquisition time of 1-2 min/spectrum.

High-resolution STEM and elemental mapping discussed in chapter 5 were performed using a Jeol JEM-ARM200CF. The JEM-ARM200CF is a probe aberration corrected 200 kV STEM/TEM with a cold field emission source with 0.35 eV energy resolution. For HAADF imaging at 200 kV this instrument has a resolution of less than 0.08 nm.

2.2.5. X-ray photoelectron spectroscopy and X-ray absorption near edge structure (XPS-XANES)

X-ray photoelectron spectroscopy (XPS) is among the most frequently used techniques in catalysis.⁸⁸ It yields information on the elemental composition, the oxidation state of the elements and in favorable case on the dispersion of one phase over another. XPS is based on the photoelectric effect, in which an atom absorbs a photon of energy $h\nu$; next a core or valance electron with binding energy E_b is ejected with kinetic energy E_k (**Figure 6**):

$$E_k = h\nu - E_b - \varphi \quad (15)$$

where

E_k is the kinetic energy of the photoelectron

h is the Planck's constant

ν is the frequency of the exciting radiation

E_b is the binding energy of the photoelectron with respect to the Fermi level of the sample

ϕ is the work function of the spectrometer.

After the photoelectron ejection, the atom/ion is at the (n-1) state and has an electron hole at its core shell. Accordingly, one electron of an outer shell will drop into that core hole to minimize the energy of the system. The energy released by this relaxation process is either emitted as X-ray photon (X-ray fluorescence) or transferred to another outer electron leaving the atom/ion as Auger electron (**Figure 6**). If the X-ray photon energy and the work function of the spectrometer are known and the kinetic energy is measured by the spectrometer one can easily calculate the binding energy of the photoelectron.

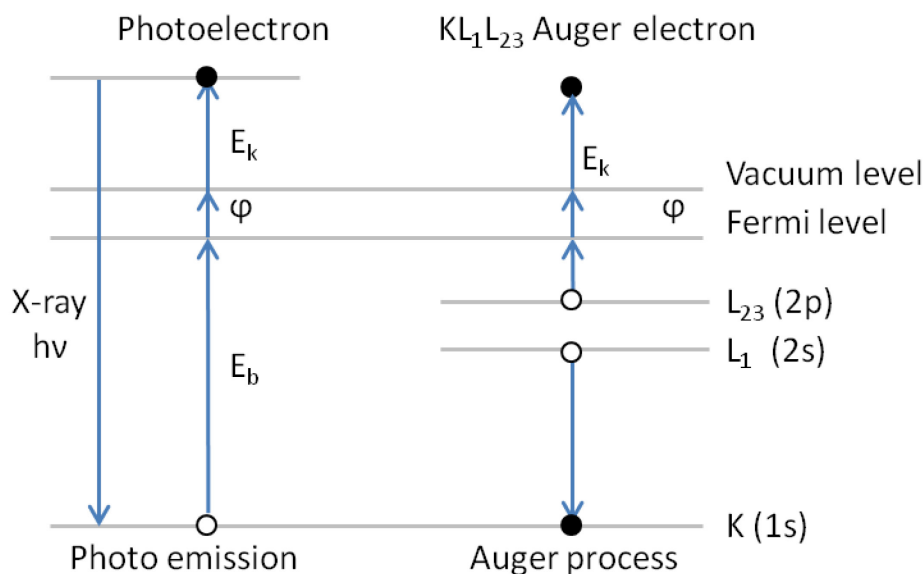


Figure 6. Photoemission and the Auger process. Left: An incident X-ray photon is absorbed and a photoelectron emitted. Measurement of its kinetic energy allows one to calculate the binding energy of the photoelectron. The atom stays behind as an unstable ion with a hole in one of the core levels. Right: The excited ion relaxes by filling the core hole with an electron from a higher shell. The energy released by this transition is taken up by another electron, the Auger electron, which leaves the sample with an element-specific kinetic energy. In Auger spectroscopy a beam of energetic (2-5 keV) electrons creates the initial core holes. Reproduced from Ref. 88 with permission of John Wiley and Sons, copyright (2007).

Sample preparation. To prepare the catalytic ink, 5 mg of catalyst powder was suspended in 3.980 mL of ultrapure water (Millipore, 18 M Ω), 1.000 mL of isopropanol and 20 μ L of 5 wt% Nafion[®] perfluorinated resin solution (Sigma Aldrich). The mixture was ultra sonified for 15 min (with carbon supported catalysts) or for 30 min (with ATO supported catalysts) using a Branson sonifier to form a uniform ink. Glassy carbon (GC) wafers (~10 mm x 10 mm) were used as substrate for the catalyst films. The GC wafers were polished manually in two steps: first step with Buehler "Alpha micropolish 1" solution on a Nylon sheet and second, followed by rinsing with ultrapure water, and the second step with Buehler "Alpha micropolish 0.05" solution on a Microloth[®] sheet. Finally the GC wafers were cleaned with ultrapure water and acetone before use. 10 μ L of catalyst ink was pipetted onto GC substrate and dried at 60 °C for 7 minutes. The pipetting and drying step was repeated 10 times. The final films contain about 0.1 mg of the catalyst powder.

IrNi_x catalysts were characterized by X-ray photoelectron (XPS) and X-ray absorption near edge structure (XANES) at the ISSS beamline of the synchrotron facility BESSY of the Helmholtz-Zentrum Berlin. A detailed description of the setup can be found elsewhere.⁸⁹ Samples were mounted onto a sapphire sample holder and introduced into the spectrometer. The soft X-ray absorption spectra of the Ni L_{2,3} edge were recorded in the total electron yield mode. Both XANES and XPS experiments were carried out at room temperature in ultra-high vacuum (UHV). To calculate elemental ratios, the peak areas of Ir 4f, Ni 2p and O 1s were corrected considering the photon flux and tabulated cross sections.⁹⁰ A depth dependent experiment was performed also to estimate the distribution of metallic and oxidized Ir as a function of information depth. To do so, the Ir 4f core level was recorded at various photon energies yielding electron kinetic energies as 210, 550 and 1200 eV.

2.2.6. High energy X-ray diffraction and atomic pair distribution functions (HE XRD-atomic PDFs)

High energy X-ray diffraction (HE XRD) and atomic pair distribution function (PDF) analysis can yield good knowledge of the atomic ordering in nanocrystalline materials exhibiting any degree of structure coherence and periodicity. Diffraction data at high wave vectors (~20 \AA^{-1} and higher) can be obtained using X-rays of short wavelength, i.e. high energy, which can be obtained from synchrotron or laboratory source.⁹¹

The frequently used reduced atomic PDF, $G(r)$, gives the number of atoms in a spherical shell of unit thickness at a distance r from a reference atom as follows:

$$G(r) = 4\pi[\rho(r) - \rho_0] \quad (16)$$

where

$\rho(r)$ and ρ_0 are the local and average atomic number density, respectively
 r is the radial distance.

$G(r)$ is a one-dimensional function that oscillates around zero and shows positive peaks at distances separating pairs of atoms, i.e. where the local atomic density exceeds the average.

The negative valleys in $G(r)$ correspond to real space vectors lacking atoms at either of their ends. $G(r)$ is the Fourier transform of the experimentally observable total structure function, $S(Q)$

$$G(r) = \frac{2}{\pi} \int_{Q=0}^{Q_{max}} Q [S(Q) - 1] \sin(Qr) dQ \quad (17)$$

where

Q is the magnitude of the wave vector defined as $Q = 4\pi \sin(\theta) / \lambda$, where θ is half of the angle between the incoming and diffracted synchrotron X-ray beams and λ is the wavelength of the X-rays used.

The total structure function was obtained from diffraction patterns. The diffraction patterns were corrected for experimental artifacts such as background scattering, absorption, Compton scattering and others, normalized in absolute electron units and reduced to structure factors, $S(Q)$.

In the present experiments HE XRD were carried out at beamline 11-ID-C at the Argonne National Laboratory using X-rays with wavelength of 0.11165 Å. Scattering intensities were collected with large area detector. The as-prepared sample powders, including supported nanoparticles and pure support materials (carbon or antimony doped tin oxide) were inside glass capillaries 1.5 mm in diameter.

Preparation of electrochemically treated samples: First, the catalyst ink was prepared as described in XPS sample preparation. Carbon sheets (AvCarb Paper P50T from Fuel Cell Store) were used as substrate for the catalyst films. 10 μ L of catalyst ink

was pipetted onto carbon sheet (~10 mm x 50 mm) and dried at 60 °C for 7 minutes. The pipetting and drying step was repeated 10 times. The final films contain about 0.1 mg of catalyst powder. Electrochemical treatments (dealloying, oxidation) were then carried out as in normal RDE measurements, with an exception that the GC electrode was not used as the working electrode but the carbon sheet.

Raw HE XRD data were corrected for air (measured separately), instrumental (measured separately) and C or ATO support (measured separately) scattering, converted into absolute (electron) units and then Fourier transformed into atomic PDFs. Note that as obtained atomic PDFs largely reflect atomic correlations/atomic-scale structure in Ir-Ni nanoparticles since the contribution from C or ATO support has been eliminated during raw data processing.

Experimental atomic PDFs were approached with simple models based on/constrained to fcc-type structure/lattice occurring both with bulk Ni and Ir. Within this simplistic model approximation, atoms have to occupy identical sites/vertices of an fcc-type lattice and so are assigned appropriately averaged, $(3\text{Ni} + 1\text{Ir})/4$, scattering power for X-rays. Reported fcc-lattice parameters were obtained by the fitting model computed against experimental PDFs. Note that so obtained fcc-lattice parameters reflect the whole set of characteristic interatomic distances in the respective nanoparticles. Yet, without any model assumptions, individual interatomic distances such as radii of first atomic coordination spheres/average first atomic pair distances can be extracted directly from the experimental PDFs.

2.3. Electrochemical characterization

Electrochemical experiments were performed in a three-compartment glass cell with a rotating disk electrode (RDE, 5 mm in diameter of glassy carbon, Pine Instrument) and a potentiostat (Biologic) at room temperature. A Pt-mesh and a Hg/Hg₂SO₄ electrode (in saturated K₂SO₄) were used as counter electrode and reference electrode, respectively. Electrochemical setup is presented in **Figure 7**.

All electrochemical measurements were carried out in N₂-saturated 0.05M H₂SO₄. All potentials reported were normalized with respect to the reversible hydrogen electrode (RHE) in 0.05M H₂SO₄.

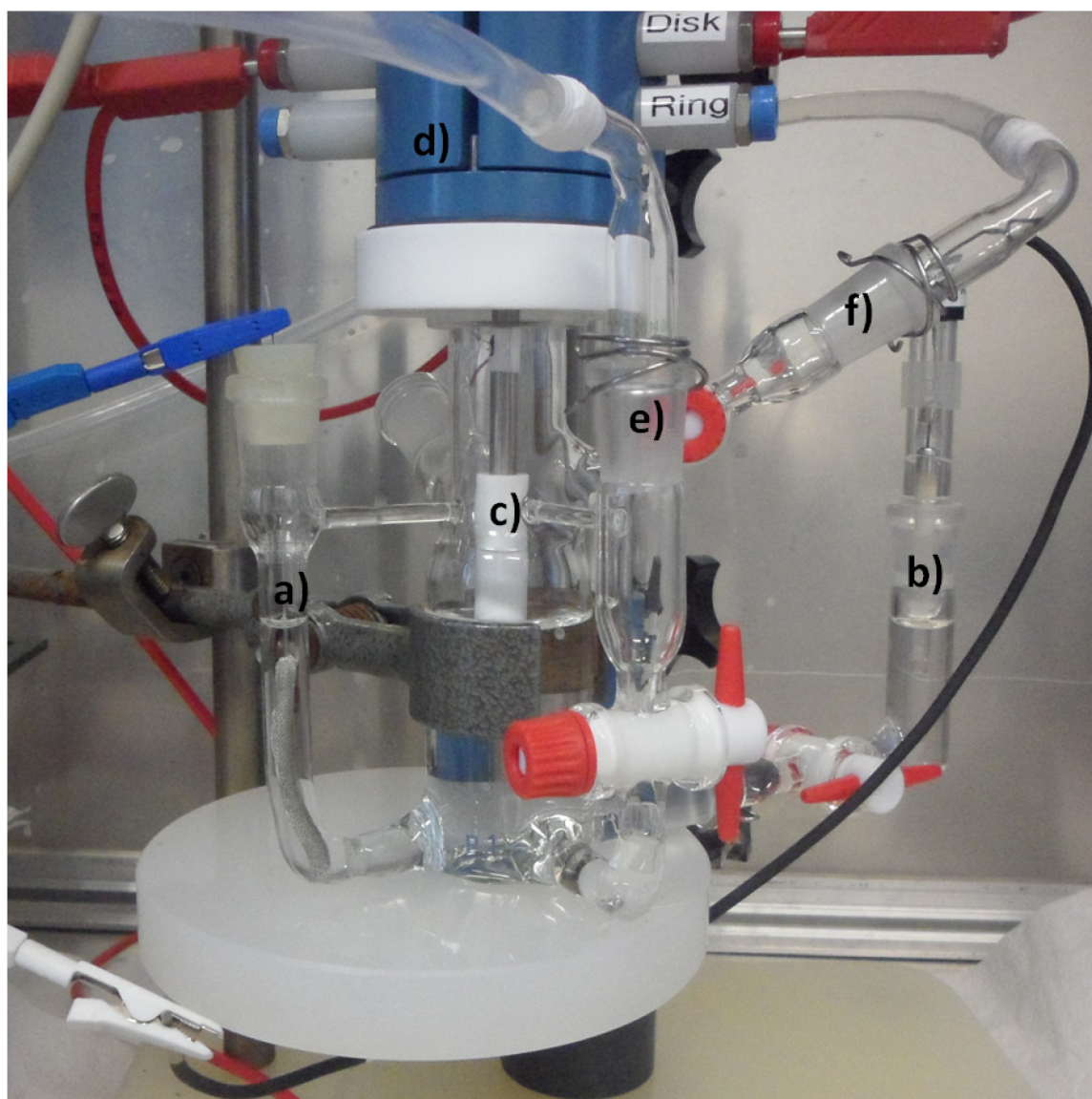


Figure 7. Electrochemical setup. a) counter electrode (Pt mesh), b) reference electrode (Hg/HgSO₄ in saturated K₂SO₄), c) working electrode RDE (thin film of catalyst on glassy carbon), d) rotator, e) and f) gas inlets.

2.3.1. Preparation of catalytic ink

To prepare the catalytic ink, a certain amount of catalyst was suspended in 3.980 mL of ultrapure water (Millipore, 18 M Ω), 1.000 mL of isopropanol and 20 μ L of Nafion[®] solution (5 wt % in lower aliphatic alcohols and H₂O, Sigma-Aldrich). The amount of catalyst was calculated in order to get the Ir concentration of 0.2 mg_{Ir} mL⁻¹_{Ink}. The mixture was ultra sonified for 15 min (with carbon supported catalysts) or for 30 min (with ATO supported catalysts) using a Branson sonifier to form a uniform ink.

2.3.2. Preparation of working electrode

The glassy carbon (GC) rotating disk electrodes (Pine Instrument, 5 mm in diameter of glassy carbon) were polished manually in two steps: first with Buehler "Alpha micropolish 1" solution on a Nylon sheet and second, after rinsing with ultrapure water, with Buehler "Alpha micropolish 0.05" solution on a Microloth® sheet. Electrodes were then sonicated in water, acetone and again in water, each step for 5 minutes, to remove the polishing solution residues. 10 μL of the catalytic ink prepared in 2.3.1 was then pipetted onto the polished and cleaned GC electrode and dried at 60 °C for 7 min in air, resulting in a uniform catalyst thin film.

2.3.3. Electrochemical protocols

Electrochemical dealloying. In order to remove less noble metal (Ni) from surface of the alloy nanoparticles (dealloying), the potential applied on the working electrode was cycled between +0.05 V and +0.8 V for 200 cycles at a scan rate of 500 mV s^{-1} in 0.05M H_2SO_4 aqueous solution. During potential cycling, Ni was gradually dissolved and the surface was enriched by Ir.

Electrochemical oxidation. The working electrode potential was cycled between +0.05 V and +1.5 V for 50 cycles at a scan rate of 500 mV s^{-1} in 0.05M H_2SO_4 aqueous solution to form oxidized IrNi@IrO_x (IrNiO_x) metal-oxide hybrid core-shell nanoparticles.

High potential direct oxidation. The working electrode potential was cycled between +1.0 V and +1.8 V at a scan rate of 5 mV s^{-1} for 1 cycle and subsequently cycled between +0.05 V and +1.5 V at a scan rate of 500 mV s^{-1} for 10 cycles, if not stated otherwise, in 0.05M H_2SO_4 aqueous solution.

Electrochemically active surface area (ECSA) evaluation. To estimate the ECSA of the Ir-Ni NP catalysts, the working electrode potential was scanned between +0.05 V and +0.80 V at a scan rate of 20 mV s^{-1} for 3 cycles. ECSA was evaluated based on the hydrogen underpotential deposition (H_{upd}) peak in anodic scans, utilizing the previously reported conversion factor of 218 $\mu\text{C cm}^{-2}$ between adsorbed hydrogen charge and real Ir based surface area.⁹²

Electrochemically accessible Ir redox sites (number of active sites) evaluation. To estimate the number of accessible Ir active sites, the working electrode potential was scanned between +0.4 V and +1.4 V at a scan rate of 20 mV s^{-1} for 3 cycles. Number

of active sites was estimated based on the anodic charge of Ir(III)-Ir(IV) peak with capacitance current subtraction.

Electrochemical active surface area (ECSA) of ATO supported samples is evaluated based on the integrated charge from anodic sweep of the CVs from 0.4 V to 1.4 V at scan rate of 20 mV s⁻¹.

Electrochemical catalytic activity test for oxygen evolution reaction (OER test protocol). After pre-treatment, the electrochemical catalytic activity of the oxidized nanoparticles was tested. Polarization curves were scanned forward from 1.0V to 1.8V and backward from 1.8V to 1.0V with scan rate of 5 mV s⁻¹ and rotation of 1600 rpm. Potential Electrochemical Impedance Spectroscopy (PEIS) was carried out before each OER measurement for ohmic loss (iR) correction. The electrochemical measurements were repeated on three catalyst films for each catalyst. The electrochemical OER polarization curves were corrected for the uncompensated ohmic resistance of the set-up and electrolyte (iR correction). The geometric current densities were calculated by normalizing the iR-corrected currents to the surface area of the GC electrode (~0.196 cm²). The Ir-mass based OER curves were calculated by normalizing the iR-corrected currents to the actual Ir mass on the electrode. The Ir-mass based OER activities at specific overpotentials (250 mV, 280 mV and 300 mV) was evaluated by taking the average current density values of the iR-corrected and capacitance-corrected anodic and cathodic scans, where the capacitive currents were evaluated by the mean value of the current in the potential range of 1.0 to 1.23 V, where no faradaic process takes place

.Chronopotentiometric measurements. The stability of the electrocatalysts was tested by the chronopotentiometry technique, in which the current density was held at 1 mA cm⁻² for a period of 3 hours for carbon supported samples (see chapter 4) and a period of 20 hours for ATO supported sample and benchmarks (see chapter 5) while the potential was recorded.

Duty cycle measurements. In order to test the stability of the catalysts under conditions similar to working conditions of PEM electrolyzers, we used a duty cycle protocol (**Figure 8**).

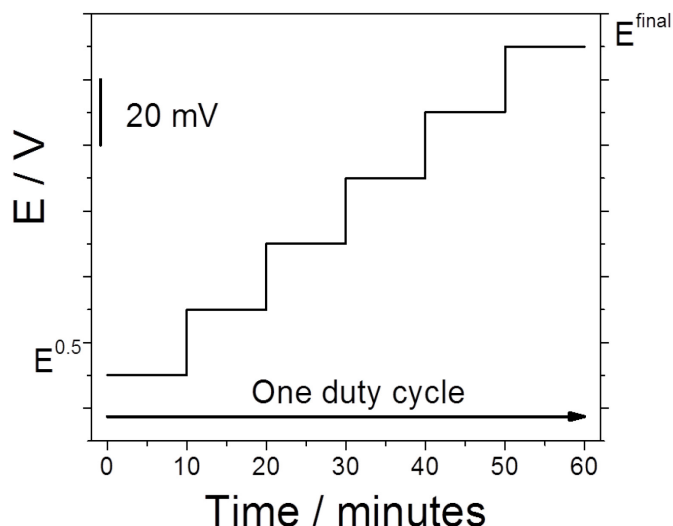


Figure 8. One duty cycle of the durability test under stepwise load increase.

In detail, the potential was first kept at $E^{0.5}$ (where the current density reached 0.5 mA cm^{-2}) for a period of 10 minutes, then increased by 20 mV and kept at the new value for 10 minutes. This increasing step was repeated until the last holding potential E^{final} equaled $E^{0.5} + 100 \text{ mV}$. This allows the catalysts undergo similar conditions as in the operating conditions of an electrolyzer. The process from potential of $E^{0.5}$ to E^{final} was then called one duty cycle. The duty cycle was repeated for 5 times, after each duty cycle, the OER activity was tested by OER test protocol.

Detailed settings of dealloying and stepwise oxidized protocol.

- 1) Chrono-amperometry CA ($E = 0.05 \text{ V vs. RHE}$, $t = 2 \text{ min}$): This technique is used at the beginning of each measurement protocol in order to avoid the strong potential variations when immersing the working electrode in the electrolyte. The potential is set at the desired starting potential of the next technique and maintained for a certain period of time to assure that the working electrode can be immersed without air bubbles. When this is done, the next technique will be started manually.
- 2) Cyclic voltammetry CV ($E_1 = 0.05 \text{ V vs. RHE}$, $E_2 = 0.8 \text{ V vs. RHE}$, $v_s = 20 \text{ mV s}^{-1}$, $n_c = 2$): electrochemical surface area (ECSA) before dealloying. The potential is increased from the starting potential E_1 until the potential E_2 is reached with the scan rate v_s and then decreased with the same scan rate until the potential E_1 is reached. This provides a continuous triangular voltage. While these potential changes continuously, the current is recorded.

A scan from E_1 to E_2 and back is counted as one cycle, is measured by the n_c repetitions. The potential range between 0.05 V and 0.8 V vs. RHE was chosen in order to purify and characterize the electrode surface. The hydrogen underpotential deposition (H_{upd}) peak (at about 0.1 V vs. RHE) which is known from platinum-CV also showed on metallic iridium. To enable the determination of the surface, the potential should not exceed 0.8 V vs. RHE in order to avoid irreversible oxidation of the nanoparticles, since iridium oxide shows no H_{upd} peak. The low scan rate was chosen to determine and integrate the H_{upd} peak more exactly.

- 3) Chrono-amperometry CA ($E = 0.05$ V vs. RHE, $t = 2$ min).
- 4) Cyclic voltammetry CV ($E_1 = 0.05$ V vs. RHE, $E_2 = 0.8$ V vs. RHE, $v_s = 500$ mV s^{-1} , $n_c = 199$): Dealloying process. The potential is scanned with high scan rate to remove Ni from surface of the nanoparticles.
- 5) Chrono-amperometry CA ($E = 0.05$ V vs. RHE, $t = 2$ min).
- 6) Cyclic voltammetry CV ($E_1 = 0.05$ V vs. RHE, $E_2 = 0.8$ V vs. RHE, $v_s = 20$ mV s^{-1} , $n_c = 2$): ECSA after dealloying.
- 7) Chrono-amperometry CA ($E = 0.05$ V vs. RHE, $t = 2$ min).
- 8) Cyclic voltammetry ($E_1 = 0.05$ V vs. RHE, $E_2 = 1.5$ V vs. RHE, $v_s = 500$ mV s^{-1} , $n_c = 49$): stepwise oxidation. In this cyclic voltammetry, the upper potential is increased to 1.5 V vs. RHE in order to oxidize the iridium surface. Since the nanoparticles were already dealloyed before applied this oxidation step, we call this stepwise oxidation. n_c is number of repetitions, normally $n_c = 49$ for 50 cycles of oxidation, unless otherwise stated.
- 9) Cyclic voltammetry ($E_1 = 0.4$ V vs. RHE, $E_2 = 1.4$ V vs. RHE, $v_s = 20$ mV s^{-1} , $n_c = 2$): $\text{Ir}^{3+}/\text{Ir}^{4+}$ redox peak analysis. Since with the oxidation of the nanoparticles, the H_{upd} for the following scans is no longer available, the surface active sites will be analyzed as the oxidation peak of $\text{Ir}^{3+}/\text{Ir}^{4+}$ at ~ 0.9 V. Here a lower scanning speed is again selected to determine the redox peak better.

Settings of directly oxidized protocol.

- 1) Chrono-amperometry CA ($E = 0.05$ V vs. RHE, $t = 2$ min).

- 2) Cyclic voltammetry ($E_1 = 0.05$ V vs. RHE, $E_2 = 1.5$ V vs. RHE, $v_s = 500$ mV s⁻¹, $n_c = 49$): direct oxidation. Normally $n_c = 49$ for 50 cycles of oxidation, unless otherwise stated.
- 3) Chrono-amperometry CA ($E = 0.05$ V vs. RHE, $t = 2$ min).
- 4) Cyclic voltammetry ($E_1 = 0.4$ V vs. RHE, $E_2 = 1.4$ V vs. RHE, $v_s = 20$ mV s⁻¹, $n_c = 2$): Ir³⁺/Ir⁴⁺ redox peak analysis.

Settings of high potential directly oxidized protocol for ATO supported samples

- 1) Chrono-amperometry CA ($E = 1.00$ V vs. RHE, $t = 2$ min).
- 2) Modular cyclic voltammetry ($E_1 = 1.00$ V vs. RHE, $E_2 = 1.80$ V vs. RHE, $v_s = 5$ mV s⁻¹).
- 3) Chrono-amperometry CA ($E = 0.05$ V vs. RHE, $t = 1$ min).
- 4) Cyclic voltammetry ($E_1 = 0.05$ V vs. RHE, $E_2 = 1.5$ V vs. RHE, $v_s = 500$ mV s⁻¹, $n_c = 49$): direct oxidation. Normally $n_c = 49$ for 50 cycles of oxidation, unless otherwise stated.
- 5) Chrono-amperometry CA ($E = 0.05$ V vs. RHE, $t = 2$ min).
- 6) Cyclic voltammetry ($E_1 = 0.4$ V vs. RHE, $E_2 = 1.4$ V vs. RHE, $v_s = 20$ mV s⁻¹, $n_c = 2$): Ir³⁺/Ir⁴⁺ redox peak analysis.

Settings of OER tests.

- 7) Chrono-amperometry CA ($E = 1.00$ V vs. RHE, $t = 2$ min).
- 8) Potentiostatic impedance spectroscopy ($E = 1.00$ V vs. RHE, $t = 2$ min, 10 Hz $\leq f \leq 100$ kHz, $V_a = 10$ mV): In this method, after the potential E for the set time t was maintained, the sinusoidal potential vibration was created in a specified frequency range and the corresponding current was recorded. From the obtained Nyquist plot the solution resistance can be determined. This is read at the point $\text{Im}(Z) = 0$.
- 9) Chrono-amperometry CA ($E = 1.00$ V vs. RHE, $t = 2$ min).
- 10) Modular cyclic voltammetry ($E_1 = 1.00$ V vs. RHE, $E_2 = 2.00$ V vs. RHE, $v_s = 5$ mV s⁻¹, $I_{\text{max}} = 9.8$ mA): This technique can be used as a standard CV, but offers the possibility to introduce certain termination criteria. If I_{max} is reached before the potential reach 2.00 V, then the potential will be stopped and scanned back to 1.00 V vs. RHE with $v_s = 5$ mV s⁻¹.

Settings of chronopotentiometry tests.

- 1) Chrono-amperometry CA ($E = 1.00$ V vs. RHE, $t = 2$ min).
- 2) Potentiostatic impedance spectroscopy ($E = 1.00$ V vs. RHE, $t = 2$ min, 10 Hz $\leq f \leq 100$ kHz, $V_a = 10$ mV).
- 3) Chronopotentiometry ($I = 196$ μ A, $t = 3$ hours or 20 hours, $E_{\max} = 2.00$ V vs. RHE). If the potential reaches 2.00V vs RHE before setting time, measurement will be stopped to protect the GC electrode from corrosion.

Settings of duty cycle tests.

- 1) Chronoamperometry CA ($E = 1.00$ V vs. RHE, $t = 2$ min).
- 2) Modular cyclic voltammetry ($E_1 = 1.00$ V vs. RHE, $E_2 = 2.00$ V vs. RHE, $v_s = 5$ mV s⁻¹, $I_{\max} = 9.8$ mA).
- 3) Modular cyclic voltammetry ($E_1 = 1.00$ V vs. RHE, $E_2 = 2.00$ V vs. RHE, $v_s = 5$ mV s⁻¹, $I_{\max} = 0.098$ mA). When the current reaches 0.098 mA (at a potential $E^{0.5}$), this technique will be stopped and the next technique will be started.
- 4) Chronoamperometry ($E = 0.00$ V vs. E_{ctrl} , $t = 10$ min): The potential achieved in the previous technique is held and the corresponding current is recorded.
- 5) Potentiostatic impedance spectroscopy ($E = 0.00$ V vs. E_{ctrl} , $t = 20$ s, 10 Hz $\leq f \leq 100$ kHz, $V_a = 10$ mV).
- 6) Chronoamperometry ($E = 0.02$ V vs. E_{ctrl} , $t = 10$ min). The potential is increased by 0.02 V.
- 7) Potentiostatic impedance spectroscopy ($E = 0.00$ V vs. E_{ctrl} , $t = 20$ s, 10 Hz $\leq f \leq 100$ kHz, $V_a = 10$ mV).
- 8) Loop ($N_e = 5$, $n_t = 4$). Go back to technique 5, repeat 4 times. The final potential E^{final} is equal to $E^{0.5} + 0.10$ V. From technique 3 to technique 8 is called as one duty cycle.
- 9) Chrono-amperometry CA ($E = 1.00$ V vs. RHE, $t = 2$ min).
- 10) Modular cyclic voltammetry ($E_1 = 1.00$ V vs. RHE, $E_2 = 2.00$ V vs. RHE, $v_s = 5$ mV s⁻¹, $I_{\max} = 9.8$ mA). OER test after each duty cycle.
- 11) Loop ($N_e = 3$, $n_t = 4$). Go back to technique 3, repeat for 4 times. From technique 1 to technique 11, there are 5 duty cycles tested.

3. Optimizing Synthesis Conditions of Supported Homogeneous IrNi_x Alloy Nanoparticles

3.1. Comparison of different methods for the synthesis of IrNi_x (nominal IrNi₃) alloy nanoparticles

We focused on a selected set of wet-chemical particle preparation routes as described in the following:

Method 1: Conventional impregnation method. Metal salt precursors were impregnated in support materials, followed by freeze drying and thermal annealing to remove the anions. This method requires a suitable metal salt precursor solution with suitably charged ions in order to ensure surface interaction of the metal ions with the surface. Thermal annealing will remove the precursor anion (or cation depending on the chemical nature of the precursor salt) at temperatures critically depending on the nature of the anions. Organic anions, such as formates, acetates, oxalates or citrates are preferred anions for decomposition already at or below 250 °C.

Method 2: Polyol method. Formation of bimetallic particles stabilized using surfactants (surfactant/micell routes). This method has been applied to a wide array of mono,bi and tri metallic nanoparticle system and offers a high control of dispersity. The preparation requires the selection of a high boiling point solvent, often a diol or polyol, in combination with surface-active and structure directing agent such as oleic acid, oleylamine and others.⁹³ This family of methods has come to be known as the polyol methods for the preparation of multimetallic nanoparticles. Careful choice of the reducing power is necessary to control the formation of the metallic state or higher oxidation states.

Method 3: Surfactant-free or ethylene glycol method. This is a simple solution-phase approach to fabricate noble and non-noble nanoparticles with narrow size distribution at around 160 °C, in which ethylene glycol acts not only as solvent but also as reducing agent. This method has the appeal of being very facile and offers a simplified separation and stabilization of the formed metallic nanoparticles.

The Ir : Ni ratio and the weight loading of Ir (**Table 1**) were determined by inductively coupled plasma optical emission spectrometry (ICP-OES).

Table 1. Actual Ir : Ni ratios and Ir weight loadings derived from ICP-OES of samples synthesized by different methods compared to the nominal compositions

Method	Ir : Ni molar ratio		Ir loading (wt. %)		Actual composition
	Nominal	Actual	Nominal	Actual	
Impregnation	1 : 3	1 : 3.1	20	19.5	19.5% IrNi _{3.1} /C
Polyol	1 : 3	1 : 2.8	20	16.4	16.4% IrNi _{2.8} /C
Ethylene glycol	1 : 3	1 : 0.25	20	22.0	22% IrNi _{0.25} /C

Starting from the same nominal Ir : Ni molar ratio (1 : 3) and Ir weight loading (20 wt. % iridium), the composition of the obtained samples is different from different methods. Nickel was not completely reduced in the ethylene glycol method, resulting in Ir rich nanoparticles. Using the polyol and impregnation methods both Ir and Ni precursors were reduced resulting in compositions close to the nominal composition. The Ir content in the sample synthesized by the polyol method was less than nominal value, which may be because of the rather low reaction temperature. Therefore, in the following synthesis the reaction temperature was increased in order to find out which effect the reaction temperature has on IrNi formation alloy formation in the polyol method.

The structures of as-prepared IrNi_x/C synthesized by the impregnation, polyol, and ethylene glycol method (denoted as IrNi_x-IMP, IrNi_x-PO, and IrNi_x-EG, respectively) were examined by X-ray diffraction. XRD profiles of the three IrNi_x bimetallic nanoparticle catalysts (**Figure 9a**) exhibit a diffraction pattern consistent with face-centered cubic crystal symmetry. The small bumps at around $2\theta = 25^\circ$ correspond to the carbon support. There is no superlattice peak discernible below $35^\circ 2\theta$ indicating a substitutional solid solution structure throughout. IrNi_x-PO and IrNi_x-EG exhibit single broad peaks suggesting homogeneous single-phase alloy nanoparticles with small crystallite size, IrNi_x-IMP shows sharp reflections, indicating a larger crystalline size, in addition, there are small shoulders at reflection position of Ir (111) and Ir (200) in the XRD pattern of IrNi_x-IMP (see **Figure 9b**), which can be assigned to a

second Ir-rich phase of Ir-Ni, or a pure Ir phase. All diffraction peaks of Ni-containing samples are shifted towards higher diffraction angles compared to the pure Ir reference pattern, indicating a contraction of the lattice with an increasing amount of smaller Ni atoms included in the structure.

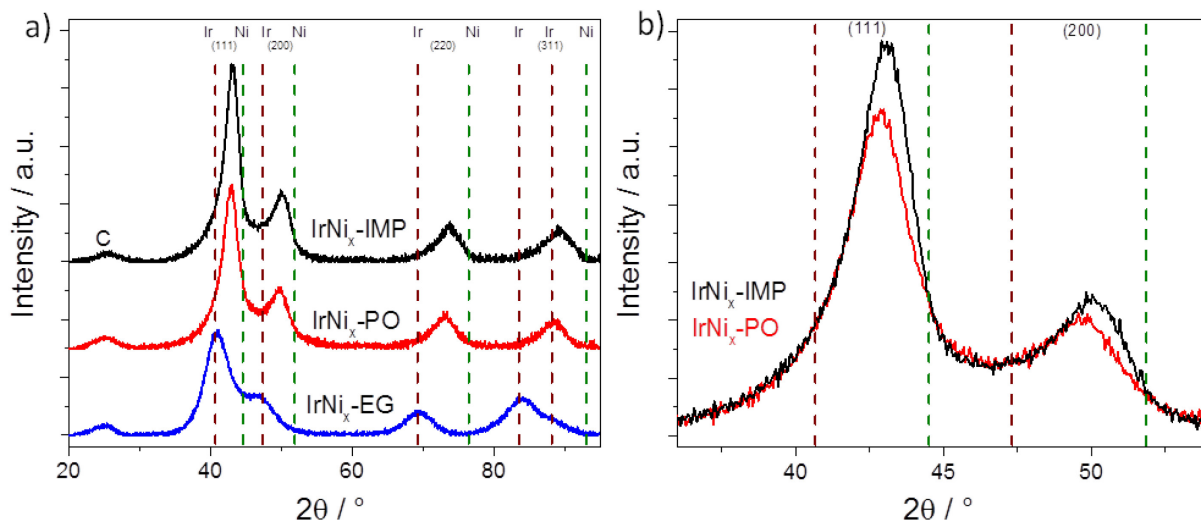


Figure 9. a) XRD patterns of IrNi_x/C synthesized by impregnation, polyol, and surfactant free methods (denoted as IrNi_x-IMP, IrNi_x-PO, and IrNi_x-EG, respectively), and b) a zoom in the first two reflections of IrNi_x-IMP and IrNi_x-PO.

From XRD and ICP-OES results, it can be concluded that using the polyol method, in which bimetallic particles were pre-formed and stabilized using surfactants and then immobilized on high surface area supports, single phase IrNi_x alloy nanoparticles with the desired composition can be obtained. Therefore, the polyol method is selected as the synthesis method for Ir-Ni nanoparticles in the following.

3.2. Impact of reaction conditions in polyol method based synthesis of IrNi alloy nanoparticles

Effect of reaction temperature.

IrNi_x/C samples were synthesized using a polyol method and DMA as co-solvent. The reaction temperature was kept at 200 °C, 220 °C, or 240 °C, the obtained samples were denoted as IrNi_x/C-200, IrNi_x/C-220, and IrNi_x/C-240, respectively. Atomic compositions of the obtained samples are tabulated in **Table 2**.

Table 2. Actual Ir : Ni ratios and Ir weight loadings derived from ICP-OES measurements of IrNi_x/C-200, IrNi_x/C-220, and IrNi_x/C-240 compared to the nominal compositions

Sample	Ir : Ni molar ratio		Ir loading (wt. %)		Actual composition
	Nominal	Actual	Nominal	Actual	
IrNi _x /C-200	1 : 3	2.3	20	12.8	12.8% IrNi _{2.3} /C
IrNi _x /C-220	1 : 3	2.3	20	14.5	14.5% IrNi _{2.3} /C
IrNi _x /C-240	1 : 3	3.2	20	14.9	14.9% IrNi _{3.2} /C

Since the composition of the obtained IrNi nanoparticles was closest to expected nominal composition at a reaction temperature of 240 °C, this temperature was selected for further investigations.

Effect of co-solvents for Ir precursor.

In the polyol method, the Ir precursor needed to be introduced into the reaction mixture by hot injection at the reaction temperature, therefore, this method required a suitable co-solvent beside the reaction solvent which needs not only to dissolve the Ir precursor but also to be miscible with the main reaction solvent (benzyl ether in this case). This is to ensure the interaction of the Ir ions with Ni ions and the reducing agent.

In the polyol method which has been well established for the PtNi_x nanoparticle synthesis,^{94, 95} the co-solvent 1,2 dichlorobenzene C₆H₄Cl₂ (DCB) was used to dissolve the Pt precursor. However, the low solubility of Ir(CH₃COO)₃ in 1,2-C₆H₄Cl₂ made large amounts of co-solvent necessary, resulting in an inhomogeneous mixture of the co-solvent and the reaction solvent (benzyl ether) during the reaction, which was detrimental for the synthesis. The solubility of the Ir(CH₃COO)₃ precursor in various solvents was tested and ethanol, water, dimethylacetamide (DMA), N-methyl-2-pyrrolidone (NMP) appeared as good solvents for Ir(CH₃COO)₃. However, ethanol and water are insoluble in benzyl ether, and can hence not used in the present polyol

synthesis. Therefore, only DMA and NMP were tested as co-solvents for Ir(CH₃COO)₃.

Atomic compositions of IrNi_x/C synthesized using DCB, NMP, and DMA as co-solvent (denoted as IrNi_x-DCB, IrNi_x-NMP, and IrNi_x-DMA, respectively) were tabulated in **Table 3**.

Table 3. Actual Ir : Ni ratios and Ir weight loadings derived from ICP-OES of IrNi_x-DCB, IrNi_x-NMP, and IrNi_x-DMA compared to nominal compositions.

Sample	Ir : Ni molar ratio		Ir loading (wt. %)		Actual composition
	Nominal	Actual	Nominal	Actual	
IrNi _x -DCB	1 : 3	1 : 2.1	20	13.7	13.7% IrNi _{2.1} /C
IrNi _x -NMP	1 : 3	1 : 4.8	20	9.9	9.9% IrNi _{4.8} /C
IrNi _x -DMA	1 : 3	1 : 3.2	20	14.9	14.9% IrNi _{3.2} /C

Starting from the same nominal Ir : Ni molar ratio (1 : 3) and Ir weight loading (20 wt. % iridium), the actual compositions of as-received samples differ depending on the co-solvent applied. DCB resulted in Ir rich nanoparticles with an Ir content higher than the nominal value, most likely due to an inhomogeneous mixture of co-solvent and reaction solvent, leading to an insufficient interaction of Ni ions dissolved in the reaction solvent with Ir ions dissolved in the co-solvent and, hence, a less efficient reduction of Ni ions. In contrast, NMP resulted in Ni rich nanoparticles with a Ni content higher than the nominal Ni value. Interestingly, in this case only half of the Ir precursor ions were reduced and transferred to the final alloy particles. DMA appeared as a good co-solvent for the polyol method as almost all Ir precursor ions and Ni precursor ions were reduced and transferred to the final product. The actual composition was as almost similar to the nominal composition.

The structure of IrNi_x nanoparticles synthesized by the polyol method using different co-solvents was examined by XRD. XRD profiles of IrNi_x-DCB, IrNi_x-NMP, and IrNi_x-DMA (**Figure 10**) exhibit a diffraction pattern consistent with face-centered cubic crystal symmetry. The small bumps at around $2\theta = 25^\circ$ are related to the carbon

support. There is no superlattice peak discernible below 35° 2θ indicating a substitutional solid solution structure throughout. XRD patterns of IrNi_x-DCB and IrNi_x-NMP showed sharp reflections indicating large crystallite sizes. In addition, there are small shoulders near the Ir (111) and Ir (200) reflections in the XRD patterns of IrNi_x-DCB and IrNi_x-NMP, which can be assigned to a second phase of Ir-Ni. The XRD pattern of IrNi_x-DMA exhibits single broad peaks indicating the formation of homogeneous single-phase alloy nanoparticles with small crystallite sizes. All diffraction peaks of Ni-containing samples shifted towards higher 2θ values compared to the pure Ir reference pattern, indicating the contraction of the lattice by alloying Ir with smaller Ni atoms.

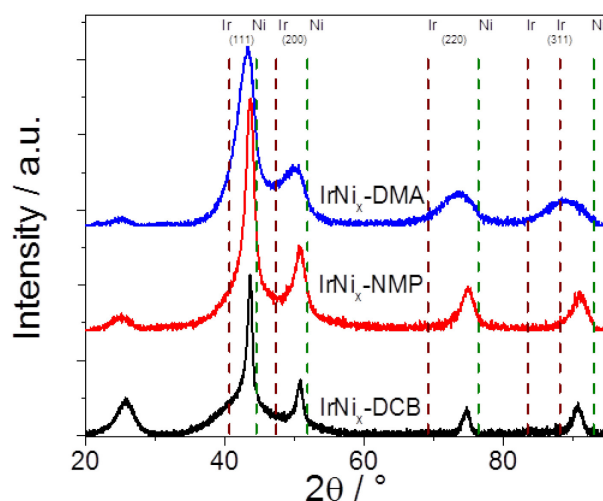


Figure 10. XRD patterns of IrNi_x/C synthesized by the polyol method at 240 °C using different co-solvents: 1,2-dichlorobenzene (DCB), N-methyl-2-pyrrolidone (NMP), dimethylacetamide (DMA), (denoted as IrNi_x-DCB, IrNi_x-NMP, IrNi_x-DMA, respectively).

From ICP-OES and XRD results, we concluded that DMA is the most suitable co-solvent for IrNi_x alloy nanoparticle synthesis using the polyol method. The obtained alloy nanoparticles constitute a homogeneous single phase alloy with small crystallite size and expected composition. Therefore, DMA was chosen as co-solvent for IrNi_x nanoparticle synthesis in the following.

In order to confirm the success of the nanoparticle synthesis, we performed TEM of the unsupported and carbon supported IrNi_x nanoparticles synthesized by the polyol method with optimized conditions. The TEM images and particle size histograms are presented in **Figure 11** and **Figure 12**, respectively.

The unsupported and supported nanoparticles are in the size range of below 10 nm with narrow size distribution. The size of unsupported IrNi_x nanoparticles (7.6 ± 1.6 nm) is smaller than that of carbon supported nanoparticles (8.1 ± 1.6 nm), probably because during thermal treatment small nanoparticles were sintered to form larger nanoparticles.

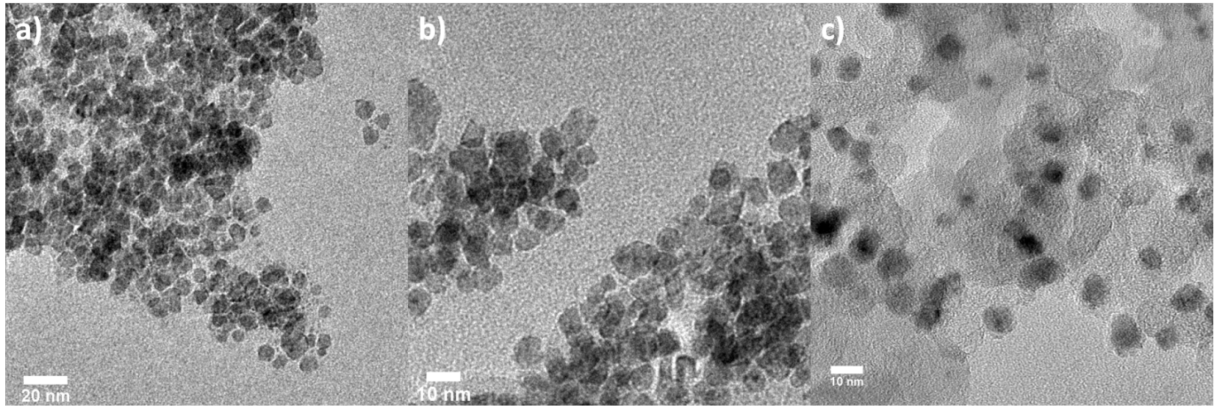


Figure 11. TEM images of unsupported IrNi_x nanoparticles with different magnifications (a and b), and carbon supported IrNi_x nanoparticles (c) synthesized by the polyol method with optimized conditions.

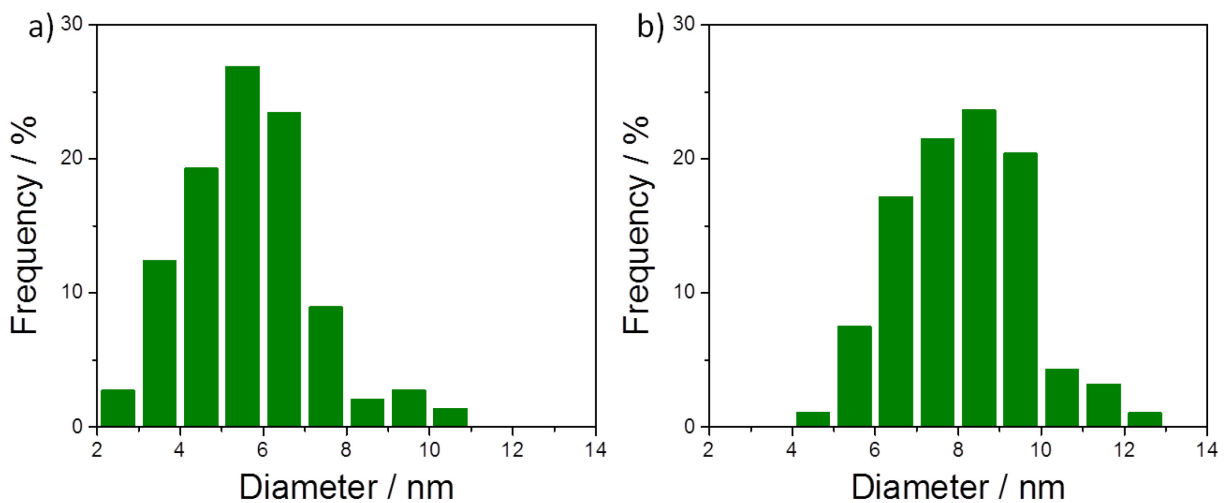


Figure 12. Particle size histograms of a) unsupported IrNi_x nanoparticles, and b) carbon supported IrNi_x nanoparticles synthesized by the polyol method with optimized conditions.

3.3. Summary

In summary, the polyol method using oleic acid and oleylamine as capping agents, DMA as co-solvent for the Ir precursor and a reaction temperature of 240 °C appeared as the most suitable method for the synthesis of IrNi_x nanoparticle alloys, resulting in homogeneous, small alloyed nanoparticles, and was hence used as synthetic route for the following studies.

For ATO supported samples (will be discussed later in chapter 5, 6, and 7), the ATO support material were introduced into the reaction mixture from beginning in order to ensure a good contact of the IrNi_x nanoparticles and the oxide support.

4. Synthesis and Characterization of IrNiO_x Core-Shell Nanoparticles as Oxygen Evolution Electrocatalysts

[Ref. 96] - Reproduced with permission of The Royal Society of Chemistry, copyright (2014).

A family of dealloyed metal-oxide hybrid (M₁M₂@M₁O_x) core@shell nanoparticle catalysts is demonstrated to provide substantial advances in terms of more efficient and less expensive electrolytic water splitting. IrNi@IrO_x nanoparticles were synthesized from IrNi precursor alloys through selective surface Ni dealloying and controlled surface oxidation of Ir. Detailed depth-resolved insight into chemical structure, composition, morphology, oxidation state was obtained using spectroscopic, diffraction, and scanning microscopic techniques (XANES, XRD, STEM-EDX, XPS), which confirmed our structural hypotheses. A 3-fold catalytic activity enhancement for the electrochemical oxygen evolution reaction (OER) over Ir and RuO₂ benchmark catalysts was observed for the core-shell catalysts on a noble metal mass as well as active site basis.

This study documents the successful use of synthetic dealloying for the preparation of metal-oxide hybrid core-shell catalysts. The concept is quite general, can be applied to other noble metal nanoparticles, and points out a path forward to nanostructured proton-exchange-electrolyzer electrodes with dramatically reduced noble metal content. The essential idea involves Ir-Ni precursor alloy nanoparticles that were selectively electrochemically dealloyed to form metallic core-shell nanoparticles. Subsequently or simultaneously, they are selectively dealloyed and surface oxidized to form active metal-oxide hybrid core-shell nanoparticle IrNi@IrO_x catalysts with outstanding catalytic OER activities. Special emphasis is placed on the role of Ni in the alloy material. First, it enhances the electrochemical active surface area of the catalysts during selective dealloying. Second, subsurface Ni caused electronic and strain effects resulting in higher intrinsic OER activity, and third, the high Ni core content significantly lowers the total Ir loading.

4.1. Experimental

Synthesis of alloy nanoparticles and benchmark

IrNi_x bimetallic nanoparticles with different Ni/Ir molar ratios (Ni/Ir molar ratios of 2, 3, and 5) were prepared using a modified and optimized polyol method as discussed in chapter 3. The nanoparticles were immobilized on high surface area carbon black Vulcan® XC72 from Carbot. For comparison, carbon supported pure Ir nanoparticles were synthesized using ethylene glycol as reducing agent and solvent (see chapter 2).

Electrochemical measurements

All electrochemical measurements were carried out in N₂-saturated 0.05M H₂SO₄ and repeated on three catalyst films for each catalyst.

Preparation of IrNi@IrO_x hybrid core-shell catalysts

Preparation procedures of IrNi@IrO_x hybrid core-shell nanoparticles are illustrated in **Figure 13**. The IrNi_x nanoparticle precursor alloys (referred to as PA-IrNi_x) were first electrochemically dealloyed to form dealloyed metallic core-shell nanoparticles (“D-IrNi_x”). Subsequently, they were selectively surface oxidized to form “SO-IrNi@IrO_x” metal-oxide hybrid core-shell nanoparticles. SO refers to the stepwise nature of the preparation (“SO-IrNi_x”). The stepwise oxidation synthesis is depicted schematically in **Figure 13** (top). Alternatively, DO-IrNi@IrO_x samples were prepared by direct dealloying/oxidation, that is, coupled dealloying/oxidation (“DO-IrNi_x”) as depicted in **Figure 13** (bottom).

Note that in the following the SO-IrNi_x or DO-IrNi_x nomenclatures emphasize the stoichiometry of the parent precursor alloy, while the SO-IrNi@IrO_x and DO-IrNi@IrO_x nomenclature stress the chemical core-shell structure. The detailed electrochemical protocols for synthesizing IrNi_x core-shell nanoparticles by electrochemical dealloying and oxidation are given in section 2.3.3.

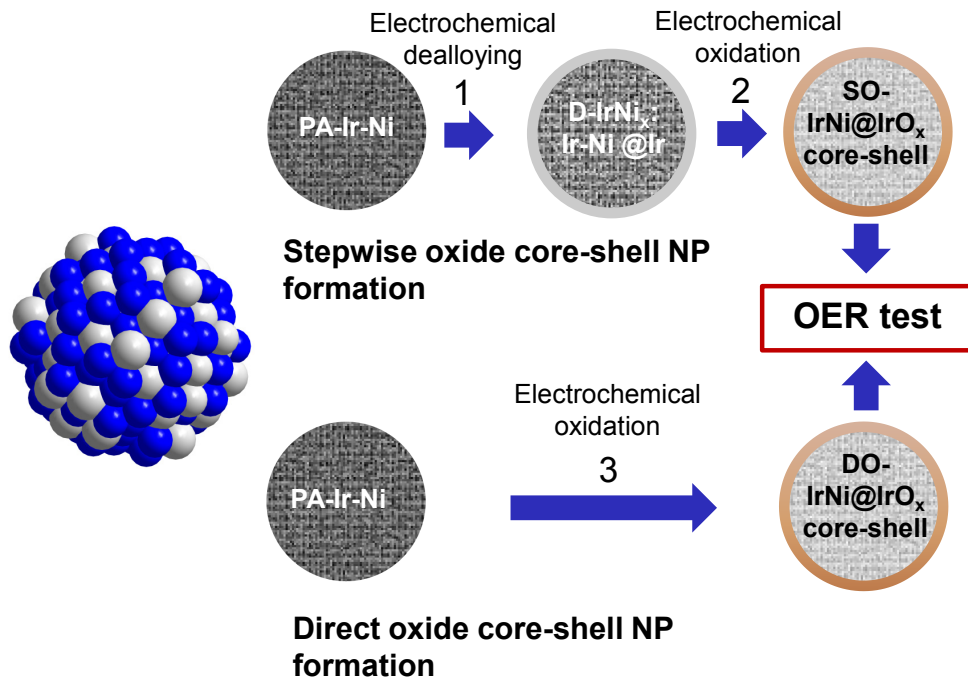


Figure 13. Synthetic protocol for the preparation of SO-IrNi@IrO_x and DO-IrNi@IrO_x hybrid core-shell nanoparticle catalysts. Precursor IrNi alloys (“PA-IrNi”, and alloy scheme on left, blue: Ni, grey: Ir) are stepwise (SO) or directly (DO) dealloyed and surface oxidized. The “SO-IrNi_x” or “DO-IrNi_x” nomenclatures emphasize the original stoichiometry of the parent precursor alloy, while the “SO-IrNi@IrO_x” and “DO-IrNi@IrO_x” nomenclature stresses the chemical structure of the core-shell particles. Reprinted from Ref. 96 with permission of The Royal Society of Chemistry, copyright (2014).

Stability test of IrNi@IrO_x core-shell catalysts

The catalytic stability was tested for the pure Ir nanoparticles and directly oxidized IrNi_{3.3} core-shell nanoparticles by a chronopotentiometry measurement, in which the current density was held at 1 mA cm⁻² for a period of 3 hours and the potential was measured correspondingly. The stability tested IrNi_{3.3} sample was then denoted as DO-IrNi_{3.3}-Stabil.

More details about electrochemical protocols can be found in section 2.3.3.

4.2. IrNi_x precursor alloys (PA-IrNi_x)

Carbon (Vulcan® XC72, Cabot) supported Ir-Ni bimetallic precursor alloy nanoparticles (denoted as “PA-IrNi_x” in **Figure 13**) were synthesized with 3 different IrNi_x ratios ($x = 2.3, 3.3, 5.7$, obtained from nominal Ni/Ir ratios of 2, 3, and 5, respectively). Carbon supported pure Ir nanoparticles were used as benchmark

catalysts. Morphology and structure of the PA-IrNi_x nanoparticles were characterized by ICP-OES, powder X-ray diffraction and TEM.

The XRD profiles of the IrNi_x and pure Ir nanoparticle catalysts (**Figure 14a**) exhibit a diffraction pattern consistent with a face-centered cubic (fcc) crystal symmetry. There is no superlattice peak discernible below 35 ° indicating a substitutional solid solution structure throughout. Pure Ir, IrNi_{2.3} and IrNi_{3.3} materials exhibit single broad peaks suggesting homogeneous single-phase metallic (alloy) nanoparticles with small crystallite size, on the other hand, IrNi_{5.7} shows sharper diffraction peaks, indicating larger crystalline size. All diffraction peaks of Ni-containing samples are shifted toward higher 2θ compared to Ir nanoparticles, indicating a contraction of the lattice with the increasing amount of smaller Ni atoms. The relationship between the lattice constant derived from the (111) planes and the composition of the annealed IrNi_x nanoparticles (**Figure 14b**) follows the Vegard's lattice constant - composition law surprisingly well, indicating good atomic mixing of Ir and Ni atoms in alloyed nanoparticles.

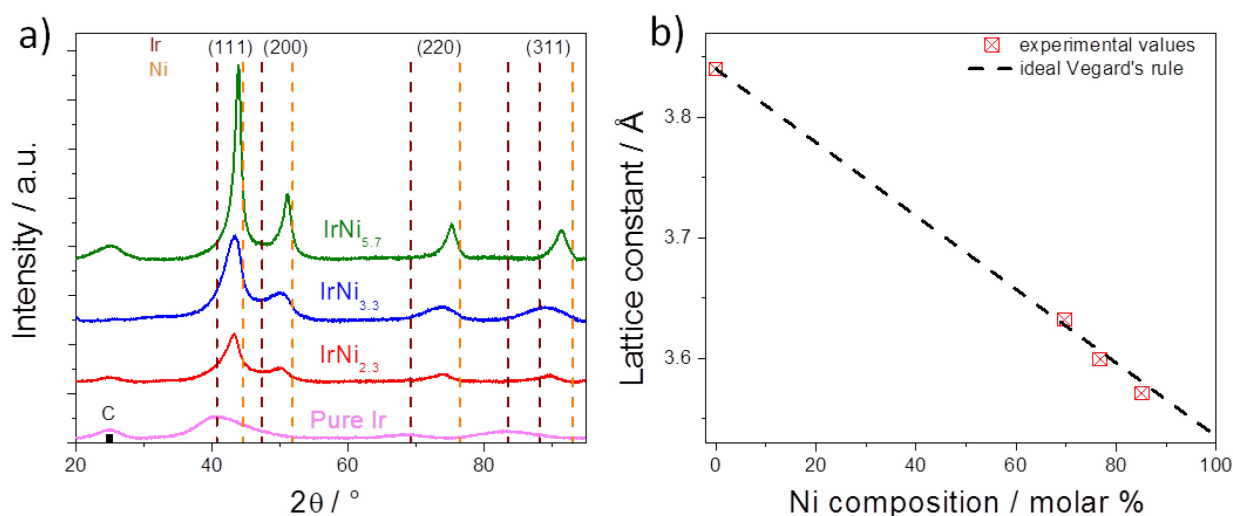


Figure 14. a) Powder X-ray diffraction patterns of Ir, IrNi_{2.3}, IrNi_{3.3}, IrNi_{5.7} precursor alloy catalysts; C denotes a support reflection; vertical dashed lines indicate database reflections of pure Ir and pure Ni, and b) relationship between lattice constant and Ni composition (red symbols) compared to Vegard's rule (dashed line). Reprinted from Ref. 96 with permission of The Royal Society of Chemistry, copyright (2014).

Bright field TEM images and particle size histograms (**Figure 15**) showed a narrow particle size distribution of the pure Ir and IrNi_x bimetallic nanoparticles up to the IrNi_{3.3} ratio. The mean particle size increased with increasing bulk Ni content, as well as the deviation of particle size.

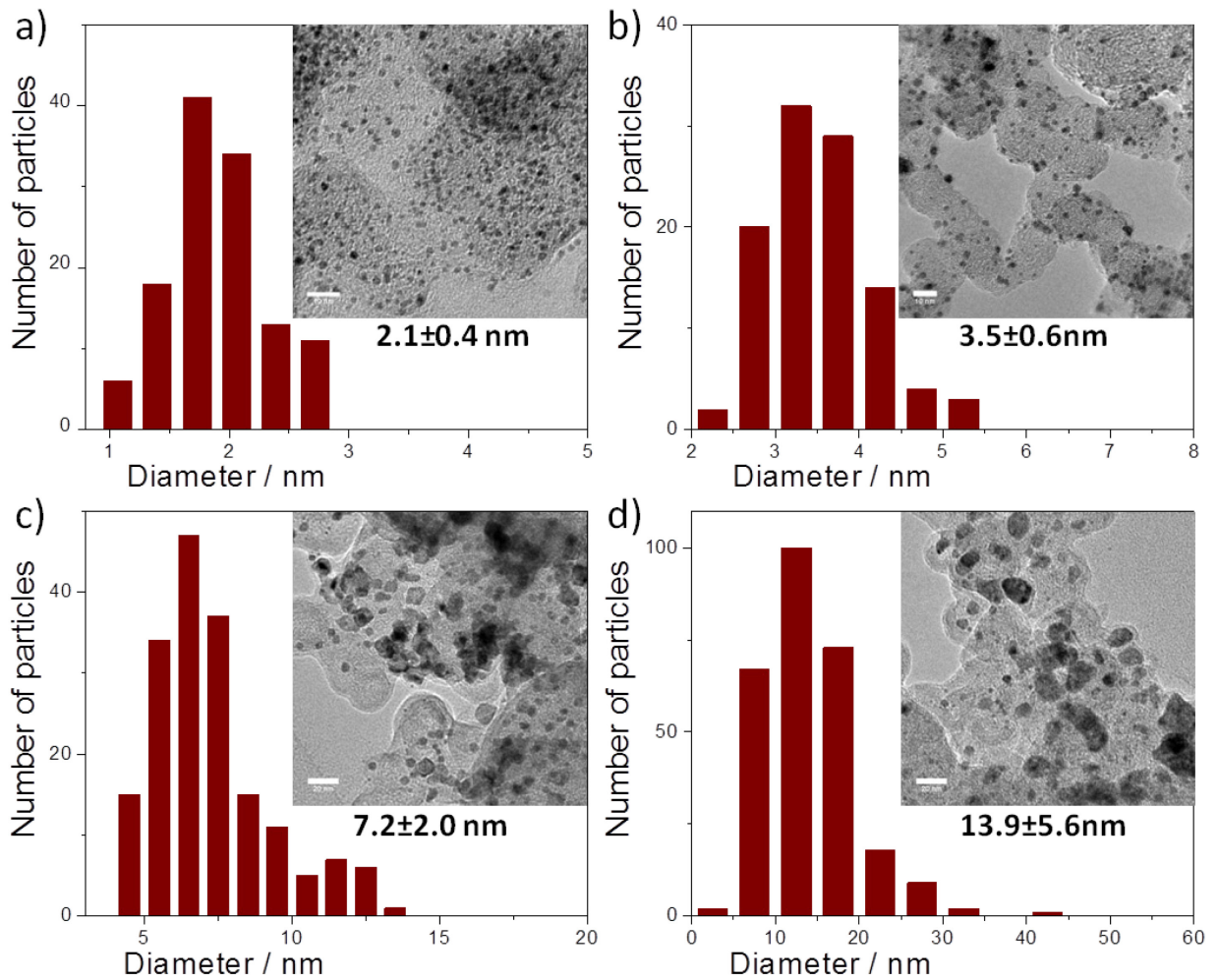


Figure 15. TEM images and particle size histograms of a) Ir, b) IrNi_{2.3}, c) IrNi_{3.3}, and d) IrNi_{5.7} precursor alloys. Scale bars are 10 nm in a) and b); and are 20 nm in c) and d). Reprinted from Ref. 96 with permission of The Royal Society of Chemistry, copyright (2014).

Composition, crystallite size and particle size of Ir and IrNi_x nanoparticles are tabulated in **Table 4**. The number-averaged mean particle sizes are higher than the mean crystallite sizes, probably due to partially amorphous domains inside the alloy particles and/or limitation of the applicability of the simple Scherrer equation to nanoscale clusters.⁹⁷

Table 4. Atomic composition of supported pure Ir and IrNi_x materials and their XRD, TEM based crystallite and particle size analysis

Sample	Weight content of Ir measured by ICP-OES, wt. %	Crystallite size evaluated by Sherrer equation, XRD, Nm	Particle size evaluated from TEM images, nm
Pure Ir	20.4	1.5 ± 0.5	2.1 ± 0.4
IrNi _{2.3}	18.5	5.4 ± 0.4	3.5 ± 0.6
IrNi _{3.3}	15.3	2.9 ± 0.2	7.2 ± 2.0
IrNi _{5.7}	15.4	4.5 ± 0.2	13.9 ± 5.6

To summarize, using the polyol method with optimized conditions according to chapter 3, we successfully synthesized IrNi_x nanoparticles with a wide range of Ni contents but still preserve small particle sizes and the homogeneity of the alloys.

4.3. Preparation of dealloyed IrNi@Ir metallic core-shell nanoparticles (“D-IrNi_x”)

As illustrated in **Figure 13**, the PA-IrNi_x (x = 2.3, 3.3, and 5.7) nanoparticles were electrochemical dealloyed by potential cycling to form the corresponding dealloyed metallic IrNi@Ir core-shell nanoparticles, referred to as D-IrNi_{2.3}, D-IrNi_{3.3}, and D-IrNi_{5.7}, respectively. For comparison, the pure Ir nanoparticles were treated in the same way.

Comparative inspection of the cyclic voltammograms (CVs) of the pristine PA-IrNi_x and dealloyed D-IrNi_x catalysts (**Figure 16a**) showed the typical hydrogen surface electrochemistry of Ir manifested by underpotential hydrogen deposition (H_{upd}) and stripping peaks between +0.05 and +0.4 V. Unlike pure Ir, however, the first scans of the PA-IrNi_x catalysts (dashed lines) displayed an oxidative wave around +0.3 V (best seen for the Ni rich catalysts), evidencing the electrochemical dissolution of surface Ni atoms.⁸⁶ In the CV profiles of D-IrNi_x nanoparticles (solid lines), however, these Ni

oxidation features became absent restoring the typical pure Ir voltammetric shape; we can conclude that, at this point, the dissolution of surface Ni atoms has yielded a stable metallic IrNi@Ir core-shell structure, which will be backed up below by spectroscopy.

The initial electrochemical surface areas (ECSA) of the PA-IrNi_x nanoparticles dropped with increasing Ni content (**Figure 16b**, red columns), which can be explained by increasing particle size and more Ni enriched particle surfaces. In contrast, D-IrNi_{3.3} and D-IrNi_{5.7} nanoparticles showed a 3 and 7 fold enhancement in the ECSA in comparison to their respective pristine state. The trend in ECSA of the dealloyed nanoparticles with increasing Ni content is fully plausible considering that roughness and defect densities increase with more initial surface Ni content.⁸⁶

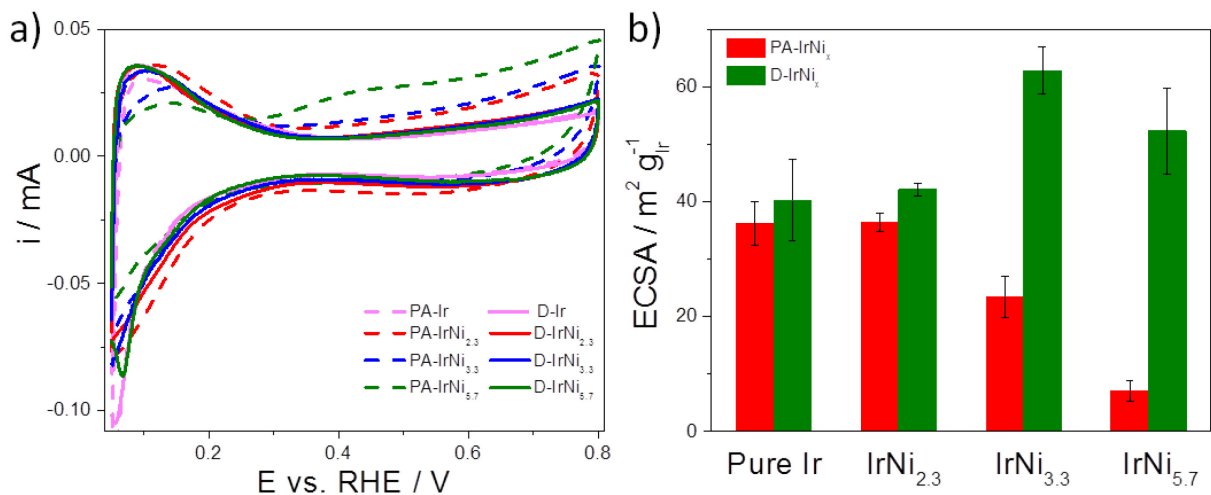


Figure 16. a) Voltammetric profiles of the precursor alloy PA-IrNi_x nanoparticles (dashed) and dealloyed D-IrNi_x nanoparticles (solid) in N₂-saturated 0.05 M H₂SO₄ aqueous solution at 20 mV s⁻¹, and b) Comparison of the electrochemically active surface areas (ECSA) of PA-IrNi_x and D-IrNi_x nanoparticles. Reprinted from Ref. 96 with permission of The Royal Society of Chemistry, copyright (2014).

In order to confirm our hypothesis about the formation of a metallic core-shell structure, and to get further atomic-scale insight into the nanostructure of the catalysts before and after the dealloying, we performed high-angle annular dark-field (HAADF)-scanning transmission electron microscopy (STEM) and STEM-EDX line scans of the IrNi_{3.3} material.

Ir and Ni reveal a significant difference in the atomic number ($Z = 77$ for Ir and $Z = 28$ for Ni), which results in a distinct image contrast between Ir- and Ni-rich specimen regions, similar to Pt and Ni.⁹⁸ The well alloyed PA-IrNi_{3.3} catalyst shows a uniform

contrast distribution with the highest intensity at the center of the particles, appearing as the brightest regions (**Figure 17a**). These contrast features indicate a homogeneous chemical composition. On the other hand, dealloyed nanoparticles (**Figure 17b**) exhibit contrary HAADF patterns, in which nanoparticles show bright Z-contrast rings (shells) surrounding dark inner parts (cores) evidencing the formation of IrNi@Ir core-shell nanostructures.

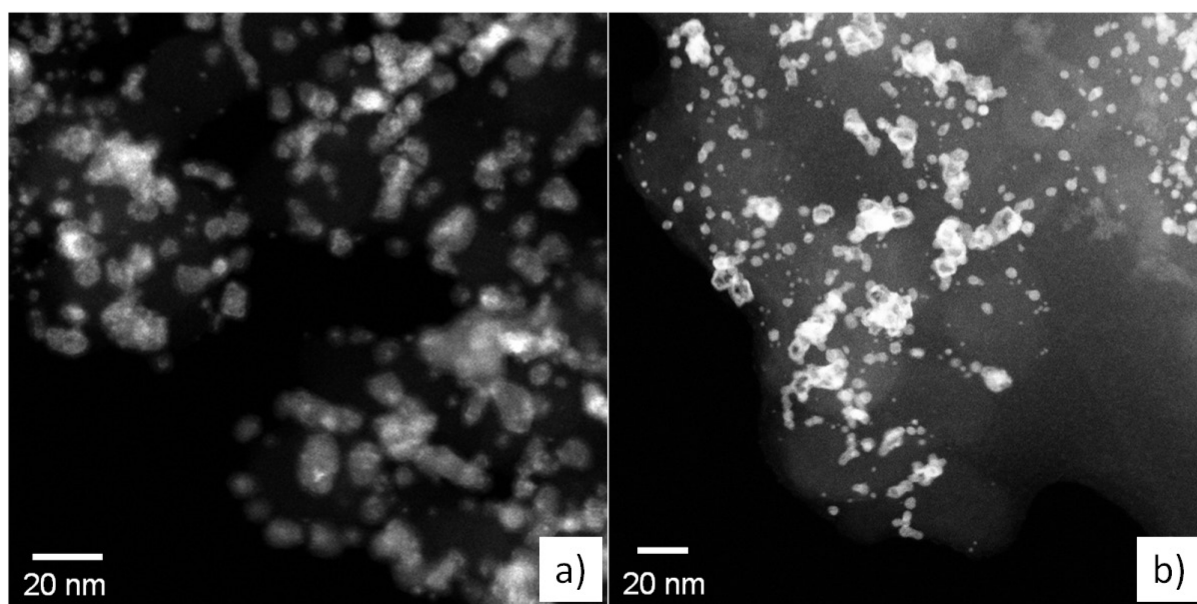


Figure 17. HAADF-STEM images of a) PA-IrNi_{3.3} and b) D-IrNi_{3.3} nanoparticles. Reprinted from Ref. 96 with permission of The Royal Society of Chemistry, copyright (2014).

STEM-EDX line scans of PA-IrNi_{3.3} and D-IrNi_{3.3} nanoparticles (**Figure 18**) corroborate these conclusions unambiguously. Upon dealloying, the homogeneous Ir, Ni distribution yields a core-shell type line scan^{86,99} of D-IrNi_{3.3} with two symmetric Ir shell peaks. Interestingly, the morphology of the dealloyed nanoparticles strongly depended on the particle size, while smaller nanoparticles (~ 5 nm diameter) favoring Ni-rich core-shell structures, larger nanoparticles (~ 10 nm diameter) appear to undergo severe Ni leaching in their transition to core-shell structures, forming hollow core-shell nanoparticle with Ni depleted in the core.

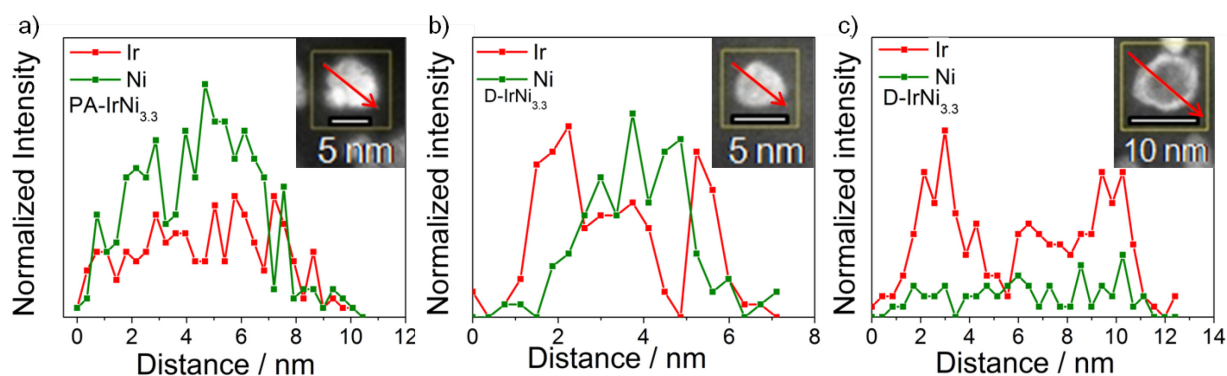


Figure 18. STEM-EDX line profiles of Ir and Ni in a) PA-IrNi_{3.3}, b) and c) D-IrNi_{3.3}. The red arrows in the corresponding nanoparticles (see insets) indicate the directions of the EDX line profiles. Reprinted from Ref. 96 with permission of The Royal Society of Chemistry, copyright (2014).

4.4. Preparation of SO-IrNi@IrO_x and DO-IrNi@IrO_x hybrid core-shell nanoparticles

4.4.1. Electrochemistry of the oxidized core-shell nanoparticles

To prepare the catalytically active core-shell structures, dealloyed IrNi@Ir metallic core-shell particles (D-IrNi_x) were electrochemically cycled up to +1.5V where surface Ir atoms form irreversible oxide species.⁹ Given their stepwise oxidization preparation, these catalysts will be referred to as SO-IrNi_x ($x = 2.3, 3.3,$ and 5.7) to emphasize their precursor material, or equivalently as SO-IrNi@IrO_x to emphasize their chemical structure. For comparison, the homogeneous precursor alloys PA-IrNi_x were subjected to the same cycling protocol in order to achieve simultaneous Ni dealloying and surface Ir oxidation. These samples are referred to as the directly oxidized catalysts, DO-IrNi_x, with a DO-IrNi@IrO_x core-shell structure.

Figure 19a displays the evolution of the surface chemistry of the D-IrNi_{3.3} during voltammetric surface oxidation. The formation of irreversible Ir oxide is clearly evidenced by the diminishing hydrogen adsorption (+0.05 V to +0.4 V) with a strongly emerging Ir^{III/IV} redox wave (+0.8 V to +1.2 V). The characteristic Ir^{III/IV} redox couple (see **Figure 19b**) was used to estimate the molar amount of catalytically active Ir atoms for each catalyst as plotted in **Figure 20**.^{43,100}

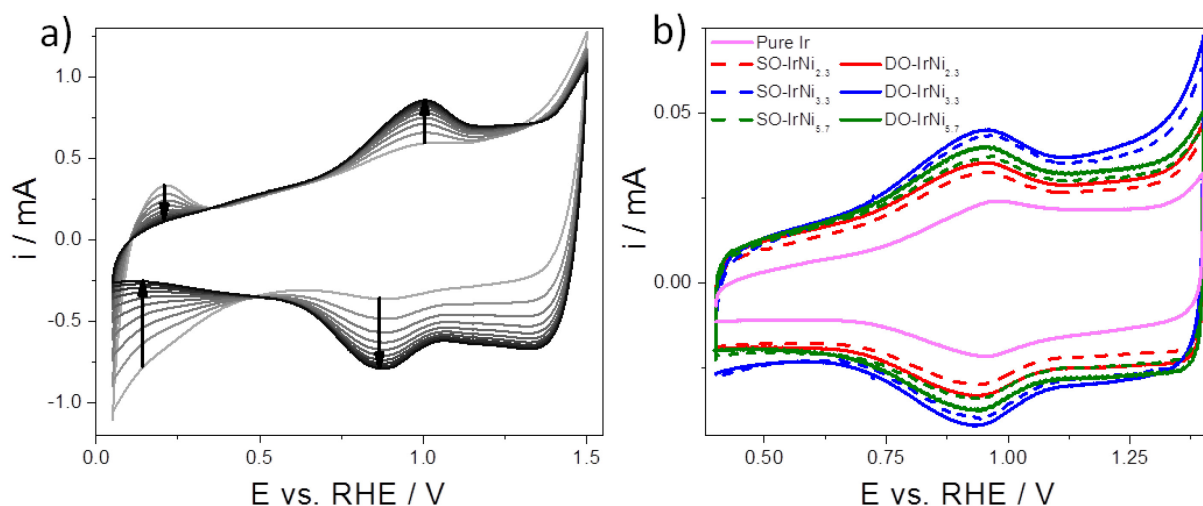


Figure 19. (a) Voltammetric surface oxidation D-IrNi_{3.3} catalyst and (b) Ir (III-IV) redox peaks of SO-IrNi_x and DO-IrNi_x. Reprinted from Ref. 96 with permission of The Royal Society of Chemistry, copyright (2014).

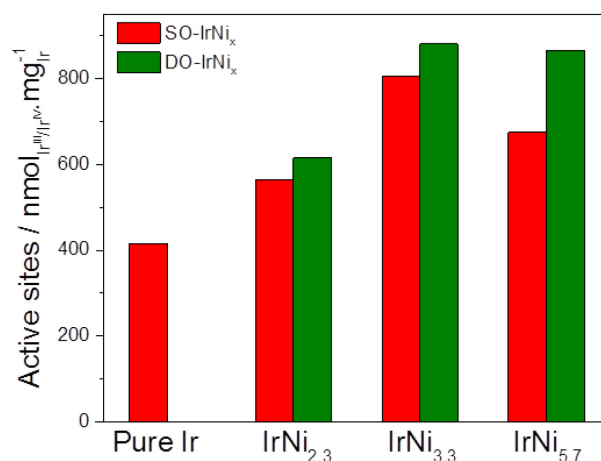


Figure 20. Estimated molar amount of electrochemically accessible Ir redox sites (active sites) per mg of Ir on electrode of stepwise oxidized (SO-IrNi_x) and directly oxidized (DO-IrNi_x) samples.

We are aware of the possibility to overestimate the number of active sites by evaluating the Ir^{III/IV} redox peak, caused by not all of the Ir^{III/IV} sites might involve in OER. However, we still are able to see the trend of the active surface. As expected, IrNi_{3.3} series with the highest ECSA have the highest number of active sites, and all IrNi_x samples have a higher number of active sites than that of pure Ir, in line with ECSA results. DO-IrNi_x samples show higher number of active sites than those of corresponding SO-IrNi_x samples. DO-IrNi_x underwent direct oxidation in which Ni on the top surface layer was dissolved, and the exposed metallic Ir top layer was successively oxidized to Ir oxide in each potential cycling, giving rise to defects and

surface roughness. In contrast, for SO-IrNi_x, Ir metallic shells were formed first (metallic core-shell structure as discussed above) and the Ir metallic atoms on surface had more time to rearrange, lower number of defects and smoothen the surface during the dealloying process. Then the metallic core-shell nanoparticles were oxidized to form oxide core-shell nanoparticles with lower number of active sites compared to that of directly oxidized samples. The higher Ni content in the starting material is, the stronger effect direct oxidation step has on number of active sites, in fact, number of active sites of DO-IrNi_{2.3}, DO-IrNi_{3.3} and DO-IrNi_{5.7} increased ~ 9%, ~ 10 % and ~ 28% compared to SO-IrNi_{2.3}, SO-IrNi_{3.3} and SO-IrNi_{5.7}, respectively.

While we are aware that the values in **Figure 20** likely represent an upper bound of the active OER sites, we used them to calculate intrinsic turn-over-frequency (TOF) type kinetic rates, equivalent to lower bounds of the OER activity. DO-IrNi_x samples showed larger numbers of active Ir sites than SO-IrNi_x samples, presumably due to increased surface roughness and defects because of the massive surface atomic rearrangements during simultaneous dealloying and oxidation.

4.4.2. XPS studies of PA-, SO-, and DO-IrNi_x nanoparticles confirm the metal-oxide hybrid core-shell structure hypothesis

To corroborate our core-shell structure hypothesis further for the metallic IrNi@Ir materials, we performed depth profiled X-ray Photoelectron Spectroscopy (XPS) at different kinetic photoelectron energies (KE) as well as X-ray Absorption Near Edge Structure (XANES).

Typical survey XP spectra (**Figure 21**) showed presence of only expected elements (Ni and Ir from the nanoparticles, C from carbon support, F from Nafion binder, O from oxidized surface of the nanoparticles and the support material) and confirmed the absence of impurities in the precursor alloy or any of the core-shell materials.

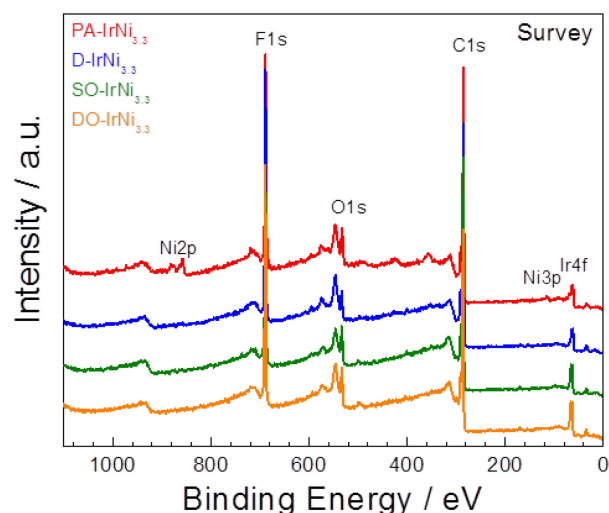


Figure 21. Survey XP spectra of IrNi_{3.3} series: precursor alloy, dealloyed, stepwise oxidized, and directly oxidized IrNi_{3.3} (denoted as PA-, D-, SO-, and DO-IrNi_{3.3}, respectively). Reprinted from Ref. 96 with permission of The Royal Society of Chemistry, copyright (2014).

IrNi_{2.3} series

Here three stages: precursor alloy, stepwise oxidized and direct oxidized samples, denoted as PA-IrNi_{2.3}, SO-IrNi_{2.3}, and DO-IrNi_{2.3}, respectively, were investigated. The precursor alloy PA-IrNi_{2.3} is composed of metallic Ir, some metallic Ni and significant amounts of oxidized Ni (**Figure 22**). Upon direct or stepwise oxidation the Ir 4f shifted to higher binding energy, consistent with the formation of surface IrO_x (**Figure 22a**). When probing more information depth, we found more metallic Ir, and hence metallic Ir still remains in the bulk (**Figure 23**). The XPS Ni 2p region of both SO-IrNi_{2.3} and DO-IrNi_{2.3} (**Figure 22b**, purple and orange lines) clearly proved an essential removal of near surface Ni (see also **Table 5** for quantitative results). Actually, a certain fraction of metallic Ni still remains although its relative content (metallic/oxidized Ni) has been decreased, too. That is, a small amount of Ni is left in the alloyed metallic phase. From this, we can conclude that after electrochemical oxidation, metal-oxide hybrid nanoparticles were formed with IrO_x enriched surface and a metallic alloy in the bulk.

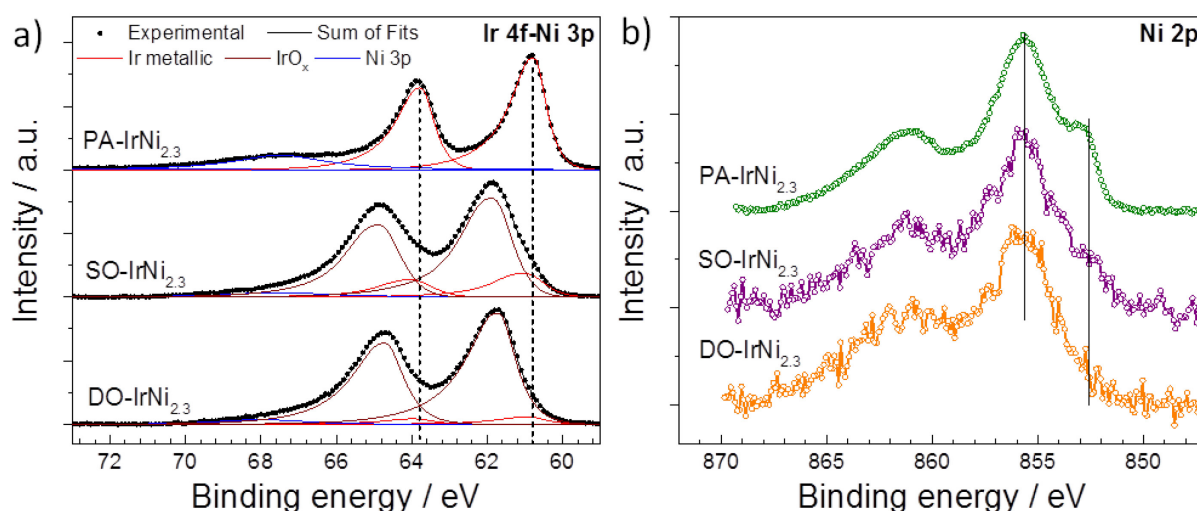


Figure 22. a) Ir 4f and b) Ni 2p core levels of the IrNi_{2.3} series: precursor alloy (PA-IrNi_{2.3}), stepwise oxidized (SO-IrNi_{2.3}) and directly oxidized (DO-IrNi_{2.3}) samples at kinetic energy 550 eV. Vertical dashed lines indicate peak position of metallic Ir.

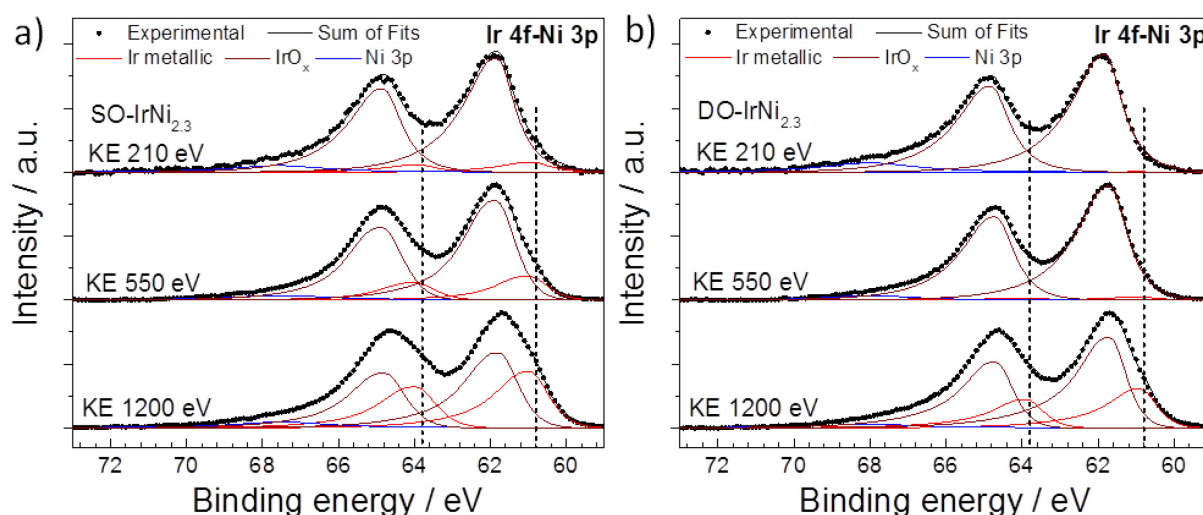


Figure 23. Ir 4f depth profiles of a) stepwise oxidized (SO-IrNi_{2.3}) and b) directly oxidized (DO-IrNi_{2.3}). Vertical dashed lines indicate peak position of metallic Ir.

The carbon 1s core level (**Figure 24**) shows the main peak at around 284.4 eV, corresponding to graphite-like carbon of the support. After oxidation, the peak shifted to higher binding energy, indicating the oxidation of the support as the signals of oxidized C and sp³ carbon species increased significantly in the spectra. There is no big difference between C 1s XPS of stepwise and directly oxidized samples.

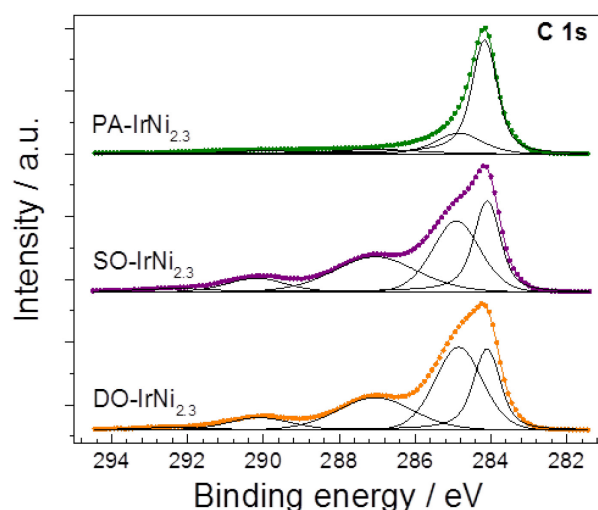


Figure 24. C 1s core levels of the IrNi_{2.3} series (precursor alloy (PA-IrNi_{2.3}), stepwise oxidized (SO-IrNi_{2.3}) and directly oxidized (DO-IrNi_{2.3}) samples) at kinetic energy 550 eV.

IrNi_{3.3} series

The Ni 2p region of PA-IrNi_{3.3} (**Figure 25a**, red lines, solid: 210 eV KE, dotted: 550 eV KE) indicated the prevalence of oxidic Ni species highly reminiscent of NiO.¹⁰¹ This is plausible given the high Ni content of the pristine nanoparticles. A low binding-energy shoulder around 853 eV marked in **Figure 25a** indicates a minor metallic Ni contribution to the overall line shape. Depth profiling of Ni 2p with two different kinetic energies (210 eV and 550 eV) clearly evidenced the metallic component of Ni being more abundant when probing deeper into the nanoparticles. This is consistent with the notion that the core of the particle consists of metallic Ni, while the surface underwent oxidation. Song et al.¹⁰² claimed the formation of ~1 nm oxide layer on Ni nanoparticles occurred during the production or storage period, which might be caused by the non-uniform distribution of defects of nickel crystal structures, i.e. areas with large defects could result in high oxidation levels and vice versa. Similarly, in our case, Ni in the near-surface region of PA-IrNi_{3.3} nanoparticles was oxidized, probably to an amorphous XRD invisible state.

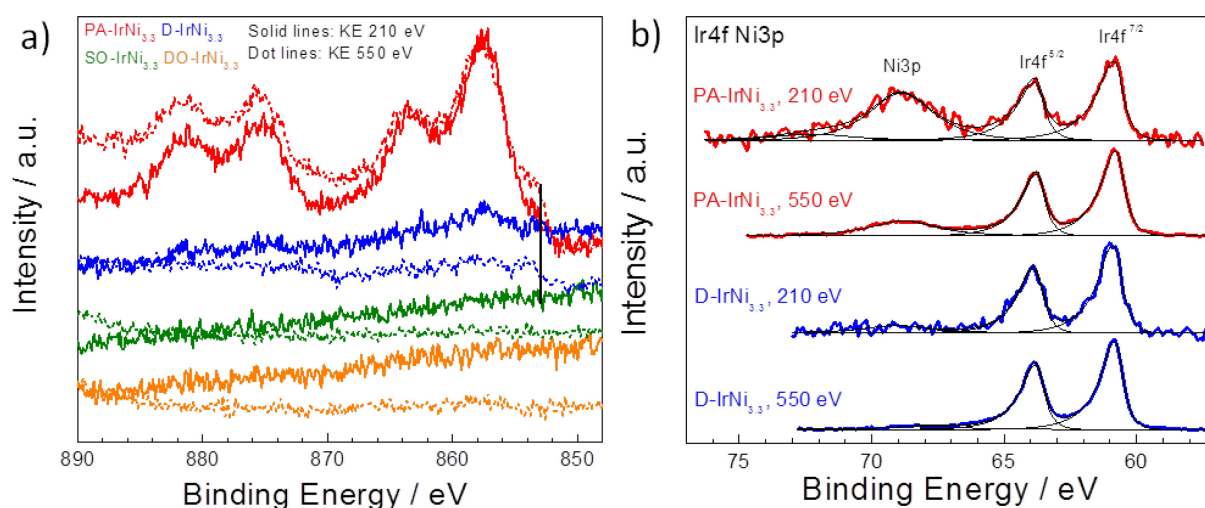


Figure 25. a) Ni 2p of precursor alloy (PA-IrNi_{3.3}), dealloyed (D-IrNi_{3.3}), stepwise oxidized (SO-IrNi_{3.3}) and directly oxidized IrNi_{3.3} (DO-IrNi_{3.3}), and b) Ir 4f XP spectra of PA-IrNi_{3.3} and D-IrNi_{3.3} at kinetic energy (KE) of 210 eV and 550 eV. Vertical line in a) marks the core level shift of metallic Ni. Reprinted from Ref. 96 with permission of The Royal Society of Chemistry, copyright (2014).

Upon dealloying, we recorded dramatically reduced NiO_x intensities (blue solid, 210 eV KE, and dotted lines, 550 eV KE), a nearly six-fold reduction in the estimated Ni/Ir molar ratio (see **Table 5**), and a sustained contribution of metallic Ni⁰ in the subsurface region. All these findings are in excellent agreement with expectations and microscopic data and strengthened our hypothesis as to the electrochemical formation of a metallic IrNi@Ir core-shell catalyst structure.

The XPS Ir 4f region of the PA-IrNi_{3.3} and D-IrNi_{3.3} catalysts (see **Figure 25b**) indicated the prevalence of metallic Ir⁰ (BE ~60.8 eV). Interestingly, the Ir 4f region overlapped with the Ni 3p region. This is why Ni-related 3p peaks appear. These peaks corroborated our conclusions from the 2p region: Ni 3p of the precursor alloy evidenced a NiO_x-covered surface. After dealloying, Ir remained in fully metallic state; however the intensity of Ni 3p significantly decreased commensurate with the selective removal of Ni from the surface.

XANES Ni L edge spectra of PA-IrNi_{3.3} and D-IrNi_{3.3} (**Figure 26a**) revealed slight but characteristic differences, suggesting more NiO contribution (~855 eV) in the PA-IrNi_{3.3} catalyst, whereas more metallic Ni⁰ contributions in the D-IrNi_{3.3} material (satellite structure in **Figure 26** at 859 eV) were identified in line with the XPS results.

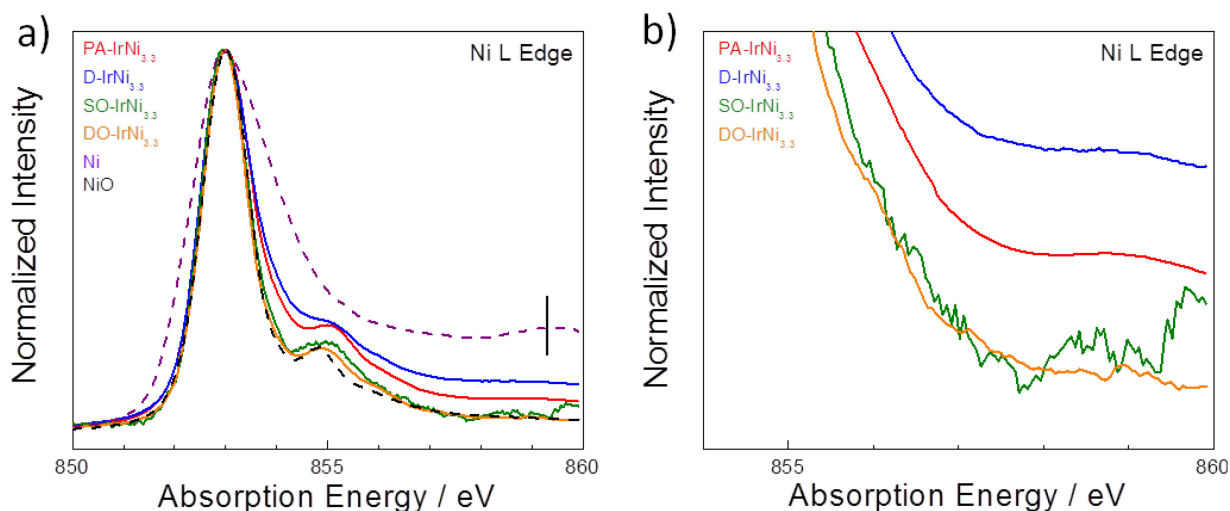


Figure 26. a) Ni L-edge XANES of the IrNi_{3.3} series: precursor alloy, dealloyed, stepwise oxidized, and directly oxidized IrNi_{3.3} (denoted as PA-, D-, SO, and DO-IrNi_{3.3}, respectively), and b) a zoom on a tiny shoulder around 859 eV. Reprinted from Ref. 96 with permission of The Royal Society of Chemistry, copyright (2014).

Depth resolved Ir 4f core level spectra of the SO-IrNi_{3.3} and DO-IrNi_{3.3} catalysts (**Figure 27**) were clearly shifted to higher binding energy compared to metallic Ir, consistent with the formation of surface IrO_x. The Ir 4f XPS at low KE 210 eV indicated that Ir atoms in the surface layer were completely oxidized; however, spectra at higher KE (550 and 1200 eV) also showed that metallic Ir components were present at larger information depth. This corroborates our structural hypothesis that the nanoparticle cores of the catalysts still contain a metallic alloy.

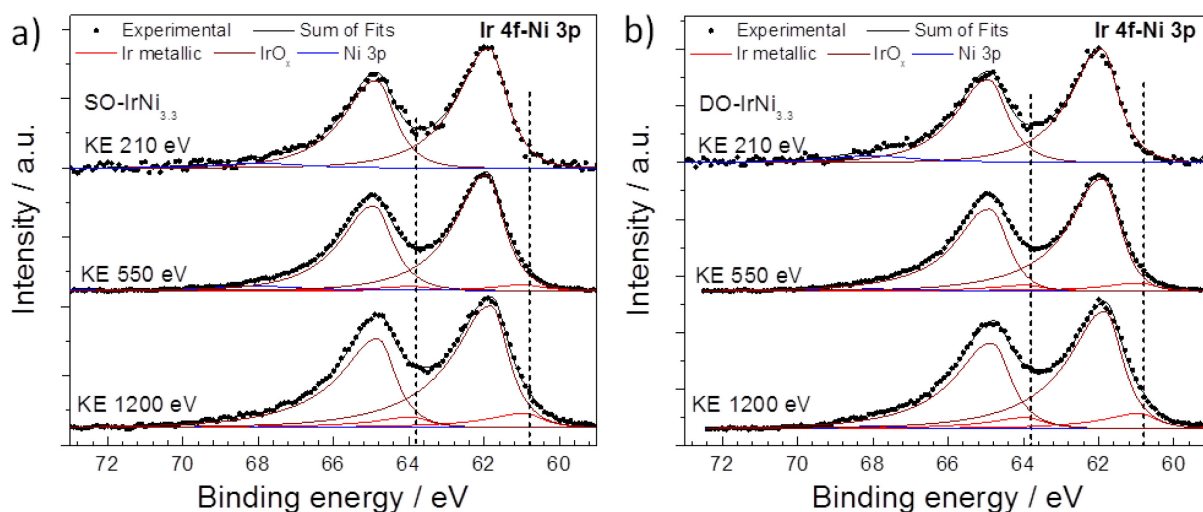


Figure 27. Ir 4f core level spectra of (a) SO-IrNi_{3.3} and (b) DO-IrNi_{3.3} at KE 210, 550 and 1200 eV. Dashed lines indicate peak position of metallic Ir as found in PA-IrNi_{3.3}. Reprinted from Ref. 96 with permission of The Royal Society of Chemistry, copyright (2014).

IrNi_{5.7} series

Here again three states: precursor alloy, stepwise oxidized and direct oxidized samples were investigated. Similar trends were observed as above: the precursor alloy is composed of metallic Ir, some metallic Ni and significant amounts of oxidized Ni (**Figure 28**). Upon direct or stepwise oxidation most of the Ir has been oxidized, but some metallic Ir is still kept in the bulk (**Figure 29**). The Ni content has been drastically reduced; the relative content of metallic Ni (metallic/oxidized Ni) has been decreased, too (**Figure 28b**), but probably less than with IrNi_{2.3} series.

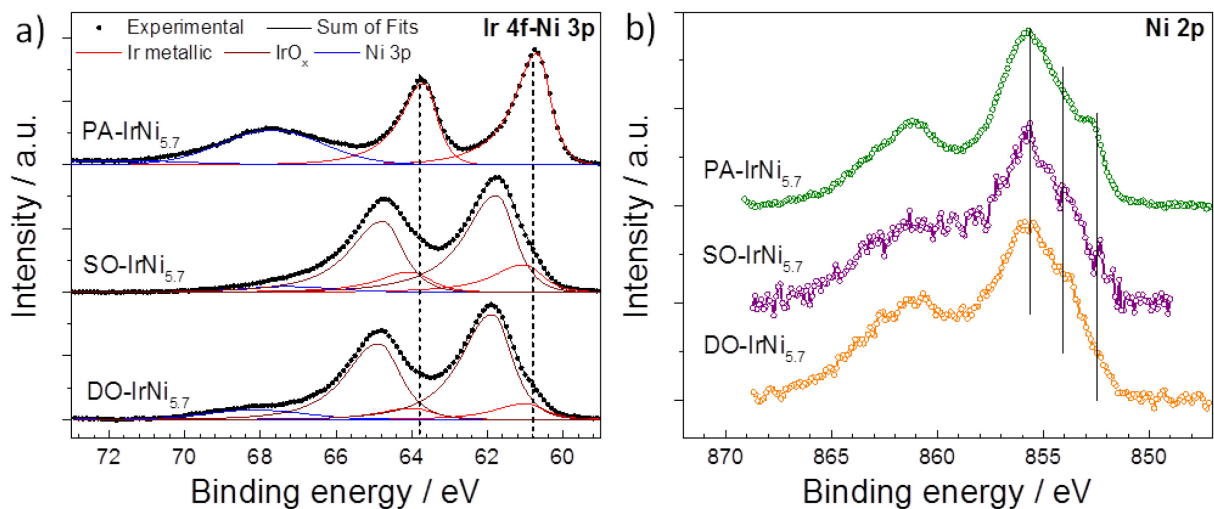


Figure 28. a) Ir 4f and b) Ni 2p core levels of the IrNi_{5.7} series (precursor alloy (PA-IrNi_{5.7}), stepwise oxidized (SO-IrNi_{5.7}) and directly oxidized (DO-IrNi_{5.7}) samples) at kinetic energy 550 eV. Vertical dashed lines indicate peak position of metallic Ir.

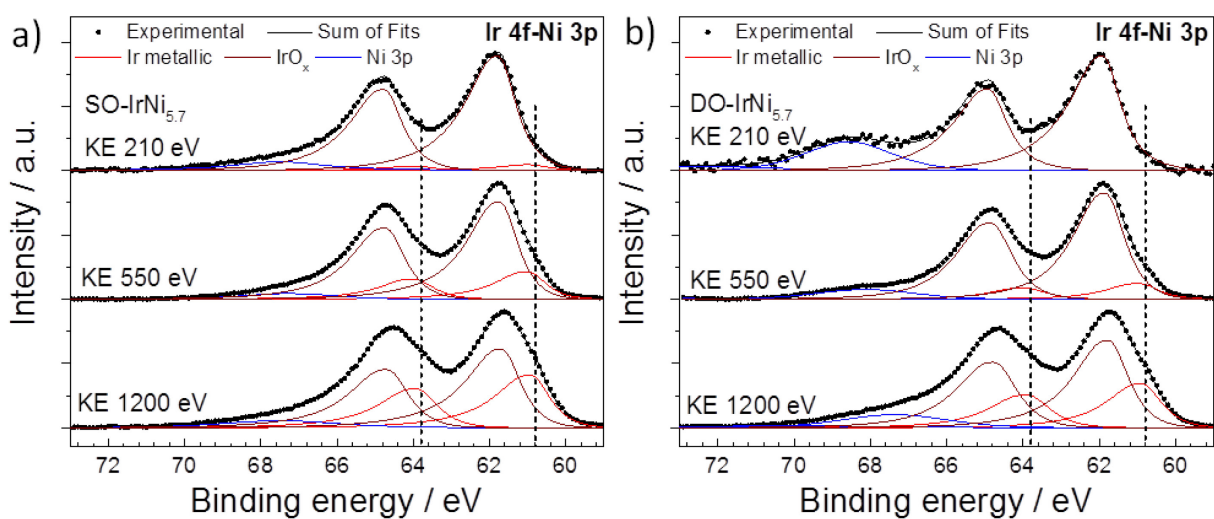


Figure 29. Ir 4f depth profile of a) stepwise oxidized (SO-IrNi_{5.7}) and b) directly oxidized (DO-IrNi_{5.7}). Vertical dashed lines indicate peak positions of metallic Ir.

It should be noted here that the shape of the Ir 4f peaks lacks the characteristic asymmetry of IrO₂,¹⁰³ suggesting that the Ir oxide component here cannot be IrO₂ itself, but rather a mixture of ill-defined oxide-hydroxide, with potentially numerous defects and thus varying oxidation states.¹⁰⁴ Concerning the thickness and stability of the formed Ir oxide layer, as well as the real oxidation states of Ir after oxidation step and oxygen evolution reaction, further investigation is necessary.

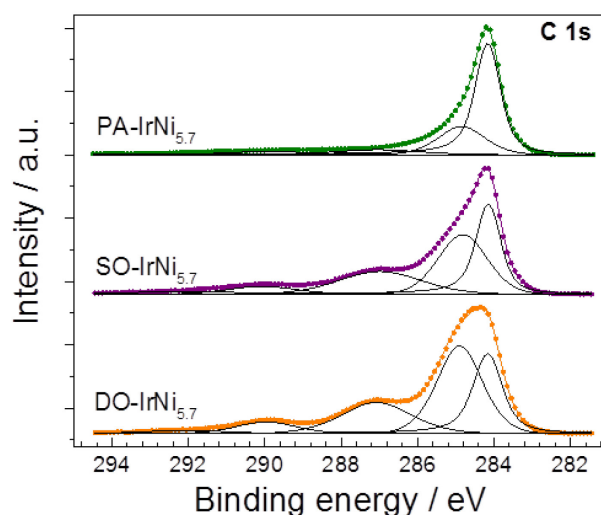


Figure 30. C 1s core level spectra of the IrNi_{5.7} series (precursor alloy (PA-IrNi_{5.7}), stepwise oxidized (SO-IrNi_{5.7}) and directly oxidized (DO-IrNi_{5.7}) samples) at kinetic energy 550 eV.

Similar to IrNi_{2.3} series, the carbon 1s core level (**Figure 30**) shows the main peak at around 284.4 eV, corresponding to graphite-like carbon of the support. After oxidation, significant amounts of oxidized C and sp³ carbon appeared in the spectra, indicating the oxidation of the carbon support.

Surface composition of PA-, SO- and DO-IrNi_x samples is compiled in **Table 5**. As expected, the Ni content has been drastically reduced after stepwise or direct oxidation. If we compare the Ni/Ir ratios of the various series, there is not much correlation with the nominal precursor alloy composition, especially for SO- samples. SO- and DO-IrNi_{3.3} show much less Ni content after oxidation compared to their parent alloy, while in SO-, DO-IrNi_{2.3} and SO-, DO-IrNi_{5.7}, the Ni content remained higher after oxidation.

Table 5. Quantitative XPS results of IrNi_x series ($x = 2.3, 3.3, \text{ and } 5.7$): precursor alloy (PA-IrNi_x), stepwise oxidized (SO-IrNi_x) and directly oxidized (DO-IrNi_x) measured in UHV at kinetic energy 550 eV.

Sample series	Ni/Ir ratio			O/(Ir+Ni) ratio		
	PA-	SO-	DO-	PA-	SO-	DO-
IrNi _{2.3}	2.3	0.27	0.31	1.4	3.7	4.0
IrNi _{3.3}	6.1	0.09	0.14	1.6	5.2	4.1
IrNi _{5.7}	7.5	0.33	1.6	1.6	3.5	4.2

All in all, the extensive and comprehensive HAADF-STEM, STEM-EDX, XANES, and XPS studies evidence the successful synthesis of metallic and metal-oxide hybrid core-shell nanoparticles by selective removal of Ni and Ir surface oxidation, which confirms our structural hypotheses illustrated in **Figure 13**.

4.5. Electrochemical OER activity of IrNi@IrO_x core-shell nanoparticles

In order to correlate the structural and electronic parameters obtained in the previous sections 4.2, 4.3, and 4.4 with the surface catalytic activity for the oxygen evolution reaction (OER) activities under acidic conditions similar to those of PEM electrolyzers, the SO-IrNi@IrO_x and DO-IrNi@IrO_x core-shell catalysts were subjected to a cyclic voltammetry protocol in a highly acidic electrolyte (see OER test protocol in section 2.3.3). The iR corrected linear sweep voltammetry of all catalysts with their Ir-mass based and specific activities (iR and capacitance corrected) at 0.25 V overpotential are presented in **Figure 31**.

Obviously, all Ni-containing nanoparticle catalysts are significantly more active for the OER on a mass and active site-specific basis than pure Ir. The most active catalysts are the SO-IrNi_{3.3} and the DO-IrNi_{3.3} showing a 3 times higher mass activity compared to pure Ir at 250 mV overpotential. This implies a three times higher electrolyzer hydrogen output at constant input voltage. The directly oxidized core-shell catalysts showed even slightly higher OER mass activities than those of

stepwise oxidized samples, most likely due to higher surface roughness and more catalytic sites.

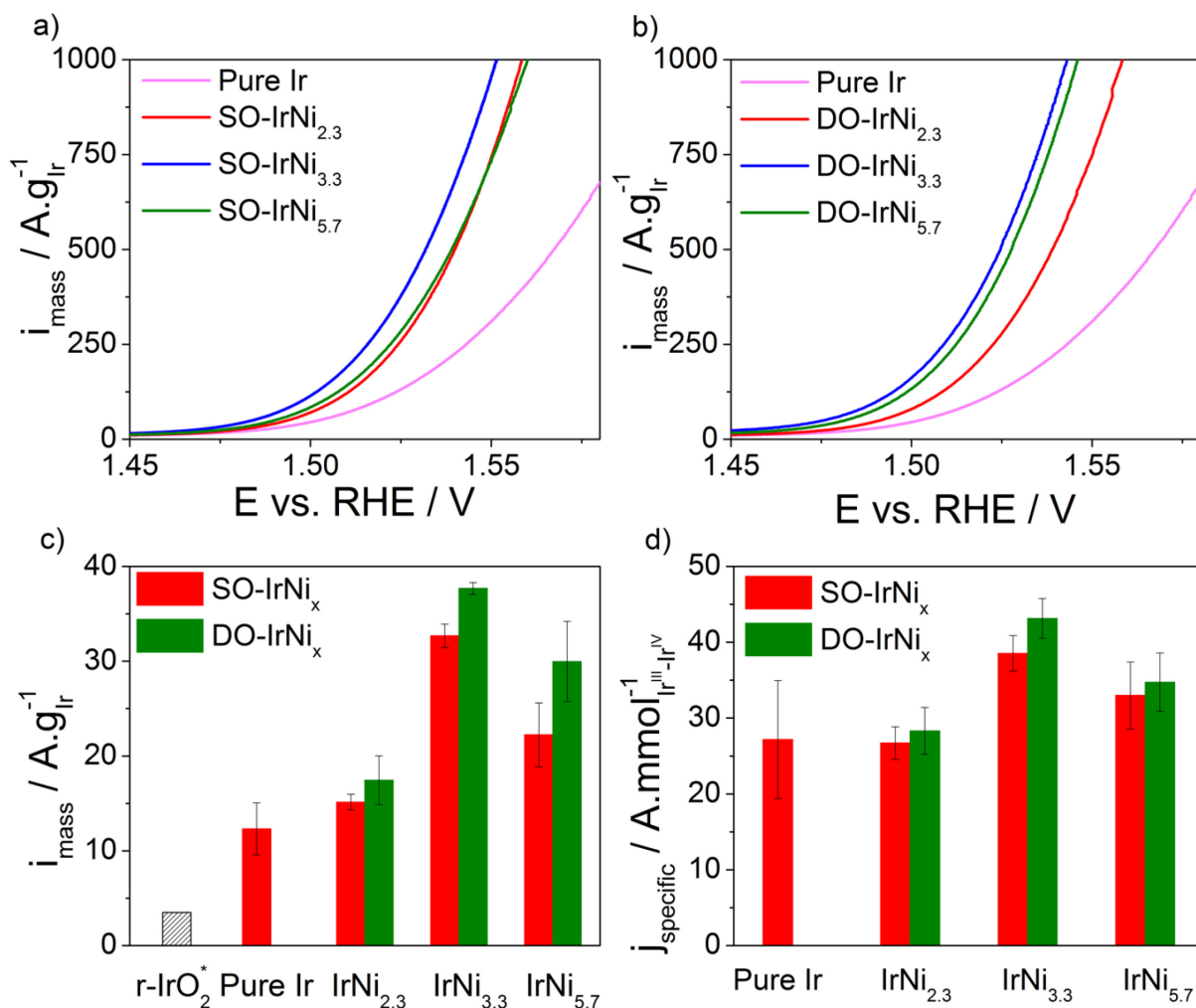


Figure 31. Linear sweep voltammetry as catalytic oxygen evolution reaction (OER) activities of a) stepwise oxidized (SO) IrNi_x and b) directly oxidized (DO) IrNi_x core-shell nanoparticle catalysts, in comparison to pure Ir nanoparticles. c) Ir mass based activities and d) specific activities at 0.25V overpotential. Conditions: 0.05 M H₂SO₄, 1600 rpm, scan rate 5 mV s⁻¹. “r-IrO₂” denotes the Ir-mass based activity of IrO₂ rutile-type nanoparticles at 0.25V overpotential.⁷¹ Reprinted from Ref. 96 with permission of The Royal Society of Chemistry, copyright (2014).

In comparison to literature, our IrNi@IrO_x metal/oxide core-shell nanoparticle catalysts showed substantially higher mass activities, even compared to a rutile-type iridium oxide particle catalyst (“r-IrO₂” in **Figure 31c**), which is often taken as a benchmark Ir OER catalyst.⁷¹ In particular, at 250 mV overpotential, the DO-IrNi_{3.3} core-shell catalyst exhibited a 10 times higher mass activity than r-IrO₂. Moreover, although ruthenium has been reported to be the most active catalyst for OER in acidic media, all of our Ni-containing catalysts are more active for the OER than a

rutile-type r-RuO₂ nanoparticle catalyst (Ru mass activity of 14.5 A g⁻¹_{Ru} compared to ~ 40 A g⁻¹_{Ir} for DO-IrNi_{3.3}, an almost 3 times activity enhancement).⁷¹ At a higher overpotential of 370 mV (1.60 V vs. RHE), Wei Hu et al.¹⁰⁵ reported a noble metal mass activity of three-dimensional ordered macroporous IrO₂ of 500 A g⁻¹_{Oxide} (or 583 A g⁻¹_{Ir}); for comparison, our DO-IrNi_{3.3} reaches this same value already at 1.530V vs. RHE corroborating the mass efficient OER catalysis. In terms of Ir-site based specific activities, the IrNi_{2.3} sample shows a similar activity to pure Ir, while the two Ni-richer samples (IrNi_{3.3} and IrNi_{5.7}) showed substantially higher specific OER activities than pure Ir, however the enhancement remain below the mass-based value. This is explained by the fact that the number of active sites is an upper bound, rendering the presented specific activities a lower bound of the actual specific OER activities.

If we compare the Ni/Ir ratios of all the SO- and DO-IrNi_x samples, there is no clear correlation with the specific OER activity. The most active catalysts, SO-IrNi_{3.3} and DO-IrNi_{3.3} have the smallest Ni content on surface compared to the other samples; however, SO- and DO-IrNi_{2.3} show a lower OER activity than SO- and DO-IrNi_{5.7}, although the Ni content is smaller (**Table 5**).

Chronopotentiometric stability measurements were carried out at room temperature in aqueous 0.05M H₂SO₄ electrolyte for pure Ir and DO-IrNi_{3.3} nanoparticles (**Figure 32**).

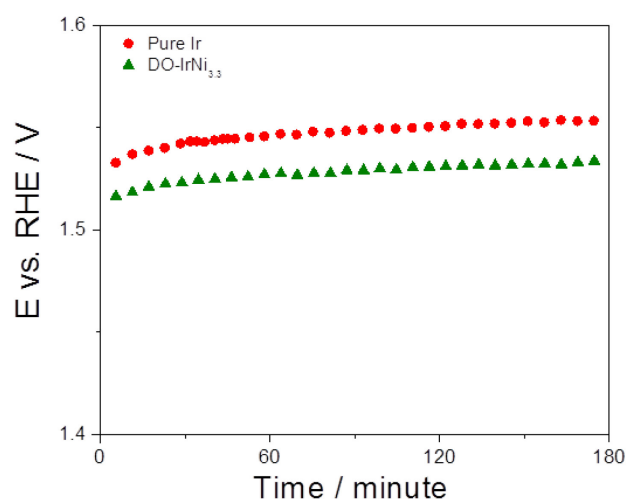


Figure 32. Chronopotentiometric measurements of pure Ir and directly oxidized (DO) IrNi_{3.3} core-shell nanoparticles at a current density of 1 mA cm⁻². Reprinted from Ref. 96 with permission of The Royal Society of Chemistry, copyright (2014).

The potential in the chronopotentiometric measurements increased slightly during the first 30 minutes and then remained constant throughout the tests, indicating stable behavior of the nanocatalysts.

Ir 4f XP spectra at KE 550 eV of directly oxidized IrNi_{3.3} before (denoted as DO-IrNi_{3.3}) and after stability test (denoted as DO-IrNi_{3.3}-Stabil) are compared in **Figure 33**.

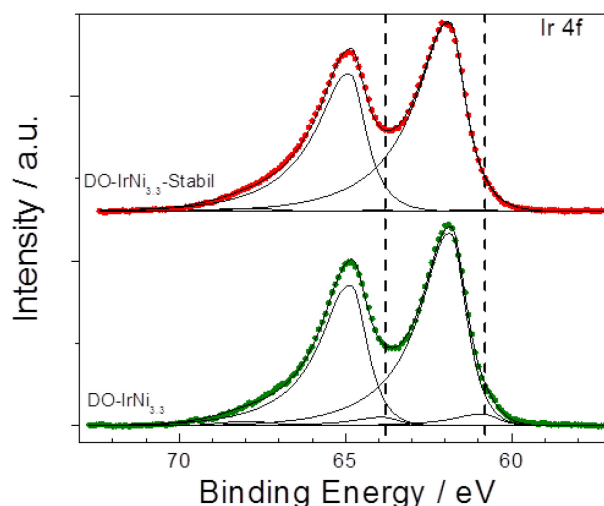


Figure 33. Ir 4f XPS of directly oxidized IrNi_{3.3} at KE 550 before (bottom graph, denoted “DO-IrNi_{3.3}”) and after the stability test (top graph, denoted “DO-IrNi_{3.3}-Stabil”) with Ir 4f peak position derived from PA-IrNi_{3.3} at KE 550 eV (dash lines) as standard for the metallic Ir component. Reprinted from Ref. 96 with permission of The Royal Society of Chemistry, copyright (2014).

The shape of the Ir 4f spectra was quite similar, though the fits suggest that a small metallic contribution of the DO-IrNi_{3.3} sample decreased further during the stability test. This indicates a prolonged oxidation of the particles from the outside in to larger and larger depths. The composition evaluation of DO-IrNi_{3.3}-Stabil resulted in an Ir/Ni ratio of 0.045, showing that Ni was further removed from surface region during the stability test.

4.6. Summary

We have presented a family of dealloyed metal-oxide hybrid ($M_1M_2@M_1O_x$) core@shell nanoparticle catalysts and have demonstrated, exemplified by the IrNi@IrO_x system that this structural and compositional class of nanocatalysts offers substantial advances in terms of more efficient and less expensive electrolytic water splitting for PEM electrolyzer applications.

Using extensive microscopic and spectroscopic analysis, largely with depth resolution, we followed the evolution of the IrNi@IrO_x metal oxide core-shell particles step-by-step from their IrNi bimetallic precursor stage, through the metallic core-shell stage to the final oxide shell/ alloy core architecture. The final catalysts have an almost pure IrO_x surface, while the inner core region became increasingly metallic and richer in Ni.

Correlating the structural characteristic with the OER activity we concluded that the core-shell catalysts perform substantially more active (about 3x higher compared to electrochemically oxidized Ir and rutile-type RuO₂, and 10x higher compared to rutile-type IrO₂) and thus thermodynamically more efficient on a noble metal mass and an active site basis during the electrocatalytic oxygen evolution.

The dealloyed metal-oxide hybrid ($M_1M_2@M_1O_x$) core-shell catalyst concept represents a quite general strategy to lower the noble-metal content of nanoparticle oxide catalysts for other technologies or application, including but not limited to energy storage and conversion such as electrolyzers, supercapacitors, or metal-air batteries. Deploying the current catalysts in PEM electrolyzer anodes, for instance, offers the prospect of lowering the required Ir content for a given hydrogen production rate by a full factor of 3.

*This page
intentionally
left blank*

5. Oxide-Supported IrNiO_x Core-Shell Particles as Efficient, Cost-Effective, and Stable Catalysts for Electrochemical Water Splitting

[Ref. 106] - Reproduced with permission of John Wiley and Sons, copyright (2015).

In this chapter, active and highly stable oxide-supported IrNiO_x core-shell catalysts for electrochemical water splitting are presented. IrNi@IrO_x nanoparticles supported on high-surface-area mesoporous antimony-doped tin oxide (IrNiO_x/Meso-ATO-T) were synthesized from bimetallic IrNi_x precursor alloys annealed at different temperatures T (PA-IrNi_x/Meso-ATO-T) using electrochemical Ni leaching and concomitant Ir oxidation. Special emphasis was placed on Ni/NiO surface segregation during the thermal treatment of the PA-IrNi_x/Meso-ATO-T as well as on the surface chemical state of the particle/oxide support interface. Combining a wide array of characterization methods, we uncovered the detrimental effect of segregated NiO phases on the OER activity of IrNiO_x core-shell particles. The core-shell IrNiO_x/Meso-ATO catalyst displayed high OER activity and unprecedented stability in acidic electrolyte providing substantial progress in the development of PEM electrolyzer anode catalysts with drastically reduced Ir loading and significantly enhanced durability.

We address the challenges related to noble metal content and durability of OER catalysts presenting a low-Ir content catalyst with previously unachieved electrochemical performance durability. To accomplish this goal, we utilized a conductive, corrosion-resistant oxide material with exceptionally high surface area to support Ir-Ni oxide nanoparticles with a IrNi@IrO_x core-shell architecture.⁹⁶ The core-shell structure helped to tune the intrinsic electrocatalytic activity, while lowering the Ir content significantly. The IrNiO_x core-shell structure was obtained from IrNi nanoparticle precursor alloys using electrochemical selective dealloying of Ni and a simultaneous surface oxidation of the surface Ir atoms resulting in the IrO_x shells. Emphasis was placed on an atomic-scale understanding of surface and bulk chemical transformation and segregation during the preparation and during the catalytic operation of the core-shell catalysts. To the best of our knowledge, this is the first report of a low-Ir content core-shell oxide catalyst combined with a corrosion-stable oxide support resulting in a highly active and remarkably stable water splitting electrocatalyst.

5.1. Structure evolution of IrNi_x/Meso-ATO precursor alloys under thermal treatment

A number of different IrNi_x ($x = 3.3$ to 3.8) nanoparticle precursor alloys supported on mesoporous antimony doped tin oxide were prepared using the optimized polyol method (see chapter 3 and section 2.1.4). The obtained precursor alloys were denoted as PA-IrNi_x/Meso-ATO-T, and later used for the synthesis of core-shell structured catalysts (IrNiO_x/Meso-ATO-T). For comparison, pure Ir nanoparticles supported on commercial ATO (Ir/com.-ATO) and carbon (Ir/C) were also synthesized. The detailed synthesis and annealing protocols of the support and catalysts are presented in chapter 2.

The TEM image of the Meso-ATO powder (**Figure 34a**) shows a mesoporous, foam-like structure consisting of interconnected nanoparticles with exceptional monodispersity. This structure provides a surface area as high as $264 \text{ m}^2 \text{ g}^{-1}$ and thus is much higher than that of commercial ATO (Sigma Aldrich, $\sim 47 \text{ m}^2 \text{ g}^{-1}$).¹⁰⁷ IrNi_x alloy nanoparticles showed a fairly homogeneous dispersion with a few small agglomerated clusters (**Figure 34b**). The IrNi_x nanoparticle size distributed in the range of $7.3 \pm 2.5 \text{ nm}$ (**Figure 34b**, inset).

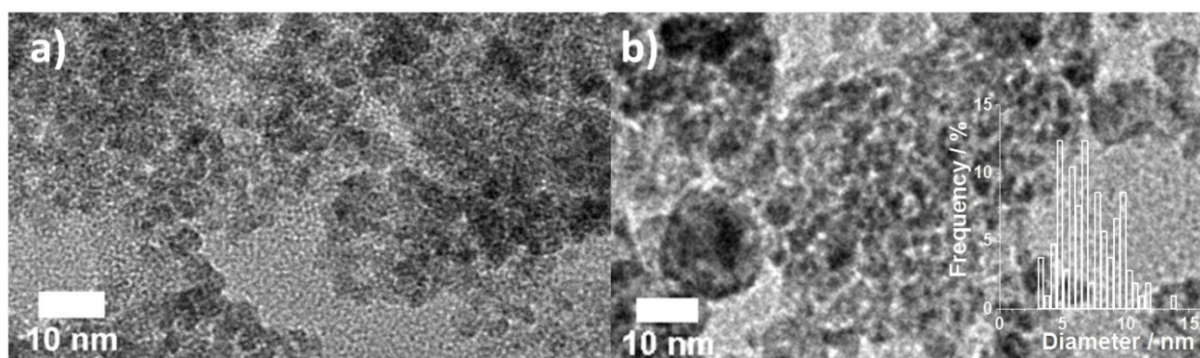


Figure 34. TEM images of a) mesoporous antimony doped tin oxide (Meso-ATO), b) Meso-ATO supported IrNi_{3.3} nanoparticle precursor alloy annealed at 180 °C (PA-IrNi_{3.3}/Meso-ATO-180), inset: particle size distribution of IrNi_{3.3} nanoparticles in PA-IrNi_{3.3}/Meso-ATO-180. Reprinted from Ref. 106 with permission of John Wiley and Sons, copyright (2015).

The preparation of metallic alloy nanoparticles supported on redox active oxides and the removal of capping agents require a careful optimization of a balanced annealing protocol in order to maintain the chemical state of alloy and support. In this study, the materials were annealed in inert N₂ gas, as opposed to our previous procedure in H₂ (see section 2.1.4),⁹⁶ to prevent the reduction of the ATO support. The thermal

treatment of a bimetallic nanoalloy in different gas atmospheres could lead to different atomic segregation phenomena, affecting the catalytic reactivity of the alloy.¹⁰⁸ Therefore, we first investigated the effects of the thermal treatment on the atomic structure of the PA-IrNi_x/Meso-ATO-T and on the OER activity of the obtained core-shell catalysts. The structure of the PA-IrNi_x/Meso-ATO-T were comprehensively studied by powder X-ray diffraction patterns (XRD), X-ray photoelectron spectroscopy (XPS) and high energy XRD coupled with atomic pair distribution function (HE-XRD atomic PDFs).

XRD patterns of PA-IrNi_x/Meso-ATO-T (**Figure 35**) with $T \leq 400$ °C showed typical reflections between 40 and 45°, corresponding to (111) planes of the alloy crystallites.⁹⁶ The reflections dropped in intensity and shifted to smaller 2θ with increasing T , indicating enrichment in Ir at decreased crystallite size of the alloys. The XRD pattern of the sample treated at 500 °C (**Figure 35**, orange line) shows additional reflections corresponding to NiO, indicating the transformation of metallic Ni to an oxide.

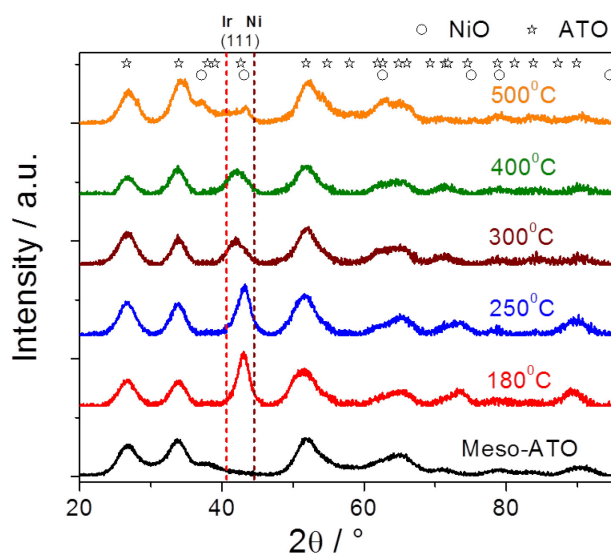


Figure 35. XRD patterns of mesoporous antimony doped tin oxide (Meso-ATO) supported IrNi_x precursor alloys annealed at different temperatures T (T is given by each data set), vertical dashed lines indicate (111) database reflections of pure metallic Ir and Ni; open cycles and stars indicate database main reflections of NiO and antimony doped tin oxide, respectively. Reprinted from Ref. 106 with permission of John Wiley and Sons, copyright (2015).

Core level photoemission spectra in the Ir 4f Ni 3p range of the PA-IrNi_x/Meso-ATO-T materials (**Figure 36a**) confirmed the presence of metallic Ir at the surface for $T < 500$ °C. Annealing the supported nanoparticles at 500 °C leads to oxidation of Ir

on surface. Notice the varying amount of Ni 3p at the high binding energy side (~ 68 eV) of Ir 4f. In the XPS Ni 2p(3/2) spectra of IrNi_x/Meso-ATO-T (**Figure 36b**), the most intense Ni 2p(3/2) line is situated at ~ 856 eV, with the satellite at ~ 862 eV, similar to what was observed before for Ir-Ni nanoparticles on carbon.⁹⁶ Although the binding energy is much up-shifted compared to crystalline NiO, the shape of Ni 2p with the strong satellite and characteristic satellite main peak separation suggest a Ni²⁺ state. The low-T annealed samples reveal a clear low binding energy component at ~ 852.6 eV, which is characteristic of metallic Ni. Thus after low-T annealing ($T \leq 300$ °C), the samples contain an alloyed metallic Ir-Ni phase. For samples annealed at 400 and 500 °C, a low binding energy component appears which fits well to crystalline NiO. Thus, we conclude that only the low-T samples maintained the desired Ir-Ni metallic alloy phase suited for dealloying and core-shell nanoparticle formation.

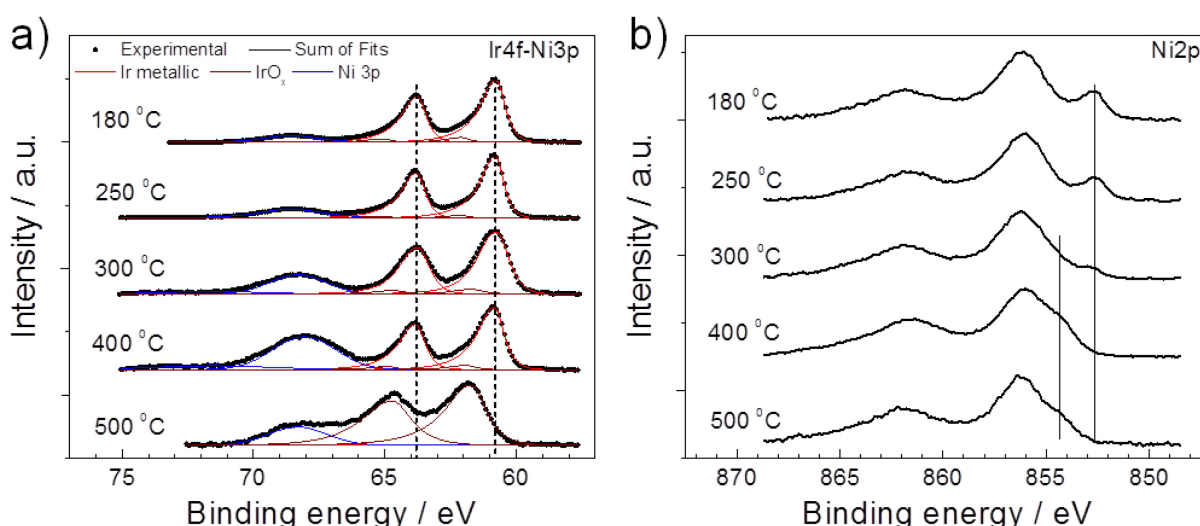


Figure 36. XP spectra of supported IrNi_x precursor alloys annealed at different temperatures T (T is given by each data set). a) Ir 4f Ni 3p XPS, and b) Ni 2p XPS. All spectra were measured at a kinetic energy of 550 eV. Vertical dashed lines indicate peak positions of metallic Ir. Reprinted from Ref. 106 with permission of John Wiley and Sons, copyright (2015).

Surface (derived from XPS at KE of 550 eV) and bulk compositional analysis (performed by ICP-OES) of the IrNi_x/Meso-ATO-T samples (**Table 6**) revealed an increasing Ni excess in the particle surface, peaking at 400 °C. This points to Ni segregation of amorphous and, at higher T , crystalline Ni oxide phases and is quite similar to Ni segregation reported in PtNi nanoparticles.¹⁰⁸ At 500 °C, both Ni and Ir

display an oxidized chemical state. The Sb/Sn ratio decreased compared to as-prepared Meso-ATO when annealed at $T \geq 300$ °C, suggesting that Sb in Meso-ATO is unstable at high annealing temperature.

Table 6. Ir loadings (wt. %), bulk composition (molar ratios) derived from ICP-OES and surface composition (molar ratios) derived from XPS (photoelectron kinetic energy: 550 eV) of PA-IrNi_x/Meso-ATO-T annealed at different temperatures and IrNiO_x/Meso-ATO-180 prepared from PA-IrNi_x/Meso-ATO-180.

Samples	Ir loading	Ni/Ir		Ir/ (Sn+Sb)	O/ (Sb+Sn)	Sb/Sn
	ICP-OES	ICP-OES	XPS	XPS	XPS	XPS
Meso-ATO		-	-	-	1.8	0.14
IrNi _x /Meso-ATO-180	19.3	3.3	4.5	0.11	1.8	0.12
IrNi _x /Meso-ATO-250	17.5	3.4	5.0	0.12	1.8	0.14
IrNi _x /Meso-ATO-300	16.0	3.8	11.0	0.04	1.7	0.1
IrNi _x /Meso-ATO-400	16.7	3.6	16.6	0.035	1.7	0.09
IrNi _x /Meso-ATO-500	15.5	3.7	9.4	0.03	1.8	0.1
IrNiO _x /Meso-ATO-180	-	-	1.5	0.1	1.9	0.08

Atomic PDF patterns extracted from the HE-XRD data are shown in **Figure 37**. The first atomic coordination shell (2.61 Å) of the PA-IrNi_{3.3}/Meso-ATO-180 is consistent with a substitutional solid solution (random) alloy of Ir and Ni atoms falling in-between the metal-metal distances of pure Ni (~2.49 Å) and pure Ir (~2.71 Å). The increasing first shell radial distance with increasing annealing temperature confirmed Ir bulk segregation, in agreement with powder XRD and XPS results. Signatures of a cubic NiO nanophase appeared at 300 °C (vertical green broken lines in **Figure 37a**) developing into a prominent co-existing NiO nanophase at $T = 500$ °C (green solid

line in **Figure 37a** represents a fit of NiO nanophase). Remnants of metallic nanoparticles have a first coordination sphere positioned at 2.72 Å which is very close to the metal-metal distances of pure Ir.

Experimental and model atomic PDFs for the various IrNi_x/Meso-ATO-T samples are presented in **Figure 37b**.

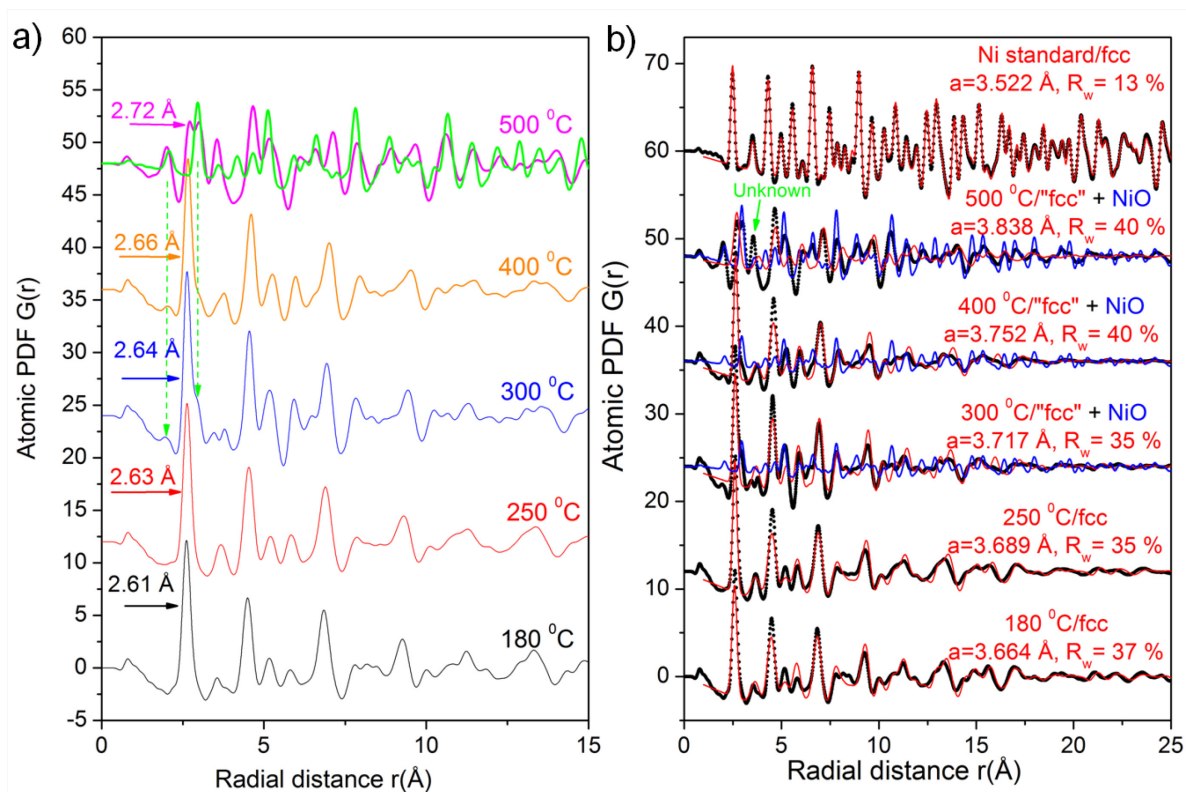


Figure 37. Atomic pair distribution functions (PDFs) of supported IrNi_x precursor alloys annealed at different temperatures T (T is given by each data set). a) Experimental atomic PDFs. Radius of first atomic coordination sphere in nanoparticles is given by each data set. Signatures of NiO nanophase appear with samples treated at 300 °C and above (green vertical broken arrows), and the NiO nanophase fully developed in the sample annealed at 500 °C (solid green line represents a fit of NiO nanophase). b) Experimental (symbols) and model (solid lines) atomic PDFs for IrNi_x/Meso-ATO-T. Models feature fcc-type (line in red) metallic alloy and NiO nanophase (line in blue). Refined “fcc-lattice parameters” are given by each data set (in red). Respective fcc model agreement/fit quality factors (R_w) are also given (in %). Reprinted from Ref. 106 with permission of John Wiley and Sons, copyright (2015).

Models feature fcc-type (red line) metallic alloy and NiO nanophase (blue line). Nanoparticles treated at 180 °C and 250 °C are metallic nanoalloys of fcc-type structure, though the fcc structure is somewhat “distorted”. Nanoparticles treated at 500 °C are completely phase segregated into a metallic Ir and NiO phase. Missing

signatures of bulk IrO₂ suggested that IrO_x observed in XPS existed only at near-surface. Based on our understanding of the thermal behavior of the IrNi_x/Meso-ATO-T precursors, we hypothesized that annealing at 180 °C (IrNi_{3.3}/Meso-ATO-180 material) would be most amenable to the generation of the core-shell oxide architecture.

5.2. Structure confirmation of IrNiO_x core-shell nanoparticles

According to the study of IrNiO_x nanoparticles supported on carbon (see section 4.5),⁹⁶ directly oxidized IrNiO_x core-shell nanoparticles showed a higher OER activity than stepwise oxidized nanoparticles. Furthermore, the electrochemical pretreatment strongly affected the electrochemical properties of ATO-supported IrNi_x nanoparticles, as will be discussed in the chapter 6, therefore, we utilized a high potential-direct electrochemical oxidation protocol for our IrNi_x/Meso-ATO-T catalysts (see section 2.3.3 for more details). The oxidized IrNi@IrO_x core-shell catalysts are denoted as “IrNiO_x/Meso-ATO-T”.

To understand the changes in the surface chemical state of Ir during the formation of the active IrNiO_x/Meso-ATO-180 core-shell catalyst, depth-resolved XPS was applied and the data are shown in **Figure 38**. Upon cycling into the OER potential region, the largely metallic precursor alloy (**Figure 38a**) gradually depleted in Ni and transformed into a thin IrO_x shell (**Figure 38b**). The oxide shell is however much thinner compared to IrNiO_x on carbon. Nevertheless, extended OER operation is going to thicken the oxidized surface shell. The 210 eV kinetic energy data evidenced a higher binding energy species, the assignment of which is however not unambiguous. It might be related to a final state shift due to size or strain effects but it can also signal the formation of a higher-valent (> 4+) Ir state at the top surface layer, as reported recently.¹⁰⁹ The surface composition of IrNiO_x/Meso-ATO-180 derived from XPS at KE 550 eV (**Table 6**) shows that Ni was selectively removed from the surface of the nanoparticles. The Ni/Ir ratio decreases from 4.5 in PA-IrNi_x/Meso-ATO-180 to 1.5 in IrNiO_x/Meso-ATO-180 while the Ir/(Sn+Sb) ratio remains constant. The O/(Sn+Sb) ratio increases only slightly since Ni oxide-hydroxide was removed from the surface and Ir was only oxidized by a few layers on the surface. The Sb/Sn ratio decreases, indicating that Sb is not very stable in the ATO network. This might cause a partial loss of electric conductivity of the support during electrocatalysis.

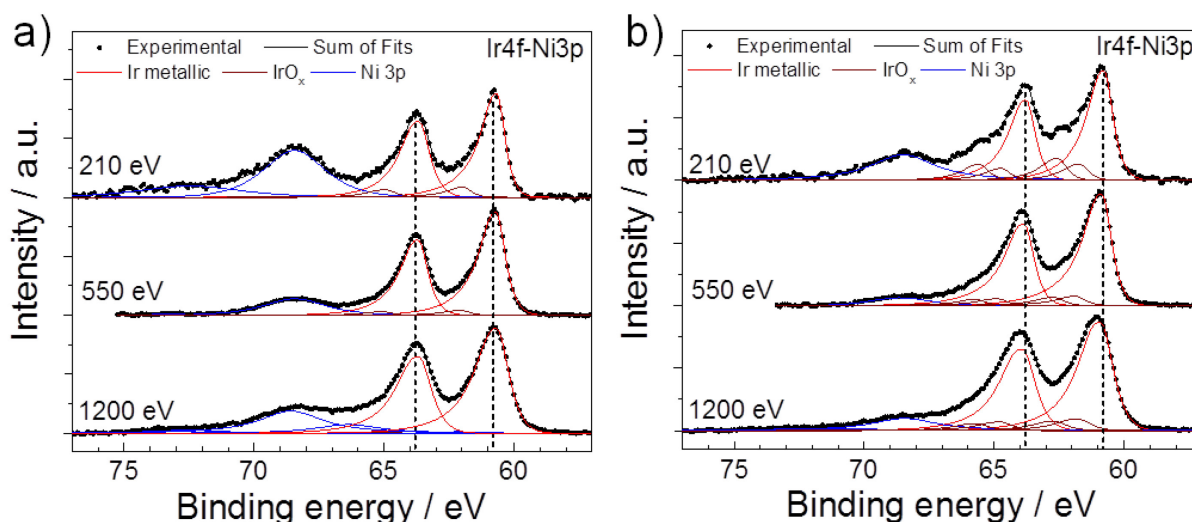


Figure 38. Depth-resolved Ir 4f-Ni 3p XP spectra of a) PA-IrNi_{3.3}/Meso-ATO-180 and b) the corresponding IrNiO_x/Meso-ATO-180 OER catalyst after dealloying and oxidation (50 CV cycles, 0.05 - 1.5V). Top to bottom spectra were measured at photoelectron kinetic energies of 210, 550, and 1200 eV. The dash vertical lines indicate peak position of metallic Ir. Note, the broader spectra at higher photon energy are due to the lower resolution of the beamline. Reprinted from Ref. 106 with permission of John Wiley and Sons, copyright (2015).

The HRTEM image of the IrNi_x/Meso-ATO-180 precursor alloy (**Figure 39a**) demonstrates that the Meso-ATO support and IrNi_x are connected. The bottom inset fast Fourier transform (FFT) shows the well-defined diffraction pattern of ATO and the top one shows the high defective single crystalline diffraction pattern of the [110]-fcc IrNi_x. One can see that the IrNi_x FFT consists of split reflections, which basically transform to stripes, indicating the high concentration of defects in the IrNi alloy phase.

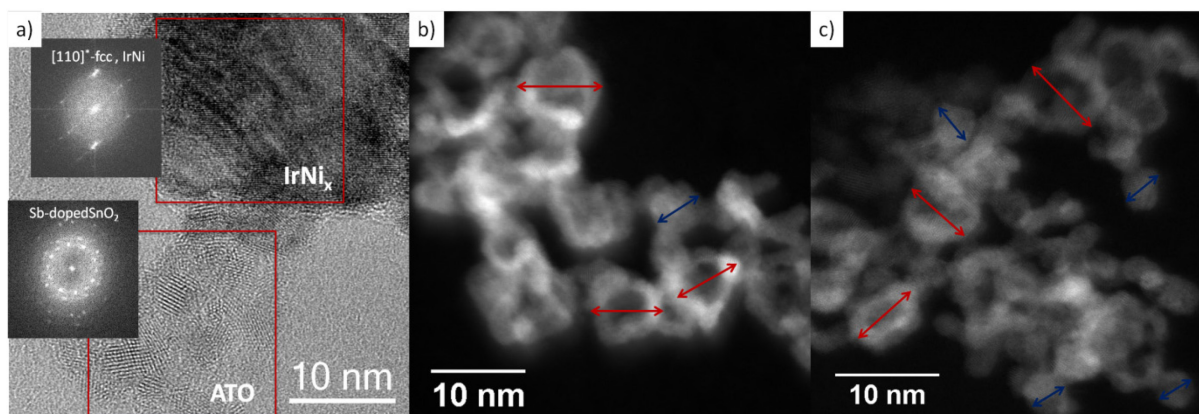


Figure 39. a) HRTEM image of IrNi_{3.3}/Meso-ATO-180 with FFTs (insets) of IrNi_x and Meso-ATO, b) and c) HAADF-STEM images of hollow core-shell (red arrows) and solid core-shell (blue arrows) IrNiO_x/Meso-ATO-180 nanoparticles. Reprinted from Ref. 106 with permission of John Wiley and Sons, copyright (2015).

A HAADF-STEM image and the corresponding elemental mapping of IrNiO_x/Meso-ATO-180 are presented in **Figure 40**. In aberration-corrected HAADF-STEM Z-contrast image of the IrNiO_x/Meso-ATO-180 (**Figure 40a**), the dealloyed oxidized nanoparticles exhibit dark centers with bright outer shells. Under Z-contrast condition, the image intensity of Ir (Z = 77) is much higher than that of Ni (Z = 28). The spherical morphologies of the nanoparticles rule out thickness variations as source of the dark particle Z-contrast suggesting a dramatically Ir-depleted chemical state of the particle cores surrounded by Ir-rich shells.

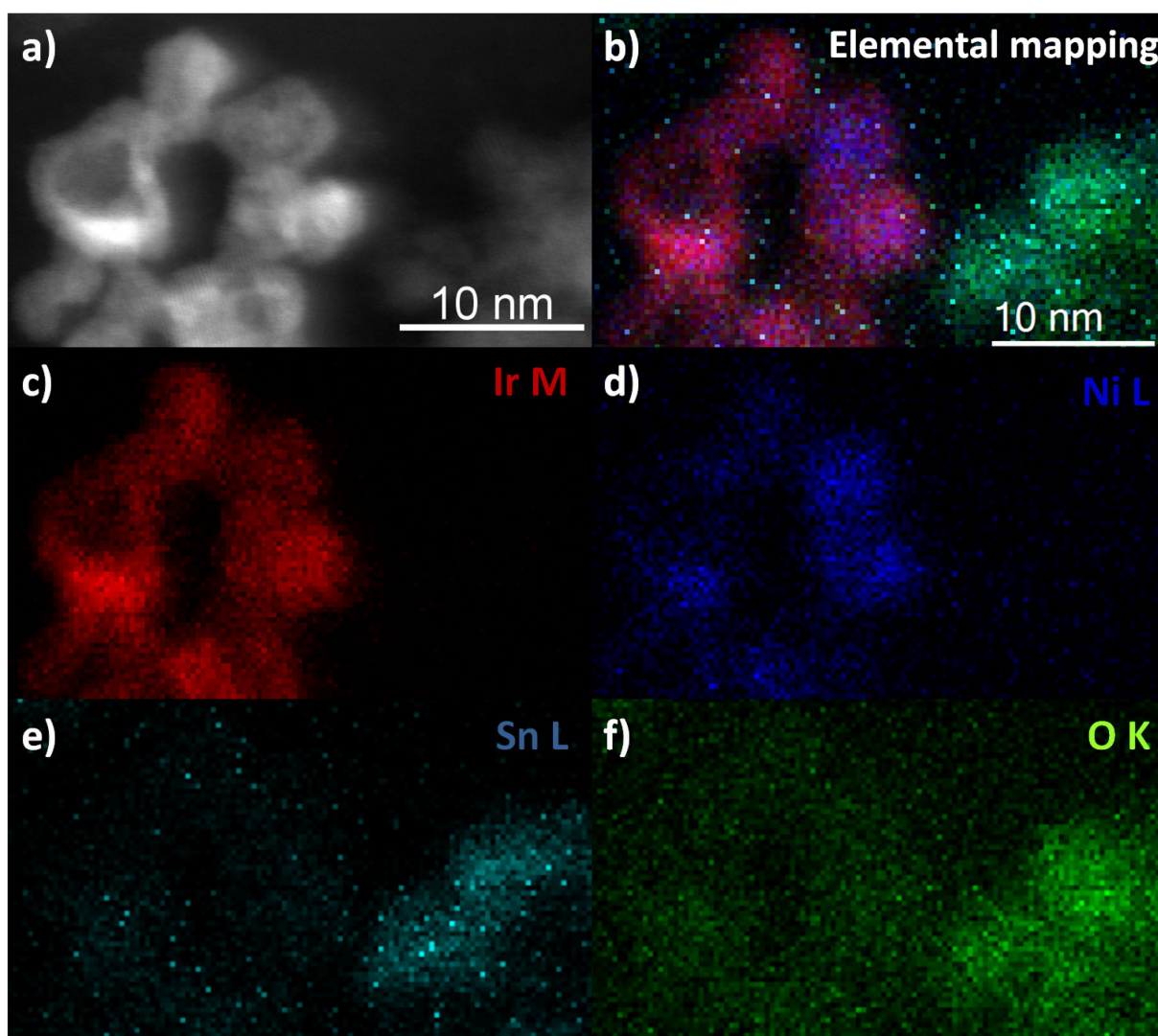


Figure 40. a) HAADF-STEM image of the IrNiO_x/Meso-ATO-180 core-shell nanoparticle catalyst synthesized from Meso-ATO supported IrNi_{3.3} nanoparticle precursor alloy annealed at 180 °C (PA-IrNi_{3.3}/Meso-ATO-180), b) corresponding elemental mapping. c) d) c, e) f) corresponding elemental mappings of Ir, Ni, Sn, and O, respectively. Reprinted from Ref. 106 with permission of John Wiley and Sons, copyright (2015).

The elemental mapping (**Figure 40b**, c, d, e, f) shows clearly enrichment of Ir on the particle surface (shells), confirming the structural core-shell hypothesis. The Ni concentration in the cores remains high for small particles while big particles tend to form hollow structures with Ir-rich shells.

HAADF STEM images of IrNiO_x/Meso-ATO-180 (**Figure 39b**, c) were used to estimate the size distribution of the core-shell particles. Due to the anisotropic shape of the nanoparticles, the measured size distribution is affected by the orientation of the particles. Nevertheless, the size distribution of the larger hollow particles is quite narrow and in the range of 7 to 11 nm (red arrows). For the small Ni rich particles, the sizes are below 4.5 nm (see blue arrows). In fact, the size of the hollow and solid core-shell nanoparticles did not change during electrochemical treatment. Analysis of an ensemble of core-shell particles revealed that the core-shell morphology depended on particle size, which was also observed for IrNi_x/C.⁹⁶

In order to explain the formation of hollow particles during electrochemical dealloying, we recall that the surface diffusion rate of the more noble metal must be slower than the surface dissolution rate of the less noble metal to allow continuous dealloying deep into the bulk which leads to nanoporosity.¹¹⁰ The nanoporosity formation therefore depends on particle size,¹¹¹ composition of the alloy,¹¹² dealloying conditions such as electrolyte and the applied potential.^{112, 113} In the current study, the IrNi_x precursor alloys were dealloyed and oxidized by cycling the potential from 0.05V to 1.5V vs. RHE in N₂ saturated 0.05M H₂SO₄, at which the dissolution rate of Ni was very high, therefore, the critical particle size to form hollow core-shell structure was small. Another possible explanation for the structure evolution is the atomic structure of the IrNi_x precursor alloys. Since the Ni precursor was heated to reaction temperature first and the Ir precursor was added afterwards, a number of seeds of Ni might have already formed, and these would result in the bigger particles with Ni-rich cores. HRTEM suggested that the bigger particles are relatively irregular with many defects and multiplet structures. Once a part of Ni has already precipitated, compositionally more uniform smaller IrNi_x nanoparticles were formed. These two types of nanoparticles dealloy differently, resulting in different final morphologies.

Figure 41 illustrates conceptually the structure hypothesis regarding the active catalyst/support couple, with the OER proceeding at thin IrO_x shells on Ir-low/Ir-free cores, thereby reducing the required Ir amount significantly.

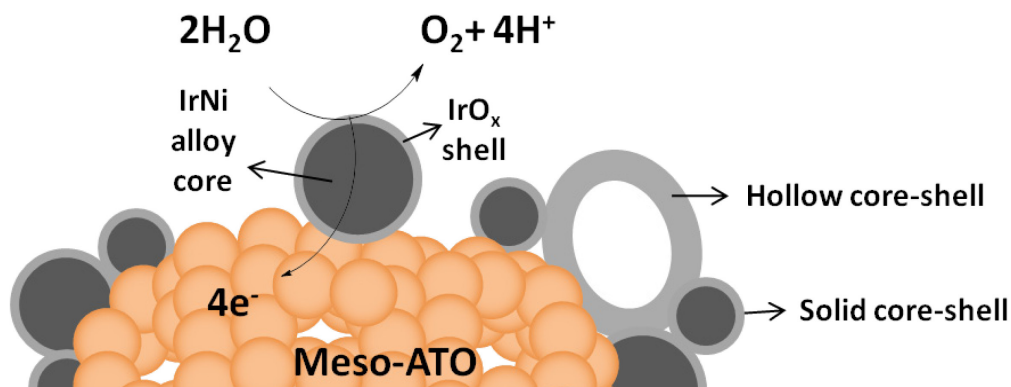


Figure 41. Scheme of the oxygen evolution reaction on the IrO_x shell of IrNiO_x core-shell nanoparticles supported on Meso-ATO. Reprinted from Ref. 106 with permission of John Wiley and Sons, copyright (2015).

5.3. Electrochemical catalytic activity and stability for the oxygen evolution reaction of core-shell IrNiO_x/Meso-ATO

We utilized the high potential direct oxidation with 1 cycle of CV from 1.0 to 1.8V and 50 cycles of CVs from 0.05 V to 1.5 V (see section 2.3.3) to generate alloy core - oxide shell nanoparticles from the IrNi_x/Meso-ATO-T precursor alloys. Electrochemically oxidized Ir nanoparticles (Ir/C and Ir/com.-ATO) were used as activity and stability reference. The oxidized IrNi@IrO_x core-shell catalysts and benchmarks were denoted as “IrNiO_x/Meso-ATO-T”, “IrO_x/C”, and “IrO_x/com.-ATO”, respectively.

The redox peaks at around 0.8V vs RHE in the CVs correspond to the Ir^{III/IV} redox peaks of IrO_x and thus are characteristics for electrochemical active surface area (ECSA) or active sites of electrochemical oxidized IrO_x. **Figure 42a** shows CVs from 0.4 V to 1.4 V vs. RHE at a scan rate of 20 mV s⁻¹ for all IrNiO_x/Meso-ATO-T samples. Obviously, an increasing annealing temperature in the synthesis process of the precursor alloys leads to a decreasing number of active sites of the corresponding core-shell nanoparticles. The decrease in number of active sites might be a result of NiO segregation from the alloyed phase or/and lower electronic conductivity of the support due to a decreased Sb/Sn ratio at high annealing temperature.

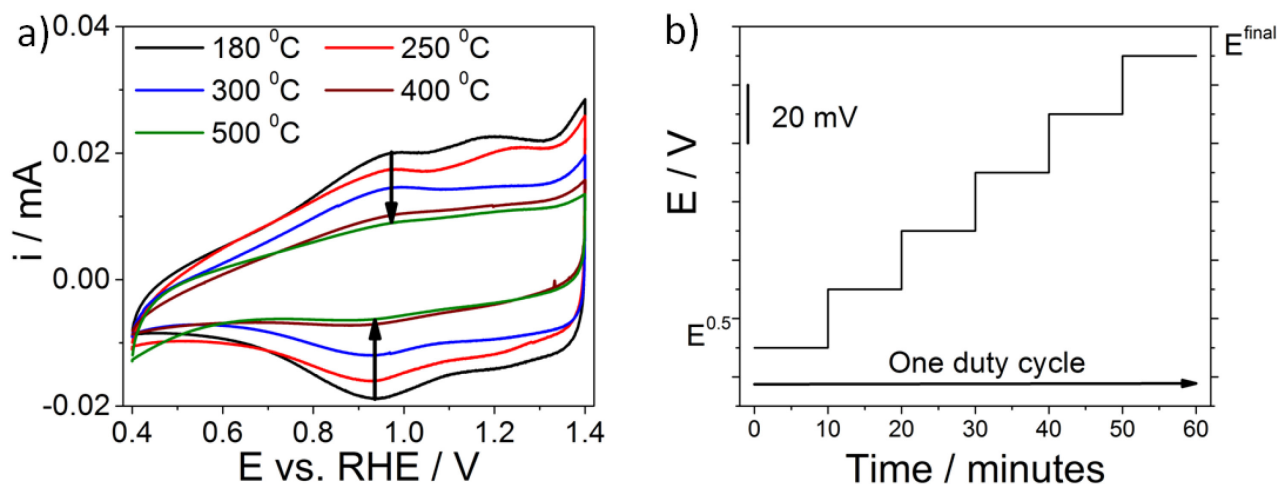


Figure 42. a) Cyclic voltammogram of IrNiO_x/Meso-ATO-T annealed at different temperatures, ($T = 180, 250, 300, 400, 500 \text{ } ^\circ\text{C}$), and b) one duty cycle of the durability test under stepwise load increase. Reprinted from Ref. 106 with permission of John Wiley and Sons, copyright (2015).

In order to correlate the catalyst structure with its catalytic OER activity under approximate conditions of PEM electrolyzers, the catalysts were subjected to a cyclic voltammetry protocol in highly acidic electrolyte (see section 2.3.3 for more details). The linear sweep voltammetry of all catalysts along with their Ir-mass based reactivity at an overpotential $\eta=280 \text{ mV}$ are presented in **Figure 43**.

Clearly, the IrNiO_x/Meso-ATO-T catalysts with $T \leq 300 \text{ } ^\circ\text{C}$ are significantly more OER active on both geometric surface and Ir-mass basis compared to the IrO_x/C and IrO_x/com.-ATO benchmarks. For these materials, the Ni content in the particle core remained high. It is plausible that, as a result of this, electronic and/or strain effects modified the chemisorption and reactivity of intermediates at the surface. In contrast, the catalysts annealed at $400 \text{ } ^\circ\text{C}$ and $500 \text{ } ^\circ\text{C}$ showed significantly lower OER activities due to the phase segregation into a NiO and an Ir-rich nanophase. The lower Ni content of the latter phase translates in a reactivity approaching that of pure Ir. In addition, the characteristic Ir^{III/IV} redox couple is usually used to estimate the molar amount of catalytically active Ir atoms of Ir catalysts.⁹⁶ The Ir^{III/IV} wave is decreased with increasing annealing temperature, indicating a smaller number of accessible Ir^{III/IV} active sites (**Figure 42a**). Together, these effects reduce the apparent OER activity of IrNiO_x/Meso-ATO annealed at $400 \text{ } ^\circ\text{C}$ and $500 \text{ } ^\circ\text{C}$.

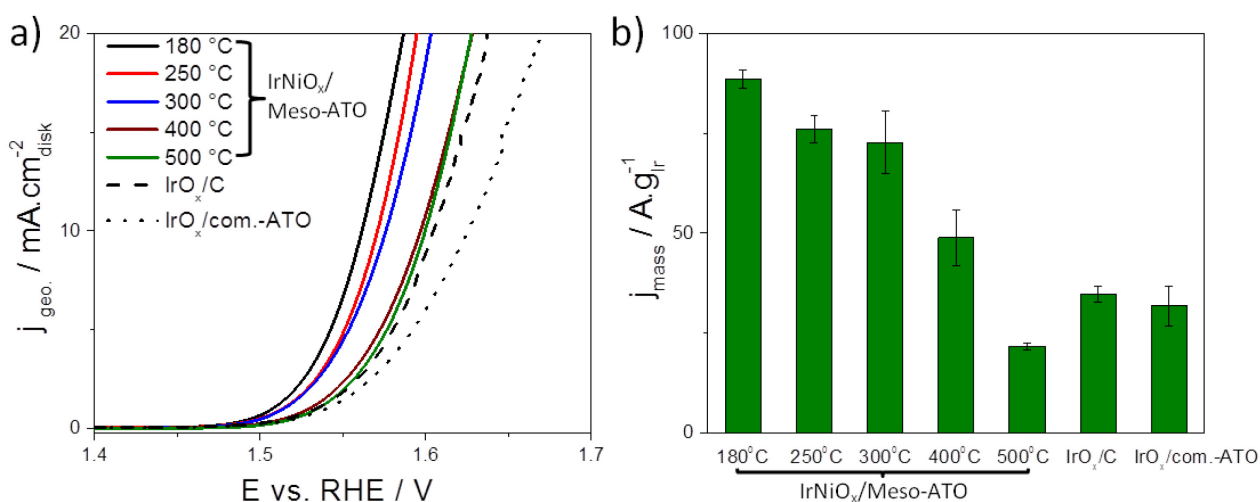


Figure 43. a) Electrocatalytic oxygen evolution reaction (OER) activities of IrNiO_x core-shell nanoparticles supported on mesoporous ATO (IrNiO_x/Meso-ATO-T), pure Ir supported on carbon (IrO_x/C), and on commercial ATO (IrO_x/com.-ATO) measured using linear sweep voltammetry, b) Ir-mass based activity at $\eta = 280 \text{ mV}$ overpotential of IrO_x/C, IrO_x/com.-ATO, and IrNiO_x/Meso-ATO-T. The temperature at which nanoparticles have been treated is given for each data set. Measurement conditions: 25 °C, 0.05M H₂SO₄, 1600 rpm. The loading of Ir was 10.2 $\mu\text{g cm}^{-2}$. Reprinted from Ref. 106 with permission of John Wiley and Sons, copyright (2015).

The most active catalyst was the IrNiO_x/Meso-ATO-180 material, which showed a 2.5 times higher Ir-mass based activity compared to IrO_x/C and IrO_x/com.-ATO at $\eta = 280 \text{ mV}$. This implies a 2.5x times higher electrolyzer hydrogen output at the constant voltage.

The electrochemical stability of the core-shell IrNiO_x/Meso-ATO-180 catalyst was tested together with the reference materials under constant current load conditions (chronopotentiometry) for a period of 20 hours (**Figure 44a**). The measured electrode potential increased gradually for the IrO_x/C and IrO_x/com.-ATO, indicating their performance degradation. Then, the electrode potential rose sharply to 2.0 V after 9 and 12 hours for IrO_x/C and IrO_x/com.-ATO, respectively, evidencing a severe degradation of the support associated with a loss of the active catalyst particles. In contrast, the electrode potential of IrNiO_x/Meso-ATO-180 remained essentially constant throughout the 20 hour stability test, evidencing a previously unachieved performance durability of low Ir content core-shell particles.

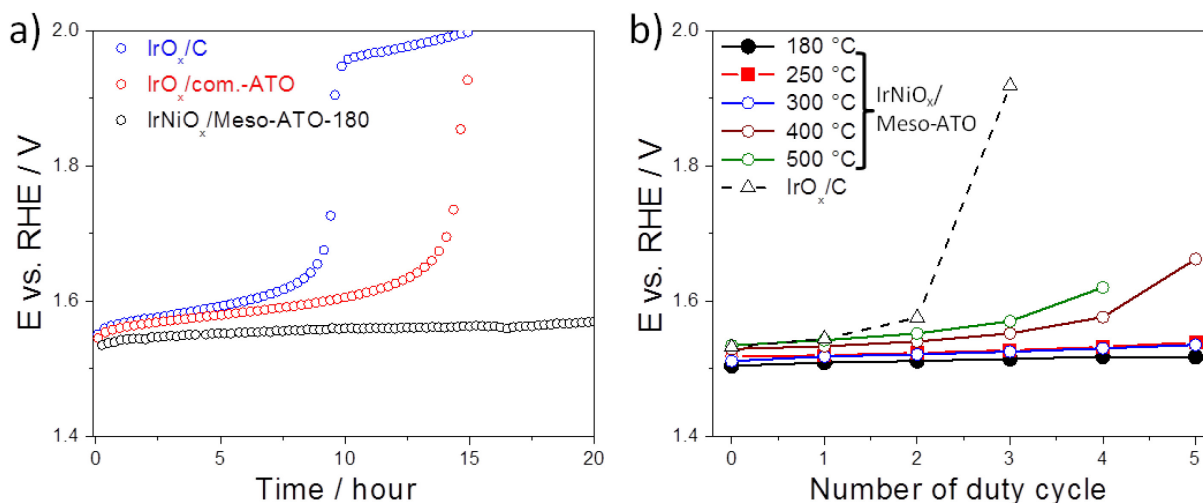


Figure 44. Electrocatalytic OER stability of IrNiO_x core-shell nanoparticles supported on mesoporous ATO (IrNiO_x/Meso-ATO-T), pure Ir supported on carbon (IrO_x/C), and on commercial ATO (IrO_x/com.-ATO) a) Constant current chronopotentiometric stability measurements at a current density of 1 mA cm⁻², and b) Potential at 1 mA cm⁻² using linear sweep voltammetry after duty cycles of IrO_x/C and IrNiO_x/Meso-ATO-T. Temperature at which nanoparticles have been treated is given for each data set. Measurement conditions: 25 °C, 0.05M H₂SO₄, 1600 rpm. The loading of Ir was 10.2 μg cm⁻². Reprinted from Ref. 106 with permission of John Wiley and Sons, copyright (2015).

In order to test the durability of the catalysts under conditions closer to the operating conditions of PEM electrolyzers, we applied a more severe potential-step duty-cycle protocol (**Figure 42b**) (see section 2.3.3). **Figure 44b** plots the electrode potentials at a current density of 1 mA cm⁻² measured using linear sweep voltammetry after each duty cycle was applied. The electrode potential of IrO_x/C reached > 1.9 V after only 2 duty cycles, indicating the complete degradation of the catalyst. Note that the same catalyst IrO_x/C was completely degraded after 9 hours in the chronopotentiometry test, showing that testing condition in the stair-case duty cycle protocol was harsher. The IrNiO_x/Meso-ATO-500 and IrNiO_x/Meso-ATO-400 were degraded after 4 and 5 duty cycles, respectively. Interestingly, the IrNiO_x/Meso-ATO-500 was more stable than IrO_x/C although it was less active in the first OER test, benefited from high corrosive stable Meso-ATO. As before, IrNiO_x/Meso-ATO annealed at lower T showed higher activity as well as durability than Ir core-shell catalysts annealed at high T (400 and 500 °C). Again, the most active and stable catalyst was the IrNiO_x/Meso-ATO-180 material evidencing a successful combination of the activity advantages of core-shell architectures and the durability benefits of an oxide support.

5.4. Summary

We have presented a novel catalyst/support couple concept, involving an electrochemically dealloyed IrNi core-IrO_x shell concept combined with a mesoporous corrosion-resistant oxide support for highly efficient and stable OER catalysts in acidic medium. This concept builds upon the formation of an oxidized Ir shell that provided excellent OER activity at low noble metal content and the high surface area mesoporous structure of the support enabled the dispersion of the active nanoparticles, as well as provided high corrosive resistance for the catalysts.

The structure evolution of precursor alloys under the thermal treatment at various temperatures T was comprehensively investigated. Ni surface enrichment was observed with increasing annealing temperature. Further studies showed that a NiO nano phase segregated from the IrNi nanoalloy phase at $T \geq 300$ °C and developed to completely separated NiO cubic phase at $T = 500$ °C. Correlating the synthesis-structure characteristic with the OER activity we concluded that NiO phase segregation shows a detrimental effect on the OER activity and stability of the corresponding core-shell nanoparticles.

The most amenable precursor alloy to prepare core-shell nanoparticle catalyst is PA-IrNi_x/Meso-ATO-180, the corresponding IrNiO_x/Meso-ATO-180 core-shell water splitting catalyst supported a 2.5 times higher oxygen on the electrolyzer level, while showing negligible degradation during a 20 hour stability test unlike various Ir benchmark materials. The nanostructured core-shell catalyst/mesoporous support couples could serve as suitable coatings in realistic PEM electrolyzer anodes. Beyond their practical deployment, the presented core-shell catalyst/oxide support concept represents a quite general strategy to reduce the amount of scarce elements in catalytic nanoparticles, and could be transferred to other precious metal based oxides in the future.

*This page
intentionally
left blank*

6. Impact of the Support Materials on OER Activity and Structure Evolution of IrNiO_x Core-Shell Nanoparticles

In the previous chapters 4 and 5, the influences of the active phase (IrNi core-shell nanoparticles), in particular, the Ni content in the precursor alloys, the electrochemical properties, the Ni segregation, on the OER activity were investigated. The Ni content in the precursor alloys and the Ni segregation from the alloyed phase strongly affected the OER activity of the catalysts. Beside the active phase, the support material plays an important role for the activity and stability of the supported catalysts. In this chapter, the structure evolution of IrNiO_x core-shell nanoparticles supported on carbon and mesoporous antimony doped tin oxide (ATO) is studied under electrochemical dealloying, oxidation and OER conditions using high energy X-ray diffraction (HE-XRD) coupled with atomic pair distribution functions (PDFs) and X-ray photoelectron spectroscopy (XPS). Special attention was paid to support materials, which showed strong effects on the formation of core-shell structure, the dealloying process of Ni, and the oxidation process of Ir shells. All these effects were correlated to OER activity and stability.

6.1. Structure evolution during electrochemical dealloying and oxidation

The precursor alloys, IrNi_x nanoparticles supported on carbon and ATO (denoted as PA-IrNi_x/C and PA-IrNi_x/ATO, respectively), were synthesized using the polyol method with optimized conditions for each support material (see section 2.1.4 for details). The initial Ir : Ni ratio in the precursor alloys was chosen as 1 : 3, since this ratio showed the best OER activity for the corresponding core-shell nanoparticles supported on carbon as discussed in chapter 4. The actual Ir : Ni ratios were 1 : 3.3 and 1 : 3.1 for PA-IrNi_x/C and PA-IrNi_x/ATO, respectively, as determined by ICP-OES. The PA-IrNi_x/C and PA-IrNi_x/ATO were dealloyed and/or oxidized using electrochemical dealloying, stepwise oxidation, and directly oxidation protocols (see section 2.3.3). The electrochemically treated samples are then denoted as D-IrNi_x/C (or D-IrNi_x/ATO), SO-IrNiO_x/C (or SO-IrNiO_x/ATO), and DO-IrNiO_x/C (or DO-IrNiO_x/ATO), respectively.

HE-XRD patterns and experimental and model atomic PDFs of IrNi_x and IrNiO_x nanoparticles supported on carbon and ATO are shown in **Figure 45** and **Figure 46**, respectively. The patterns were corrected for support scattering and thus directly reflect the atomic structure of the IrNi_x and IrNiO_x nanoparticles.

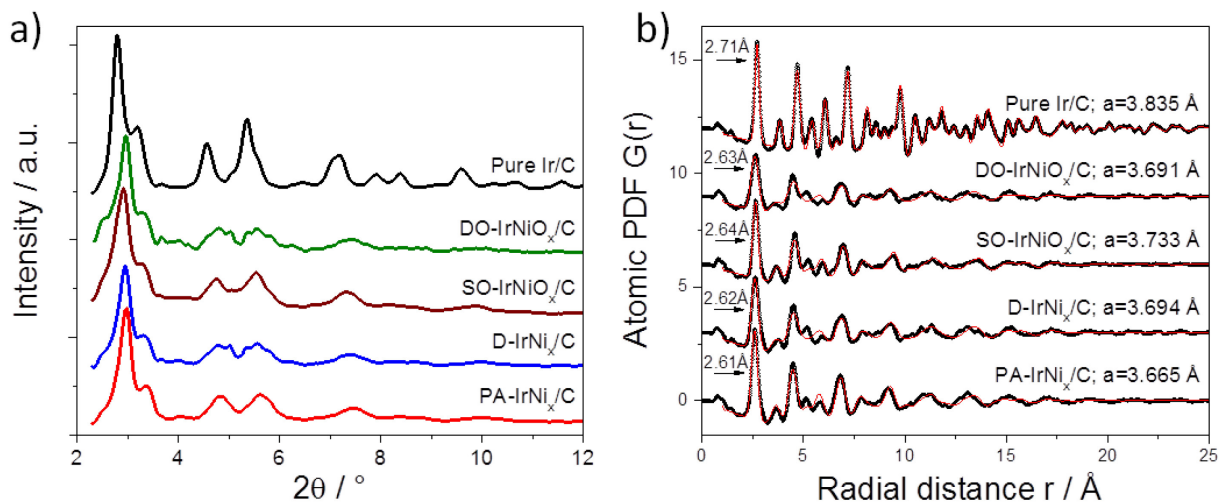


Figure 45. a) High energy X-ray diffraction patterns, and b) the corresponding experimental (black symbols) and model (red lines) atomic pair distribution functions (PDFs) for IrNi_x and IrNiO_x nanoparticles supported on carbon. Radius of first atomic coordination sphere in nanoparticles and refined “lattice parameters” are given by each data set. The pure Ir, precursor alloy, dealloyed, stepwise oxidized, and directly oxidized samples are denoted as pure Ir/C, PA- IrNi_x /C, D- IrNi_x /C, SO- IrNiO_x /C, and DO- IrNiO_x /C, respectively.

In general, atomic PDF models for IrNi_x and IrNiO_x nanoparticles supported on carbon and ATO feature fcc-type metallic alloys. The atomic arrangement in all samples is very much fcc-like. Oxidation and Ni dealloying did not lead to extra PDF feature, indicating that the nanoparticles were not “excessively” oxidized/dealloyed and did not change their crystal structure. However, oxidation/dealloying significantly affected the atomic structure of the nanoparticles as reflected by the significantly different values of the respective “lattice parameters” (a). Here the term “lattice parameters” are used to underline that atoms in nanoparticles do not sit on vertices of infinitely 3D periodic lattices. So the “lattice parameters” of the nanoparticles are approximations which need to be used with care. Lattice parameters of all Ni-containing IrNi nanoparticles were smaller than that of pure Ir, indicating the lattice contraction due to alloying of Ir with smaller Ni atoms. The first atomic coordination shells of Ni-containing samples fell in-between the metal-metal distances of pure Ni (~ 2.49 Å) and pure Ir (~ 2.71 Å), consistent with a substitutional solid solution alloy of Ir and Ni atoms.

Comparing the carbon supported samples (**Figure 45**), PA-IrNi_x/C showed the smallest lattice parameter because of the highest Ni content in the precursor alloy state. The lattice parameter of D-IrNi_x/C increased due to removal of Ni from the IrNi_x nanoparticles during electrochemical dealloying. Thereby, the lattice parameter increased only slightly, suggesting Ni remains to a largely extent in the IrNi alloy nanoparticles. The lattice parameter of DO-IrNiO_x/C was again quite similar to that of D-IrNi_x/C, suggesting that after the directly electrochemical oxidation step a large amount of Ni remained in the alloy nanoparticles. In case of SO-IrNiO_x/C the lattice parameter was substantially larger than those of D-IrNi_x/C and DO-IrNiO_x/C, since SO-IrNiO_x/C first underwent a dealloying and then an oxidation step which resulted in a larger extent of Ni dissolution.

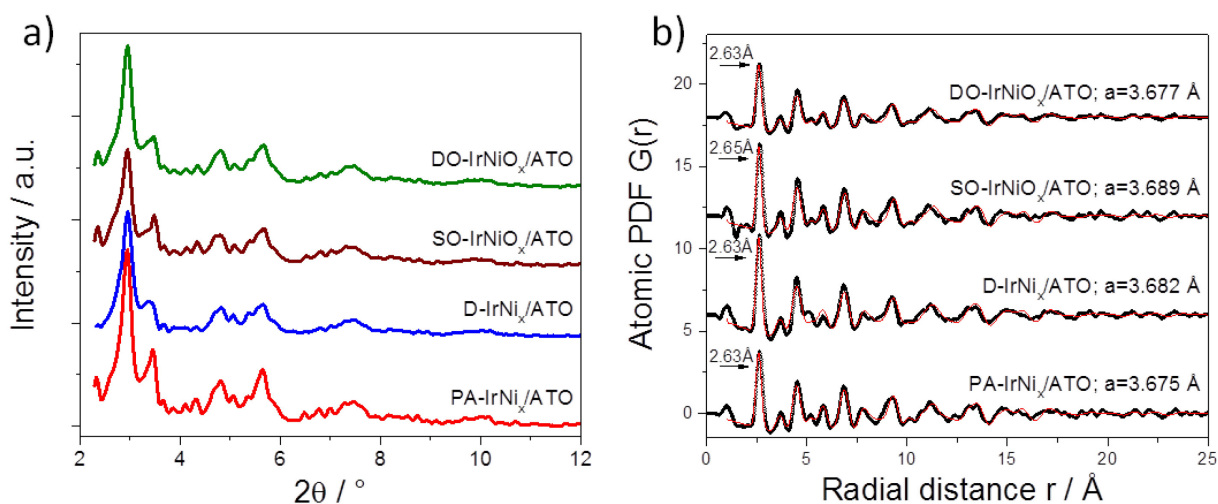


Figure 46. a) High energy X-ray diffraction patterns, and b) corresponding experimental (black symbols) and model (red lines) atomic PDFs for IrNi_x and IrNiO_x nanoparticles supported on ATO. Radius of first atomic coordination sphere in nanoparticles and refined “lattice parameters” are given by each data set. The precursor alloy, dealloyed, stepwise oxidized, and directly oxidized samples are denoted as PA-IrNi_x/ATO, D-IrNi_x/ATO, SO-IrNiO_x/ATO, and DO-IrNiO_x/ATO, respectively.

There is a clear difference in the degree of Ni dealloying between carbon and ATO supported samples. The “lattice parameters” of electrochemically treated ATO supported samples (**Figure 46**) increased only slightly compared to that of PA-IrNi_x/ATO, whereas in case of carbon supported samples, the electrochemical treatment lead to more drastical increases in “lattice parameters”. This suggests that more Ni was leached out from carbon supported than from the ATO supported samples. Indeed, quantitative XPS results of SO-IrNi_x/C, DO-IrNi_x/C (see chapter 4) and IrNiO_x/Meso-ATO (see chapter 5) testified that after oxidation, more Ni was

removed from the surface of nanoparticles supported on carbon. The Ni/Ir ratios after oxidation were 0.09, 0.14 for SO-IrNi_{3.3}/C and DO-IrNi_{3.3}/C, respectively, while the Ni/Ir ratio was 1.5 for IrNiO_x/Meso-ATO (high potential directly oxidized with 50 cycles of oxidation, see section 2.3.3).

As shown in chapter 4 and 5 for the carbon supported and the ATO supported samples, core-shell nanoparticles were formed after the electrochemical treatment, consisting of IrNi metallic or hollow cores with shells rich of metallic Ir (after the electrochemical dealloying) or IrO_x (after the electrochemical oxidation). It is well known that alloying larger Ir atoms with smaller Ni atoms causes lattice contraction. Beside, hollow cores can also induce the lattice contraction.¹¹⁴ In fact, the lattice parameters of SO-IrNiO_x/C and DO-IrNiO_x/C decreased compared to the corresponding precursor alloy, but were still much smaller than that of pure Ir. This indicates that the lattice contraction remained quite high after electrochemical treatments. For electrochemically treated ATO supported nanoparticles, the lattice parameters almost unchanged, showing that the lattice contraction remained higher than for electrochemically treated carbon supported samples. The differences in lattice contraction might affect the OER activity of the core-shell nanoparticles.

To explain the different Ni dealloying behavior of IrNi_x alloy nanoparticles supported on carbon and ATO, their cyclic voltammograms (CVs) were compared (**Figure 47** and **Figure 48**). Dealloying CVs of IrNi_x/C (**Figure 47a**) showed clearly hydrogen underpotential deposition (H_{upd}) peaks in the region of 0.05 to 0.4 V vs. RHE, characteristic for metallic Ir surfaces.^{115,96} The CVs of IrNi_x/C changed only slightly during the electrochemical dealloying, the H_{upd} shifted to lower potential and the capacitive current decreased because the contribution of the Ni dissolution to the capacitive current decreased with increasing the number of scans. After 200 cycles, the capacitive current became stable and the shape of the CV resembled that of a pure Ir CV, suggesting that the dissolution of surface Ni atoms has yielded a stable metallic IrNi@Ir core-shell structure. In contrast, the dealloying CVs of IrNi_x/ATO (**Figure 47b**) showed tiny H_{upd} waves and large reduction peaks at ~ 0.4V in the cathodic scans, corresponding to the reduction of tin oxide.¹¹⁶ The reduction and the corresponding oxidation peaks decrease with increasing number of cycles indicating that the amount of electrochemically addressable ATO decreases due to an

irreversible process, probably due to the irreversible reduction of tin oxide, or the dissolution of tin during the potential sweeps.

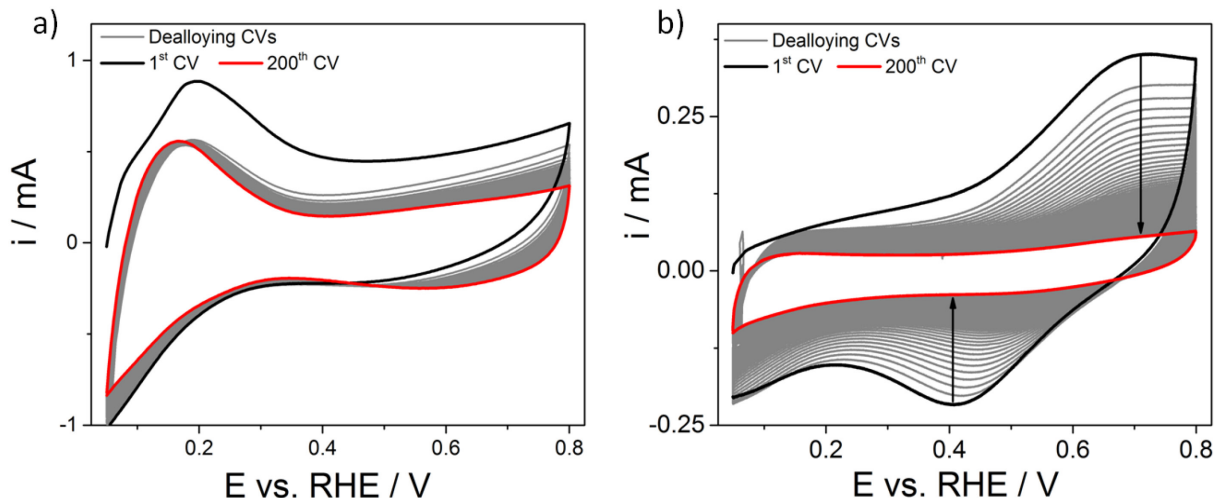


Figure 47. Dealloying cyclic voltammograms of a) IrNi_x supported on carbon (IrNi_x/C) and b) IrNi_x supported on ATO (IrNi_x/ATO) from 0.05 to 0.8 V vs. RHE in 0.05 M H₂SO₄, 200 cycles, scan rate 500 mV s⁻¹. The 1st and the 200th CVs are shown to clarify the direction of change during dealloying. Black arrows indicate the irreversible transformation process of ATO.

The cyclic voltammograms recorded during stepwise and direct oxidation of IrNiO_x/C and IrNiO_x/ATO samples are presented in **Figure 48**. The 1st and the last oxidation CVs are highlighted to clarify the direction of change. The 1st CV of DO-IrNiO_x/C showed quite high currents in the anodic scan compared to that of SO-IrNiO_x/C, probably due to an elevated dissolution of Ni from surface. After the 1st CV, the CV shape of SO-IrNiO_x/C and DO-IrNiO_x/C were similar. During the oxidation step, H_{upd} peaks in the CVs of SO-IrNiO_x/C and DO-IrNiO_x/C decreased and eventually disappeared while Ir^{III/IV} waves at ca. 0.9 V developed, indicating that the metallic Ir surface was oxidized to IrO_x. A comparison of the Ir^{III/IV} peaks of all oxidized samples is presented in **Figure 48f**.

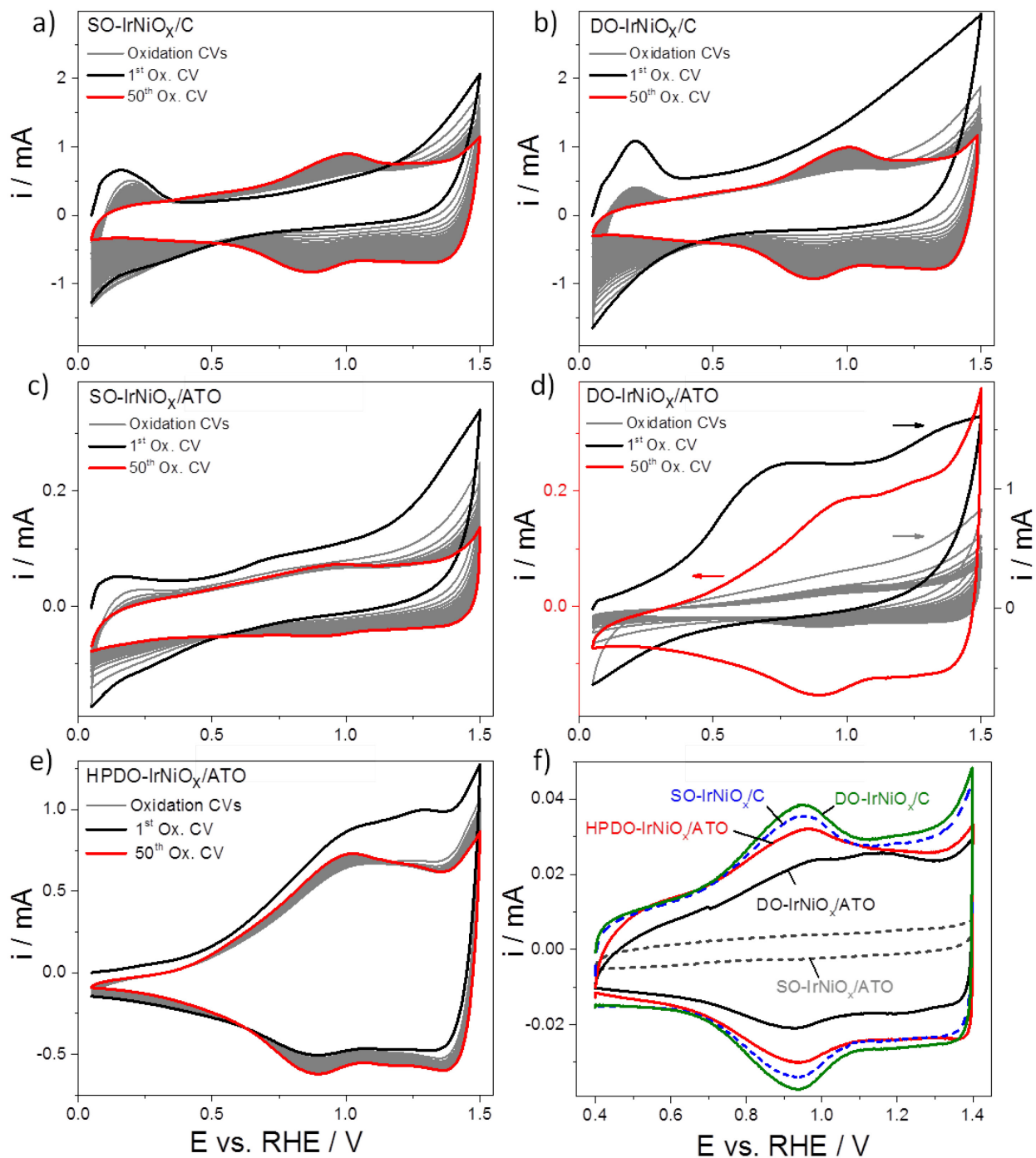


Figure 48. Oxidation cyclic voltammograms of a), b) stepwise- and directly oxidized IrNiO_x supported on carbon (denoted as SO-IrNiO_x/C and DO-IrNiO_x/C, respectively), c), d), e) stepwise-, direct, and high potential directly oxidized IrNiO_x supported on ATO (denoted as SO-IrNiO_x/ATO, DO-IrNiO_x/ATO, and HPDO-IrNiO_x/ATO, respectively). The 1st and 50th CVs are shown to clarify the direction of changes during electrochemical oxidation. The arrows indicate according to which y axis the CVs are plotted. f) Comparison of Ir^{III/IV} redox peaks of all oxidized samples. Condition: 0.05M H₂SO₄, a) to e) scan rate of 500 mV s⁻¹, f) scan rate of 20 mV s⁻¹.

After 50 oxidation cycles, the CV shape of SO-IrNiO_x/C resembled that of DO-IrNiO_x/C, in fact, the number of electrochemically accessible Ir sites estimated from the Ir^{III/IV} redox peak (see section 4.4.1) of SO-IrNiO_x/C and DO-IrNiO_x/C were quite alike (1.61 nmol and 1.76 nmol, respectively). From this, it can be concluded that stepwise oxidation and direct oxidation resulted in rather similar IrO_x shells.⁹⁶ In contrast, the oxidation CVs of SO-IrNiO_x/ATO and DO-IrNiO_x/ATO (**Figure 48c, d**) showed that the tiny H_{upd} waves depleted but the Ir^{III/IV} waves increased only slightly. This indicates that less oxidized IrO_x is present on the surface of SO-IrNiO_x/ATO and DO-IrNiO_x/ATO, and thus less electrochemically active Ir sites are accessible. In the 1st CV of DO-IrNiO_x/ATO (**Figure 48d**), there was an oxidation peak present at ~0.7 V in the anodic scan, and no corresponding reduction peak in the cathodic scan, beside the high current assigned to the Ni dissolution. This is in contrast to the dealloying CVs before the oxidation of SO-IrNiO_x/ATO (**Figure 47b**), which showed that ATO was protected from the irreversible destruction during scanning the potential up to a value of +1.5 V vs. RHE.

Compared to SO-IrNiO_x/ATO, the capacitive current and the Ir^{III/IV} peak current of DO-IrNiO_x/ATO were larger, indicating a higher number of electrochemically accessible active sites. This shows that an additional dealloying step as in the stepwise oxidation is unfavorable for ATO supported samples. The detrimental effect of the dealloying step can be explained by the irreversible destruction of ATO, which might result in lower electrical conductivity of the support and/or dissolution of the support.

In contrast, the capacitive current and the Ir^{III/IV} peak of DO-IrNiO_x/ATO were much smaller compared to those of DO-IrNiO_x/C. Since tin oxide seemed to be protected from destruction when the very first sweep was scanned up to a high potential, the pretreatment was modified accordingly. Before applying the direct oxidation protocol for IrNi_x/ATO, a potential cycle from 1.0 V to 1.8V was applied, then the common DO protocol with 50 cycles from 0.05V to 1.5V at scan rate of 500 mV s⁻¹ was performed. This sample was then denoted as HPDO-IrNiO_x/ATO (HP: high potential). **Figure 48e** presents the oxidation CVs of HPDO-IrNiO_x/ATO. Interestingly, the capacitive currents and the Ir^{III/IV} peak of HPDO-IrNiO_x/ATO were much larger than those of SO- and DO-IrNiO_x/ATO and approached those of SO- and DO-IrNiO_x/C, which indicates that HPDO-IrNiO_x/ATO had a much higher number of active sites compared to SO-

and DO-IrNiO_x/ATO. The impact of the electrochemical accessible active sites on the OER will be discussed later in section 6.3.

6.2. Evolution of IrO_x shells upon electrochemical oxidation

To investigate the evolution of IrO_x shells upon electrochemical oxidation, XPS depth profiles of IrNiO_x/C and IrNiO_x/Meso-ATO at different degrees of oxidation (different number of oxidation cycles) were studied. As discussed above, stepwise oxidation and direct oxidation showed minor effects on carbon supported samples, but stepwise oxidation was unfavorable for ATO supported samples due to irreversible destruction of ATO. In contrast, the high potential direct oxidation appeared to be the most suitable protocol to oxidize Ir in ATO supported IrNi_x nanoparticles (see section 6.1), since it resulted in the largest number of active Ir sites. Therefore, the direct oxidation protocol was used to activate IrNiO_x/C and the high potential direct oxidation protocol was used to activate IrNiO_x/ATO. The samples were investigated by XPS after different number of oxidation cycles (10, 25 or 50 potential cycles). The samples are denoted as IrNiO_x/C-10Cyc, IrNiO_x/C-25Cyc, and IrNiO_x/C-50Cyc (or, respectively, IrNiO_x/ATO-10Cyc, IrNiO_x/ATO-25Cyc, and IrNiO_x/ATO-50Cyc).

For the XPS fitting the Ir 4f-Ni 3p core levels of these partially oxidized samples, we used a procedure with 2 oxidized Ir components.

Iridium is metallic in both precursor alloy samples, except maybe a tiny oxidized component indicated by the fit at the most surface sensitive measurement (KE: 210 eV) (see **Figure 49** and **Figure 50**). There is a strong Ni 3p contribution present in the XP spectra of PA samples due to the high Ni content of the as-prepared samples, which complicates the analysis of Ir.

The XP spectra of the IrNiO_x/C samples are depicted in **Figure 49**. Ir on carbon is feasible to oxidize and additional CV cycles increase the degree of oxidation. After 10 potential cycles, only a small amount of metallic Ir can be seen at the most surface sensitive kinetic energy (KE) of 210 eV. After 25 cycles, no metallic Ir was detected anymore at this KE, indicating that Ir was completely oxidized on the surface. Nevertheless, the strong shoulder at the low binding energy side when probed with a KE of 1200 eV indicates a massive amount of metallic Ir to remain in deeper layers. This shoulder decreased upon increased number of CV cycling suggesting a continuous oxidation of Ir.

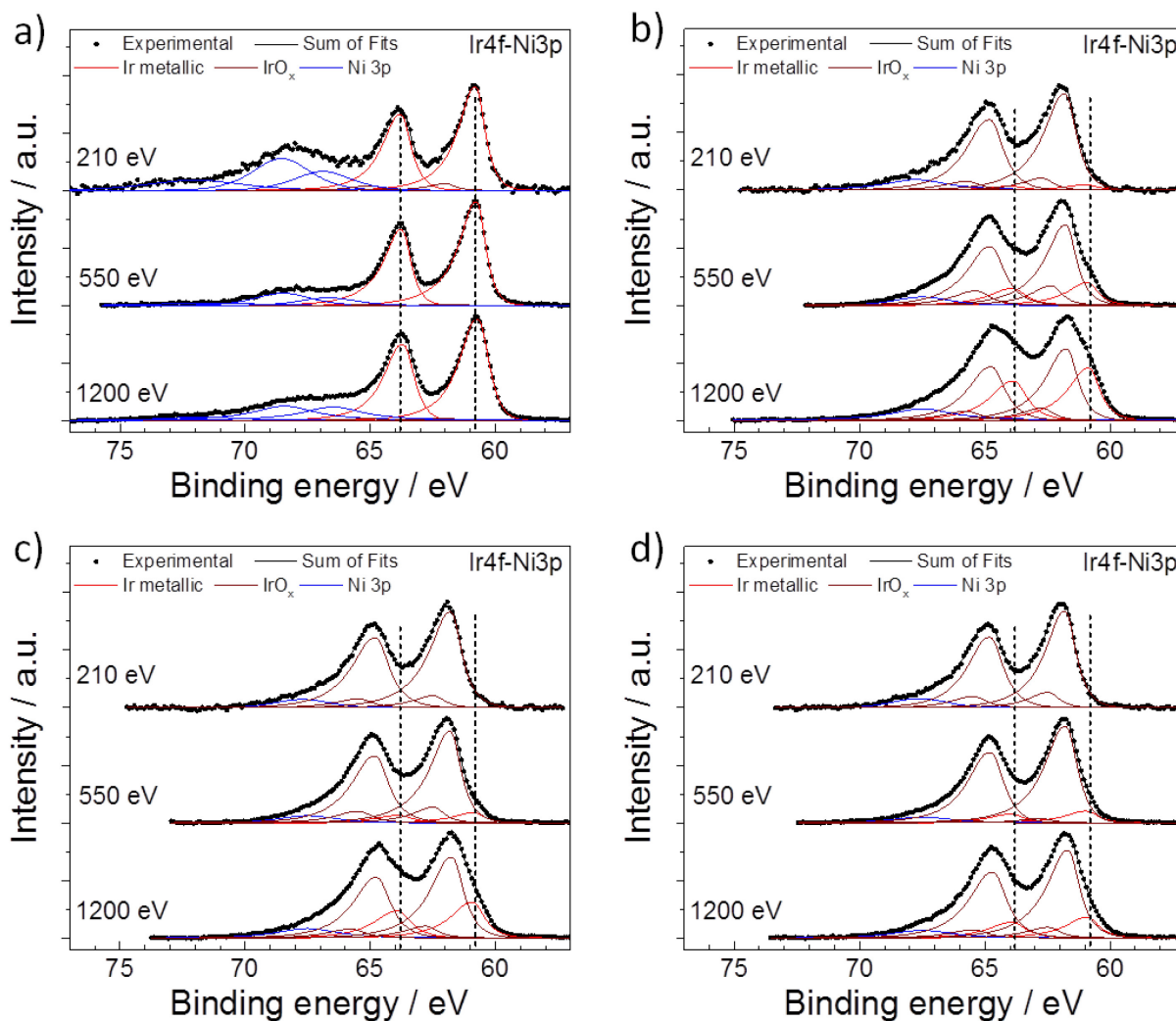


Figure 49. Ir 4f-Ni 3p depth profiles of a) PA-IrNi_x/C, b) IrNiO_x/C -10Cyc, c) IrNiO_x/C-25Cyc, and d) IrNiO_x/C-50Cyc. Vertical dashed lines represent the Ir 4f peak position found in PA-IrNi_x (metallic Ir).

In contrast, Ir was never completely oxidized when supported on ATO (**Figure 50**). In fact, the dominant Ir species upon CV cycling was still metallic Ir. These experiments demonstrated that an increase in the number of CV cycles from 10 through 25 to 50 did not lead to further oxidation of Ir. Actually, fitting indicates rather the opposite; the sample cycled 10 times was slightly more oxidized as compared to those cycled 25 and 50 times. Since the identified differences in the metallic to oxidic Ir ratio are small they attributed to the experimental error. But fact is that after the small initial oxidation, no further Ir oxidation takes place in the additional CV cycles. Interestingly, the Ni 3p contribution is reduced after the first 10 CV cycling but upon additional cycles its intensity remained relatively constant. This is in line with the Ni/Ir ratio (**Table 8**). So, when comparing the oxidation degree of Ir in the two samples after 50

CV cycles, Ir was barely oxidized at the very top layer in IrNiO_x/ATO, whereas in IrNiO_x/C Ir was mostly oxidized even in the bulk.

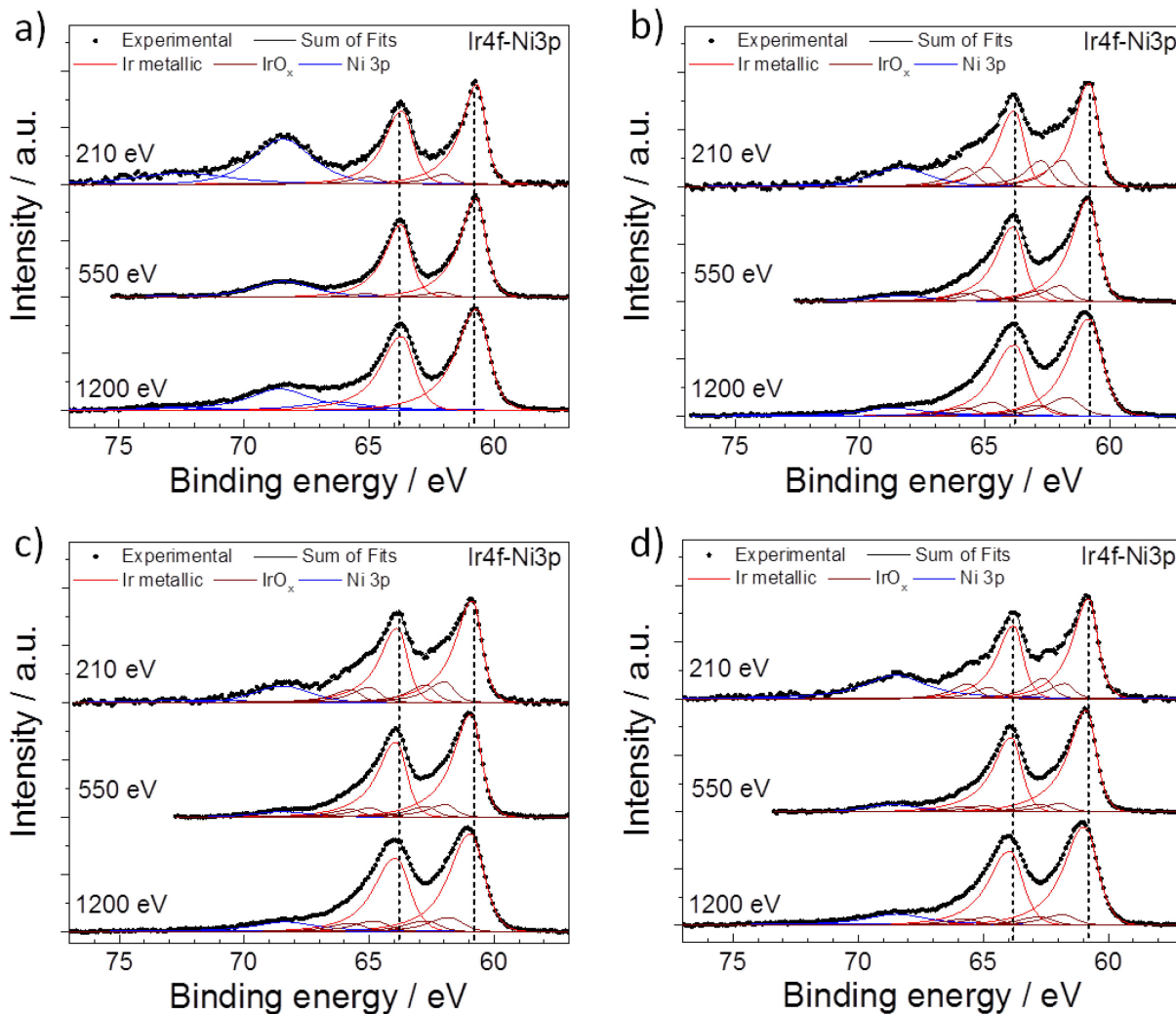


Figure 50. Ir 4f-Ni 3p depth profiles of a) PA-IrNi_x/ATO, b) IrNiO_x/ATO-10Cyc, c) IrNiO_x/ATO-25Cyc, and d) IrNiO_x/ATO-50Cyc. Vertical dashed lines represent the peak position of the metallic Ir 4f signals found in PA-IrNi_x.

The Ni 2p_{3/2} XP spectra of the carbon supported and ATO supported IrNiO_x samples are compiled in **Figure 51**, PA-samples are included for comparison.

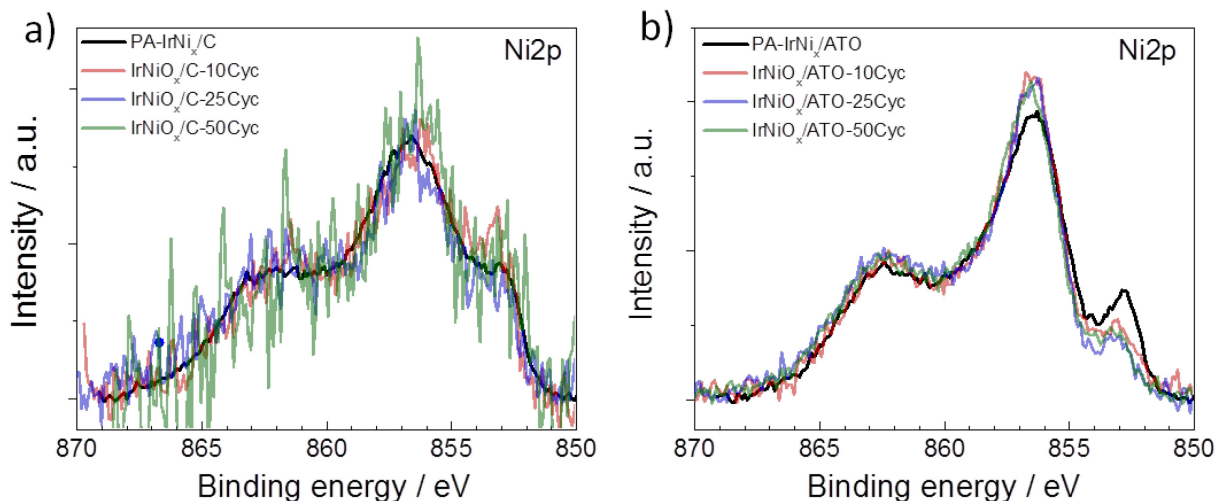


Figure 51. Ni 2p comparison of PA-IrNi_x, IrNiO_x oxidized at 10, 25, and 50 cycles on a) carbon (denoted as PA-IrNi_x/C, IrNiO_x/C-10Cyc, IrNiO_x/C-25Cyc, and IrNiO_x/C-50Cyc, respectively), and b) ATO support (denoted as PA-IrNi_x/ATO, IrNiO_x/ATO-10Cyc, IrNiO_x/ATO-25Cyc, and IrNiO_x/ATO-50Cyc, respectively). All Ni 2p spectra are area normalized.

All samples contained metallic Ni (constituting the Ir-Ni alloy) in various degrees, but the dominant species was oxidized Ni. As discussed before (see section 4.4), it was difficult to determine the exact chemical state of oxidized Ni, however, a pronounced satellite suggests that we have a Ni²⁺ species, although we have a binding energy shift to higher values and lack the resolved doublet structure of crystalline NiO. Therefore, it is possible that we have a kind of hydrated amorphous Ni (II) oxide. Since the spectra shown are area normalized, the decreasing signal-to-noise ratio for the CV cycled samples indicate lower absolute Ni 2p intensities. Notice that the PA-IrNi_x/ATO contained more metallic Ni (low BE peak) than the CV cycled counterparts. On the contrary, the metallic-to-oxidized Ni ratio seemed to be relatively stable in the IrNi_x/C, IrNiO_x/C series, although the signal-to-noise ratio gets very low for the cycled samples as the overall Ni content strongly decreased. The shape of the oxidized Ni component is different for both supports, which might be due to a lower binding energy Ni²⁺ component in the carbon supported samples (between metallic Ni and the main Ni²⁺ peaks). In this case, a more “regular” NiO species could explain the stronger overlap between the metallic and oxidized peaks as well as the overlap between the main oxidized peak and the satellite.

The quantitative results are compiled in **Table 7** and **Table 8** for carbon supported series and ATO supported series, respectively. The Ni content of the IrNi/C samples

decreased strongly after potential cycling. The apparent Ir content (Ir/C ratio) increased for the oxidized samples, which is related to Ni leaching, minimizing the Ni-induced “shielding” of Ir in the XPS study. The high oxygen content is due to strong carbon functionalization during CV.

Table 7. Quantitative XPS results (molar ratios) of PA-IrNi_x/C and IrNiO_x/C series samples. KE: 550 eV.

Samples	Ni/Ir	Ir/C	O/(Ir+Ni)
PA-IrNi _x /C	3.4	0.007	1.8
IrNiO _x /C-10cyc	0.19	0.014	3.7
IrNiO _x /C-25cyc	0.15	0.015	3.7
IrNiO _x /C-50cyc	0.12	0.014	4.5

Table 8. Quantitative XPS results (molar ratios) of PA-IrNi_x/ATO and IrNiO_x/ATO series samples. KE: 550 eV.

Samples	Ni/Ir	Ir/(Sb+Sn)	Sb/Sn	O/(Ir+Ni+Sb+Sn)
PA-IrNi _x /ATO	4.5	0.1	0.09	1.4
IrNiO _x /ATO-10cyc	1.3	0.09	0.07	1.6
IrNiO _x /ATO-25cyc	1.3	0.09	0.07	1.5
IrNiO _x /ATO-50cyc	1.5	0.1	0.08	1.5

The Ni/Ir ratio of PA-IrNi_x/ATO was 4.5. Ni was leached during CV cycling, reducing Ni/Ir ratio to 1.3 - 1.5. No clear difference in the Ni content was found, whether the sample underwent 10, 25 or 50 CV cycles. The Ir/(Sb+Sn) ratio was close to 0.1 throughout the series. Antimony in the ATO supported samples was not completely stable during the electrochemical treatment. The oxygen content of the samples

increased during sample oxidation, which is related to Ir oxidation and functionalization of the glassy carbon substrate. Comparing the two sample series, it can be clearly seen that ATO impedes Ir oxidation and Ni leaching, in line with HE XRD - atomic PDFs and CVs results.

6.3. Impact of electrochemical pretreatment on the OER activity of IrNiO_x core-shell nanoparticles supported on different materials

First, we compare the influences of the electrochemical pretreatment protocols on the OER activities of carbon supported and ATO supported IrNiO_x core-shell nanoparticles (see section 2.3.3 for experimental details). The linear sweep voltammetry (iR corrected) of these catalysts along with their Ir-mass based activities (iR and capacitance corrected) at 300 mV overpotential are presented in **Figure 52**.

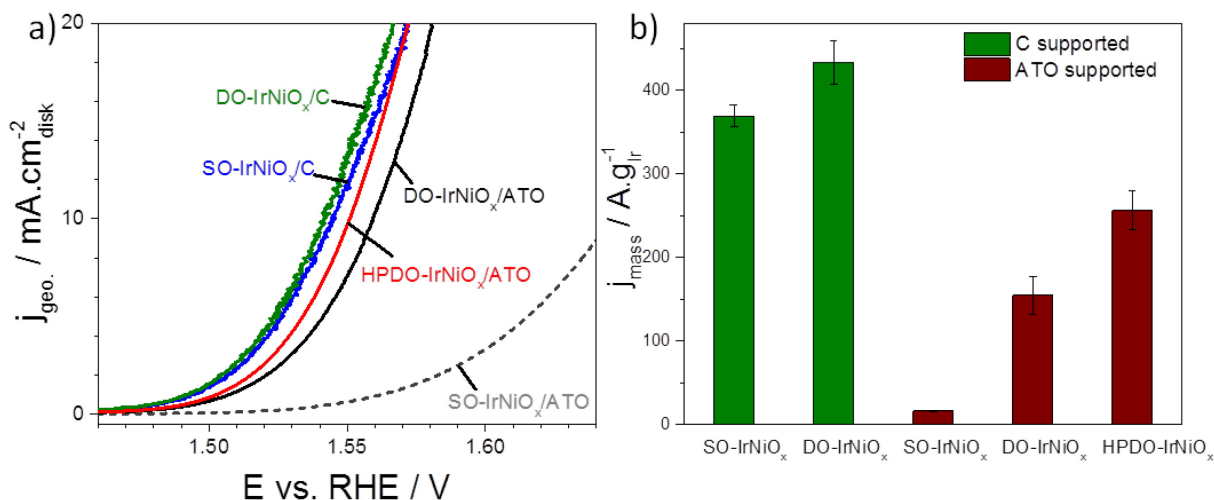


Figure 52. Oxygen evolution reaction (OER) activity of stepwise and directly oxidized IrNiO_x core-shell nanoparticles supported on carbon (denoted as SO-IrNiO_x/C and DO-IrNiO_x/C, respectively), and of stepwise, directly, and high potential directly oxidized IrNiO_x core-shell nanoparticles supported on antimony doped tin oxide (denoted as SO-IrNiO_x/ATO, DO-IrNiO_x/ATO, and HPDO-IrNiO_x/ATO, respectively). a) Linear sweep voltammetry in 0.05M H₂SO₄ at scan rate 5 mV s⁻¹, iR corrected, and b) Ir-mass based activities at 300 mV overpotential, iR- and capacitance corrected.

As discussed in section 6.1 stepwise and direct oxidation showed similar effects on the electrochemical surface properties of IrNiO_x core-shell nanoparticles supported on carbon, which resulted in rather similar geometric and Ir-mass based OER activities of these two catalysts. The OER activity of DO-IrNiO_x/C was only slightly higher than that of SO-IrNiO_x/C, most likely due to higher number of accessible active sites. On the contrary, the OER activities of DO-IrNiO_x/ATO and HPDO-IrNiO_x/ATO

were much higher than that of SO-IrNiO_x/ATO, which is plausible because the stepwise oxidation destroyed the ATO support and, thereby, lowered the number of accessible active sites drastically. HPDO-IrNiO_x/ATO was more active for the OER than DO-IrNiO_x/ATO because the applied initial high potential pretreatment resulted in a higher number of active sites. The most active IrNiO_x/ATO sample was slightly less active than IrNiO_x/C because of a lower number of active sites, but the geometric activity is approaching that of the IrNiO_x/C.

Charge measurements (integration of the anodic sweep of the voltammogram) are often used to compare the electrochemically active surface area (ECSA) of Ir oxide and Ru oxide electrodes,¹¹⁷ as well as IrO₂-RuO₂ supported on ATO,²¹ and IrO₂-SnO₂ binary oxide films.⁶⁸ In case of IrNiO_x/ATO, the charge integrated from anodic sweep of the CVs from 0.4 V to 1.4 V at scan rate of 20 mV s⁻¹ was used to compare the ECSA of the catalysts (**Figure 48f**).

The specific OER activities evaluated at 300 mV overpotential based on the anodic charge of SO-, DO- and HPDO-IrNiO_x/ATO compared with the benchmark DO-IrO_x/ATO are presented in **Figure 53**.

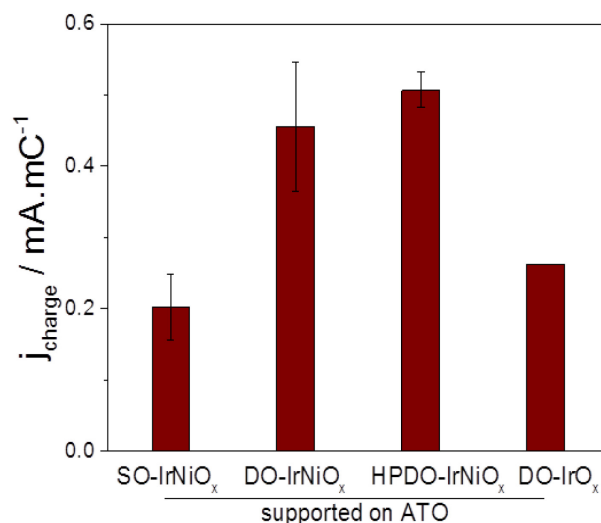


Figure 53. Specific activity at 300 mV overpotential of stepwise-, directly-, and high potential directly- oxidized IrNiO_x core-shell nanoparticles supported on antimony doped tin oxide (denoted as SO-IrNiO_x/ATO, DO-IrNiO_x/ATO, and HPDO-IrNiO_x/ATO, respectively). The specific activity at 300 mV overpotential of directly oxidized IrO_x supported on ATO (DO-IrO_x) was included as a benchmark.

All Ni-containing samples showed a higher specific activity than that of pure DO-IrO_x/ATO, with an exception of SO-IrNiO_x/ATO. The high specific activities of DO-

and HPDO-IrNiO_x/ATO might be resulted from strain effect due to lattice contraction of Ni-containing samples as discussed in section 6.1. Comparing specific activities of ATO supported samples, it can be concluded that the higher Ir-mass based activity of HPDO-IrNiO_x/ATO compared to DO-IrNiO_x/ATO was due to a higher active surface area, and the low Ir-mass based activity of SO-IrNiO_x/ATO resulted not only from low active surface area, but also from the destruction of the oxide support leading to lower specific activity. The high potential direct oxidation treatment ensured a high active surface and high OER activity of the ATO supported catalysts, therefore, this protocol was used as electrochemical pretreatment for other ATO supported samples, as well as for samples discussed earlier in chapter 5.

It was earlier shown that SO-IrNi_x/C and DO-IrNi_x/C also showed higher specific activities at 250 mV overpotential compared to pure IrO_x/C. and the Ni/Ir ratios after the electrochemical oxidation showed no correlation with the OER activity (see chapter 4). From this, the hypothesis that Ni surface centers aid to breaks the scaling relation and improve OER activity might be excluded and the enhanced OER activity can more likely be explained by the strain effect due to the lattice contraction for the IrNiO_x core-shell nanoparticles.

OER activities of IrNiO_x supported on carbon and ATO with different degree of oxidation are shown in **Figure 54**.

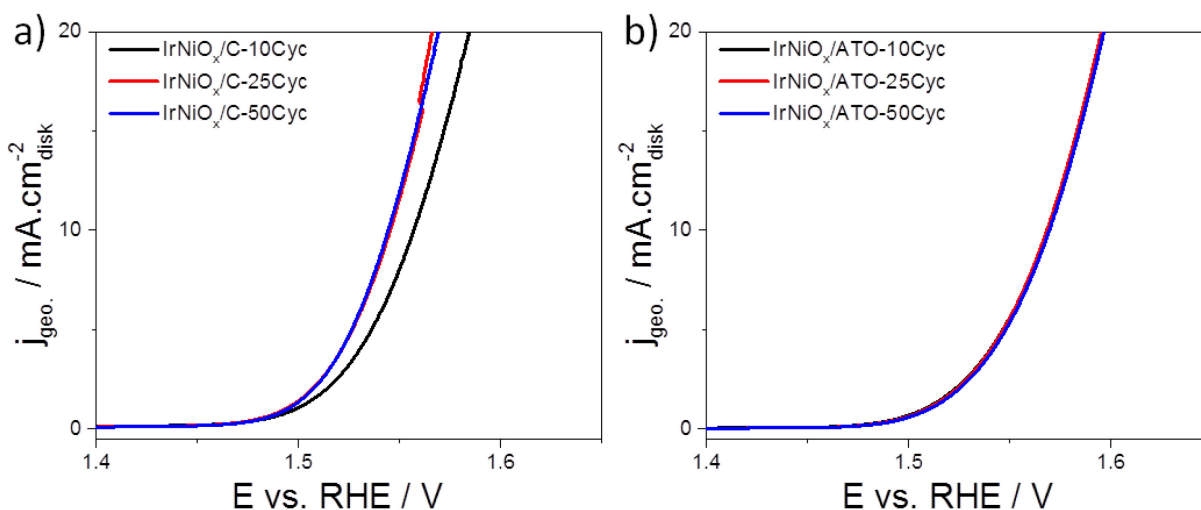


Figure 54. OER activity of a) directly oxidized IrNiO_x supported on carbon after 10, 25 and 50 cycles (denoted as IrNiO_x/C-10Cyc, IrNiO_x/C-25Cyc, and IrNiO_x/C-50Cyc, respectively), and b) high potential directly oxidized IrNiO_x supported on antimony doped tin oxide after 10, 25 and 50 cycles (denoted as IrNiO_x/ATO-10Cyc, IrNiO_x/ATO-25Cyc, and IrNiO_x/ATO-50Cyc, respectively). The measurements were performed in 0.05M H₂SO₄ at a scan rate of 5 mV s⁻¹ and were iR corrected. Ir loading 10.2 μg cm⁻².

For carbon supported samples, from 10 cycles to 25 cycles of oxidation, the OER activity increased, as the oxidation degree of Ir on the surface increased. However, further oxidizing Ir in the bulk (IrNiO_x/C-50Cyc) did not increase the OER activity compared to IrNiO_x/C-25Cyc. For ATO supported IrNiO_x, since number of oxidation (10, 25 or 50 cycles) did not lead to an increase of the OER activities of IrNiO_x/ATO, similar to the oxidation behavior of Ir on the surface. With this, it can be concluded that surface IrO_x shows a strong effect on OER activity, whereas bulk IrO_x shows very little or no effect. This indicates that the OER happens mostly on the IrO_x surface of the nanoparticles.

6.4. Summary

In summary, due to stability problems of the ATO support at low potentials, the electrochemical pretreatments of the ATO supported IrNi_x precursor alloys has to be wisely chosen in order to obtain comparably high OER activity of the core-shell nanoparticles supported on ATO and carbon.

The structure evolution of the IrNiO_x nanoparticles under different electrochemical pretreatments was investigated and compared with effect of the support materials. In particular, when supported on carbon, the alloy nanoparticles underwent stronger structural changes than those supported on ATO because larger amounts of Ni were removed during the electrochemical treatment in case of the carbon supported nanoparticles. Electrochemical dealloying and Ir oxide formation played an important role in order to realize high OER activity of ATO supported IrNi@IrO_x nanoparticles. An initial high potential pretreatment turned out to be crucial for the stability of the ATO support in the electrochemical treatment. Applying this high potential pretreatment the OER activity of ATO supported samples approached the OER activity of carbon supported samples. In contrast, dealloying at lower potentials (from 0.05 to 0.8 V) led to the destruction of ATO and lowered the OER activity dramatically.

Combined with earlier findings that OER specific activity is not correlated with the Ni/Ir ratio, we proposed that the enhanced OER activity in Ni-containing IrNi@IrO_x core-shell nanoparticles resulted from strain effect due to the lattice contraction, which was evidenced by HE XRD in combination with atomic PDFs.

7. IrNi_x Nanoparticles Supported on Mesoporous ATO-Impact of Ni Content in Precursor Alloys

7.1. Precursor alloy IrNi_x nanoparticles supported on mesoporous ATO (PA-IrNi_x/Meso-ATO) with different Ni contents

Applying optimized synthetic conditions for the polyol method (see chapter 3), we synthesized a series of precursor alloy IrNi_x nanoparticles supported on mesoporous ATO (denoted as PA-IrNi_x/Meso-ATO) with a wide range of Ni contents. **Table 9** compiles nominal Ir : Ni molar ratios and Ir loadings (calculated from the initial amount of Ni and Ir precursor in the reaction mixture) compared to actual compositions derived from ICP-OES of the as-synthesized samples. The actual compositions of as-synthesized IrNi_x nanoparticles supported on Meso-ATO are quite close to nominal Ir : Ni ratios and Ir loadings, showing the applicability of our established synthetic conditions for IrNi alloy nanoparticles with tunable Ni content.

Table 9. Nominal and actual atomic compositions derived from ICP-OES of PA-IrNi_x/Meso-ATO samples

Sample	Ir:Ni molar ratio		Ir loading (wt. %)		Actual composition
	Nominal	Actual	Nominal	Actual	
Ir ₄ Ni/Meso-ATO	1:0.25	1:0.28	20	18.7	18.7%IrNi _{0.28} /Meso-ATO
IrNi/Meso-ATO	1:1	1:1.2	20	16.8	16.8%IrNi _{1.2} /Meso-ATO
IrNi ₂ /Meso-ATO	1:2	1:2.6	20	16.1	16.1%IrNi _{2.6} /Meso-ATO
IrNi ₃ /Meso-ATO	1:3	1:3.3	20	19.4	19.4%IrNi _{3.3} /Meso-ATO
IrNi ₆ /Meso-ATO	1:6	1:6.8	20	16.9	16.9%IrNi _{6.8} /Meso-ATO

The actual Ni content in IrNi_x nanoparticles supported on either Meso-ATO or carbon (PA-IrNi_x/Meso-ATO and PA-IrNi_x/C) is slightly higher than the nominal value (**Figure 55**), most likely due to the fact that the Ir precursor solution was hot injected

in the Ni precursor containing reaction mixture at the desired reaction temperature, at which a number of seeds of Ni might have already formed. There is no big difference between the Ni content of PA-IrNi_x/Meso-ATO and PA-IrNi_x/C when started from the same nominal Ni content, suggesting that adding Meso-ATO to reaction the mixture (see synthesis procedures in chapter 2) showed little effect on the formation of the IrNi_x nanoparticles. The actual Ni content shows a linear relation with nominal Ni content, suggesting that any Ni content (from 20 up to ~ 90 molar %) can conveniently be synthesized with the present optimized polyol method.

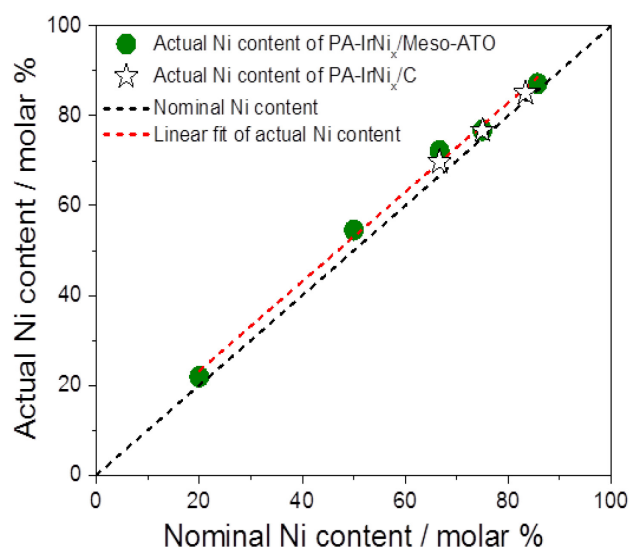


Figure 55. Relation between nominal and actual Ni content (molar %) in IrNi_x nanoparticles supported on mesoporous ATO (PA-IrNi_x/Meso-ATO) and on carbon (PA-IrNi_x/C).

XRD patterns of PA-IrNi_x/Meso-ATO, $x = 0.28, 1.2, 2.6, 3.3,$ and 6.8 (**Figure 56a**) showed typical reflections between 40 and 45° , corresponding to (111) planes of the alloy crystallites.⁹⁶ Similar to carbon supported IrNi_x nanoparticles, there is no superlattice peak discernible below 35° (beside reflections corresponding to ATO support), indicating a substitutional solid solution structure of the alloys. The (111) reflections clearly increased in intensity and shifted toward higher 2θ with increasing Ni content x (see **Figure 56b**), indicating a contraction of the lattice with an increasing amount of smaller Ni atoms included in the alloy. This indicates the good alloying of Ir atoms with smaller Ni atoms at any given Ni content.

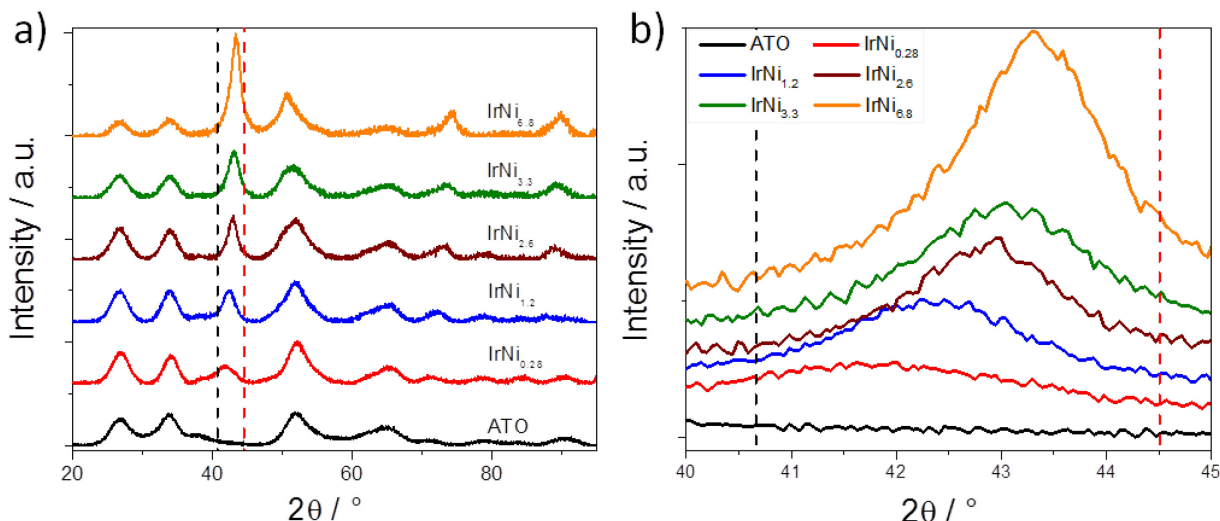


Figure 56. a) XRD patterns of IrNi_x nanoparticles ($x = 0.28, 1.2, 2.6, 3.3,$ and 6.8) supported on mesoporous ATO (PA-IrNi_x/Meso-ATO), and b) a zoom on reflections between 40° and 45° 2θ . Black and red vertical dashed lines indicate database (111) reflections of pure Ir and pure Ni, respectively.

The relationship between the interplane distance $d_{(111)}$ and the Ni content of the PA-IrNi_x/Meso-ATO (**Figure 57a**) shows a positive deviation from the ideal Vegard's law, except for the Ir-rich sample IrNi_{0.28}.

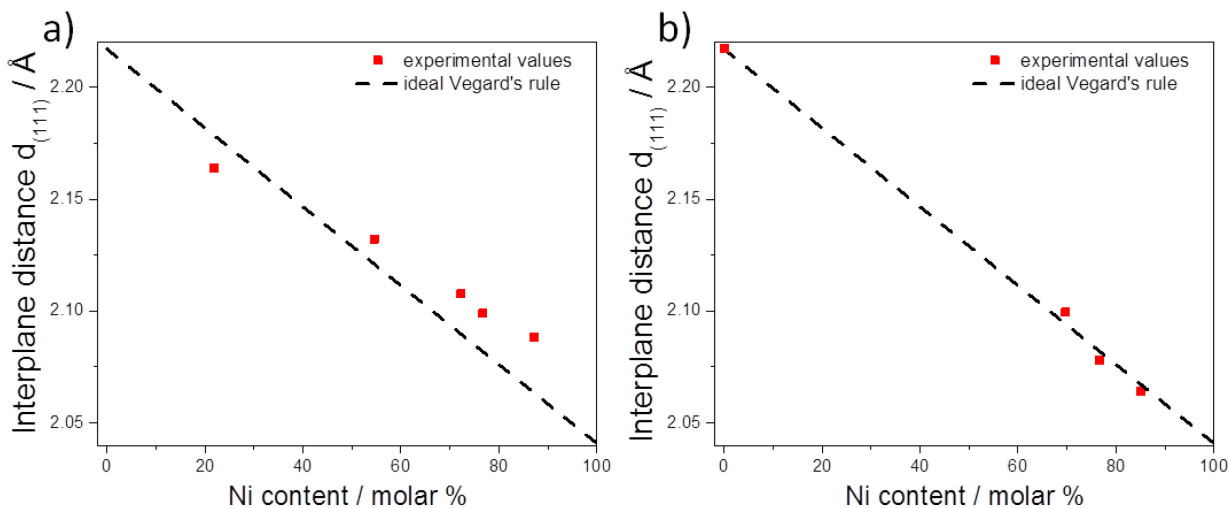


Figure 57. The relationship between interplane distance of (111) planes ($d_{(111)}$) and Ni content (red symbols) of a) mesoporous ATO supported IrNi_x nanoparticles ($x = 0.28, 1.2, 2.6, 3.3,$ and 6.8) (denoted as PA-IrNi_x/Meso-ATO), and b) carbon supported IrNi_x nanoparticles ($x = 0, 2.3, 3.3,$ and 5.7) (denoted as PA-IrNi_x/C) compared to Vegard's rule (dashed lines).

The interplane distance $d_{(111)}$ of PA-IrNi_x/Meso-ATO does not follow Vegard's rule as closely as that of IrNi_x nanoparticles supported on carbon (**Figure 57b**), indicating a slightly lower atomic mixing of Ir and Ni in PA-IrNi_x/Meso-ATO compared to in PA-

IrNi_x/C. This is plausible, since PA-IrNi_x/C samples were annealed in H₂ at 400 °C to help enhancing atomic mixing of Ir and Ni, whereas PA-IrNi_x/Meso-ATO samples were annealed at 180 °C in N₂ to avoid Ni oxide segregation and reduction of the oxide support (see chapter 2 and 5).

Figure 58 depicts Ir 4f Ni 3p XPS depth profiles of the PA-IrNi_x/Meso-ATO samples.

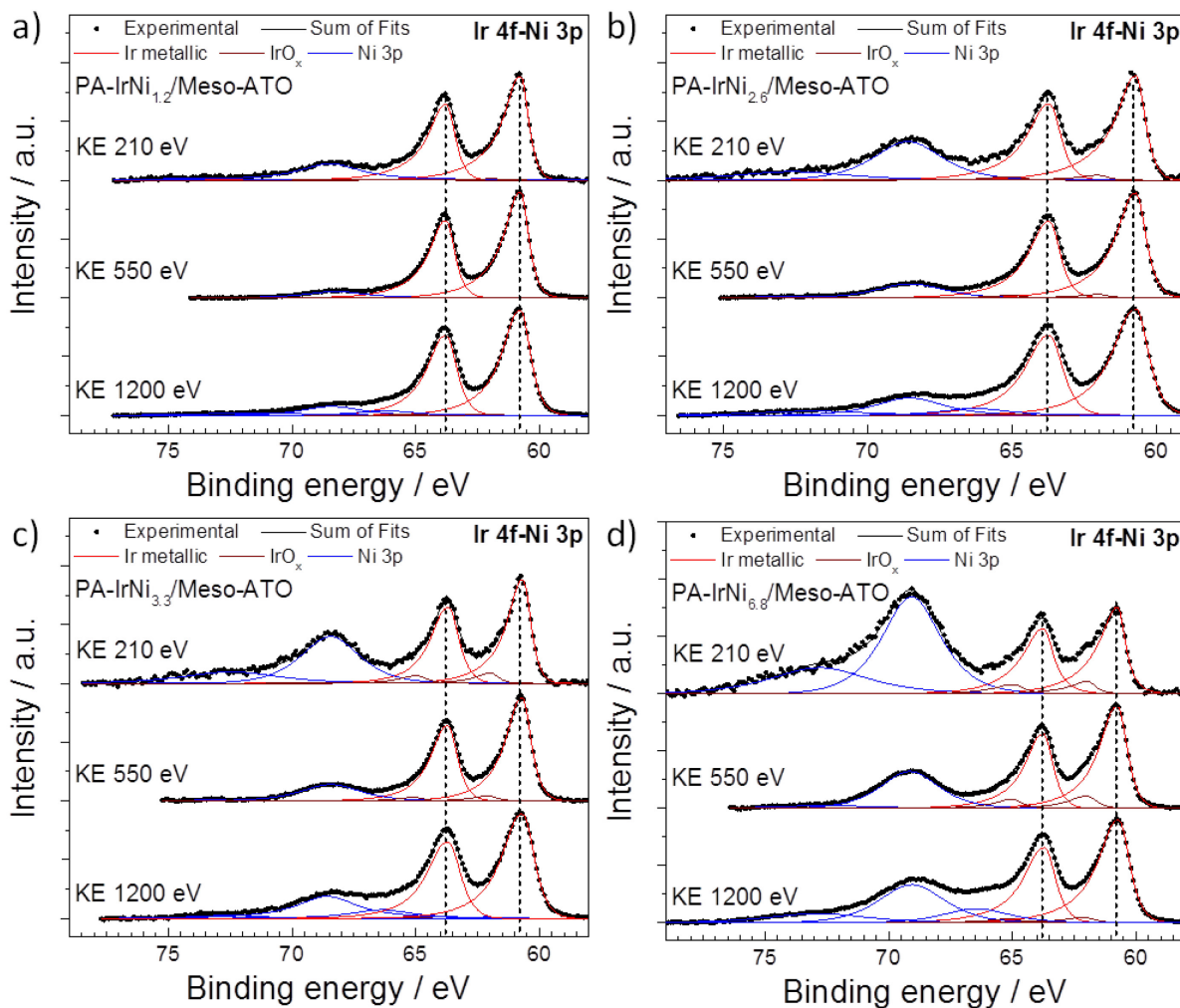


Figure 58. Ir 4f Ni 3p XPS depth profiles of precursor alloy IrNi_x nanoparticles supported on mesoporous ATO (PA-IrNi_x/Meso-ATO). a) PA-IrNi_{1.2}/Meso-ATO, b) PA-IrNi_{2.6}/Meso-ATO, c) PA-IrNi_{3.3}/Meso-ATO, and d) PA-IrNi_{6.8}/Meso-ATO. Vertical dashed lines indicate peak position of metallic Ir.

Ir is mostly metallic in all precursor alloy samples, except a very small oxidized component at the surface of the samples with high Ni content (IrNi_{2.6} and above). Notice also the increasing Ni 3p signal at the high binding energy side with increasing Ni content.

The Ni 2p XPS of PA-IrNi_x/Meso-ATO (**Figure 59a**) show that all precursor alloy samples contain Ni in metallic and oxidized form. Similar to previous IrNi_x/C samples (see chapter 4), Ni in the near surface region is mostly oxidized, but clearly some metallic Ni is constituted in the Ir-Ni alloy. As discussed in section 5.1, the oxidic Ni peaks do not resemble bulk NiO, but still the large satellite suggests a Ni²⁺ state in all investigated compositions. When area normalized, the most metallic Ni is observed in PA-IrNi_{1.2}/Meso-ATO; however, when we take the larger Ni excess on the surface with the samples with higher Ni nominal loading into consideration, the absolute amount of Ni included in the alloy phase is higher for higher Ni loadings.

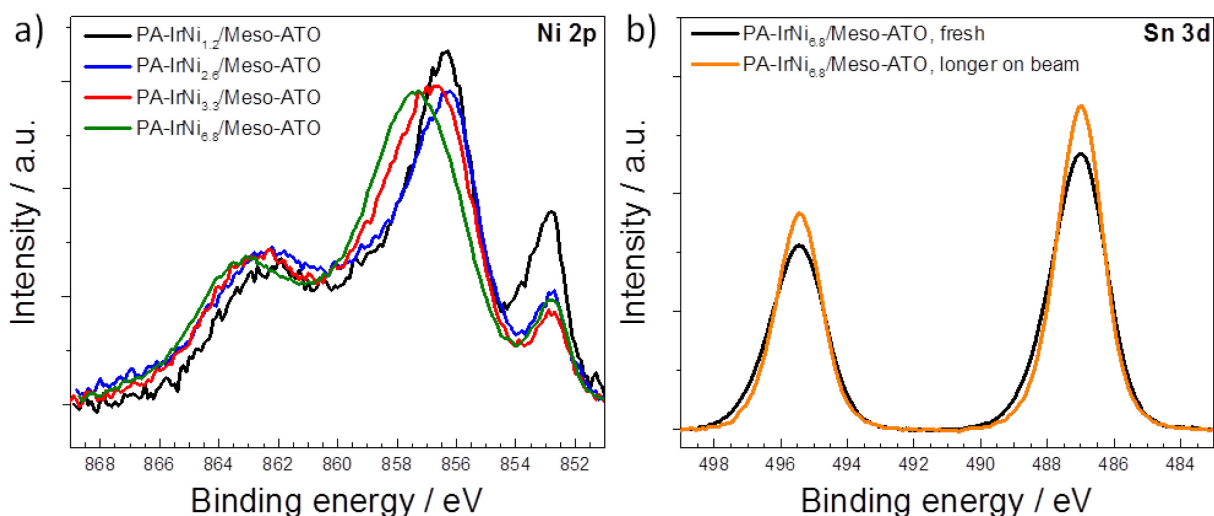


Figure 59. a) Ni 2p XPS comparison of the precursor alloy IrNi_x nanoparticles supported on mesoporous antimony doped tin oxide (PA-IrNi_x/Meso-ATO). All Ni 2p spectra are area normalized. b) Sn 3d comparison of PA-IrNi_{6.8}/Meso-ATO in a fresh beam spot and after longer irradiation.

Overall, the XPS results suggest that we have basically IrNi metallic alloys with a slightly oxidized surface (both Ir and Ni), which is in contrast with the carbon supported precursor alloy samples, where only Ni was oxidized on the surface (see chapter 4). This is because PA-IrNi_x/Meso-ATO samples were annealed in O₂ and then N₂ atmosphere to avoid reducing of the oxide support (Meso-ATO), whereas PA-IrNi_x/C samples were annealed in O₂ and then H₂ atmosphere which helped reducing oxidized surface of IrNi nanoparticles.

Interesting beam sensitivity was observed in the Sn 3d core levels. The Sn 3d of PA-IrNi_{6.8}/Meso-ATO is compared in a fresh spot and after longer irradiation (**Figure 59b**), the peaks get narrower upon longer beam irradiation, suggesting at

least a partial transformation of beam sensitive ATO particles into less beam sensitive ones.

The near surface composition of PA-IrNi_x/Meso-ATO samples is compiled in **Table 10**.

Table 10. Quantitative XPS results of PA-IrNi_x/Meso-ATO samples. KE: 550 eV. Molar ratios are shown.

Samples	Ni/Ir	Ir/(Sb+Sn)	Sb/Sn	O/(Ir+Ni+Sb+Sn)
PA-IrNi _{1.2} /Meso-ATO	1.7	0.11	0.17	1.5
PA-IrNi _{2.6} /Meso-ATO	3.2	0.11	0.12	1.5
PA-IrNi _{3.3} /Meso-ATO	4.5	0.1	0.09	1.4
PA-IrNi _{6.8} /Meso-ATO	11.2	0.13	0.1	1.1

The surface Ni content of PA-IrNi_x/Meso-ATO with $x \leq 3.3$ is slightly higher than corresponding bulk Ir : Ni ratio derived from ICP-OES, indicating slightly Ni surface enrichment. There is some variation in the Sb/Sn ratio as a function of Ni loading in the precursor alloy samples. In fact, the Sb/Sn ratio decreases with higher Ni content, which hints to a Ni-induced Sb leaching during preparation.

From ICP-OES, XRD and XPS results, we can say that we have successfully synthesized a wide range of precursor alloy IrNi_x nanoparticles supported on Meso-ATO with controllable composition and well-alloyed structure, which is suitable for the preparation of the core-shell oxide architecture.

7.2. ATO supported IrNiO_x core-shell nanoparticles synthesized from precursor alloys with different initial Ni contents

7.2.1. The surface electrochemistry of IrNiO_x core-shell nanoparticles

For electrochemical pretreatment of the Meso-ATO supported nanoparticles, learning from previous experiments, we applied the high potential direct oxidation to protect ATO from destruction (see section 2.3.3 and 6.3). The samples then are denoted as Ox-IrNi_x/Meso-ATO with x representing the molar ratio of Ni in the corresponding

precursor alloy ($x = 1.2, 2.6, 3.3,$ and 6.8). Electrochemical oxidized IrO_x/Meso-ATO prepared from pure Ir nanoparticles supported on Meso-ATO is used as benchmark.

Cyclic voltammetry was used to characterize the electrochemical behavior of the Ox-IrNi_x/Meso-ATO samples. The CVs from 0.4 V to 1.4 V vs. RHE with a scan rate of 20 mV s⁻¹ of all oxidized samples are compared in **Figure 60**. Overall the shape of the CVs exhibits the broad waves consistent with the shape of CVs measured for electrochemical oxidized IrO_x and IrNiO_x supported on carbon (see chapter 4). The broad wave features on catalysts result from the solid-state redox reactions in which the surface Ir can be oxidized or reduced accompanied by proton exchange between the oxide and the electrolyte. Thus the capacitance of the oxidized IrNi_x on ATO is a combination of the pseudo-capacitance resulting from charge storage by the solid-state redox reactions and the standard double layer capacitance resulting from charge storage within the electrode-electrolyte interface.

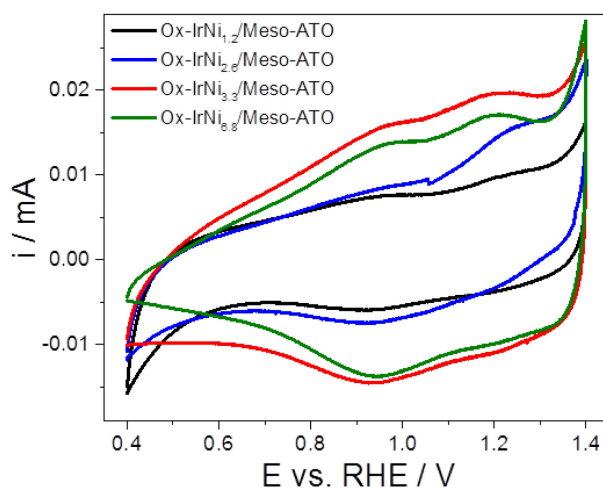


Figure 60. Cyclic voltammograms from 0.4 to 1.4 V vs. RHE at scan rate 20 mV s⁻¹ of oxidized IrNi_x nanoparticles supported on mesoporous antimony doped tin oxide (Ox-IrNi_x/Meso-ATO, x represents molar ratio of Ni in the corresponding precursor alloys, $x = 1.2, 2.6, 3.3,$ and 6.8). Conditions: 0.05M H₂SO₄, Ir loading 10.2 μg cm⁻².

As explained in section 6.3, we can use the integrated charge from anodic sweep of the CVs from 0.4 V to 1.4 V at scan rate of 20 mV s⁻¹ to compare the electrochemically active surface area (ECSA) of Ir oxide. Here, we use the so-called Meso-ATO-corrected charge ($q_{\text{Meso-ATO corrected}}$) to compare the ECSA of the Ox-IrNi_x/Meso-ATO catalysts as a function of the initial Ni content. Since the amount of Meso-ATO oxide support is varied in each PA-IrNi_x/Meso-ATO sample, the charge contributed by Meso-ATO needs to be corrected for. To do this, first we performed

charge measurement for pure Meso-ATO at otherwise identical conditions, integrated the charge from anodic sweep of the CV from 0.4 V to 1.4 V at scan rate of 20 mV s⁻¹, the same as for other samples, and divided it by the actual mass of Meso-ATO on the electrode. The obtained value ($q_{\text{Meso-ATO density}}$) is 0.01025 mC $\mu\text{g}^{-1}_{\text{Meso-ATO}}$. The charge contribution of Meso-ATO ($q_{\text{Meso-ATO}}$) in each Meso-ATO supported nanoparticle catalyst is calculated by multiplying $q_{\text{Meso-ATO density}}$ with actual mass of Meso-ATO on electrode (**Table 11**). The $q_{\text{Meso-ATO corrected}}$ is then evaluated by subtracting $q_{\text{Meso-ATO}}$ from the total anodic integrated charge ($q_{\text{integrated}}$), and represents effect of Ni-content in precursor alloys to ECSA of the corresponding IrNiO_x nanoparticles.

Table 11. Charge contribution of Meso-ATO in each sample calculated from mass of Meso-ATO on electrode and a charge density of 0.01025 mC $\mu\text{g}^{-1}_{\text{Meso-ATO}}$.

Sample	Ir loading (% wt.)	Mass of Meso-ATO on electrode (μg)	Charge contribution of Meso-ATO (mC)
Ox-IrNi _{1.2} /Meso-ATO	16.8	6.5	0.066
Ox-IrNi _{2.6} /Meso-ATO	16.1	7.3	0.074
Ox-IrNi _{3.3} /Meso-ATO	19.4	6.0	0.062
Ox-IrNi _{6.8} /Meso-ATO	16.9	4.2	0.043
IrO _x /Meso-ATO	20	8.0	0.082

The Meso-ATO-corrected charge of the Ox-IrNi_x/Meso-ATO catalysts as a function of the initial Ni content is presented in **Figure 61**, the pure IrO_x/Meso-ATO prepared from pure Ir nanoparticles supported on Meso-ATO is included as 0 % Ni sample.

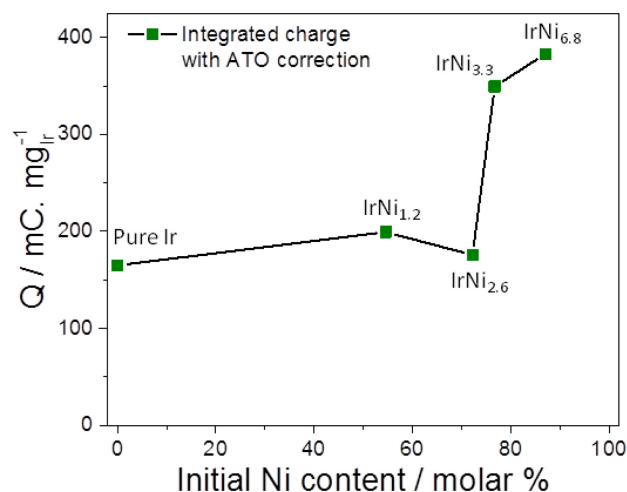


Figure 61. Meso-ATO corrected charge of Ox-IrNi_x/Meso-ATO (x = 1.2, 2.6, 3.3, and 6.8) samples as function of the initial Ni content in the corresponding precursor alloys. Charge of the pure oxidized Ir supported on Meso-ATO is shown as the 0 % Ni benchmark. Conditions: 0.05M H₂SO₄, Ir loading 10.2 μg cm⁻².

The charge of Ox-IrNi_{1.2}/Meso-ATO and Ox-IrNi_{2.6}/Meso-ATO is quite similar to that of the pure IrO_x/Meso-ATO benchmark, suggesting similar ECSAs. Interestingly, the charge of Ox-IrNi_{3.3}/Meso-ATO is much higher than that of Ox-IrNi_{2.6}/Meso-ATO, although the Ni content in corresponding precursor alloy is not much different. Ox-IrNi_{6.8}/Meso-ATO shows slightly higher charge than Ox-IrNi_{3.3}/Meso-ATO. This might presumably be due to increased surface roughness and defects during the massive removal of Ni and the surface rearrangement during simultaneous dealloying and oxidation, resulting in higher active surface area.

7.2.2. Surface chemical state and composition of IrNiO_x core-shell nanoparticles after oxidation and OER tests

Ir 4f Ni 3p XPS depth profiles of all Ox-IrNi_x/Meso-ATO samples are compared in **Figure 62**. In order to obtain reasonable results, the fitting of all oxidized samples required utilization of 3 Ir peaks (1 metallic and 2 oxidized peaks).

Similar to the observation before (see chapter 6), Ir is never completely oxidized, but only few layers on the surface when supported on mesoporous ATO. Large contribution of metallic Ir was found in the Ir 4f spectra.

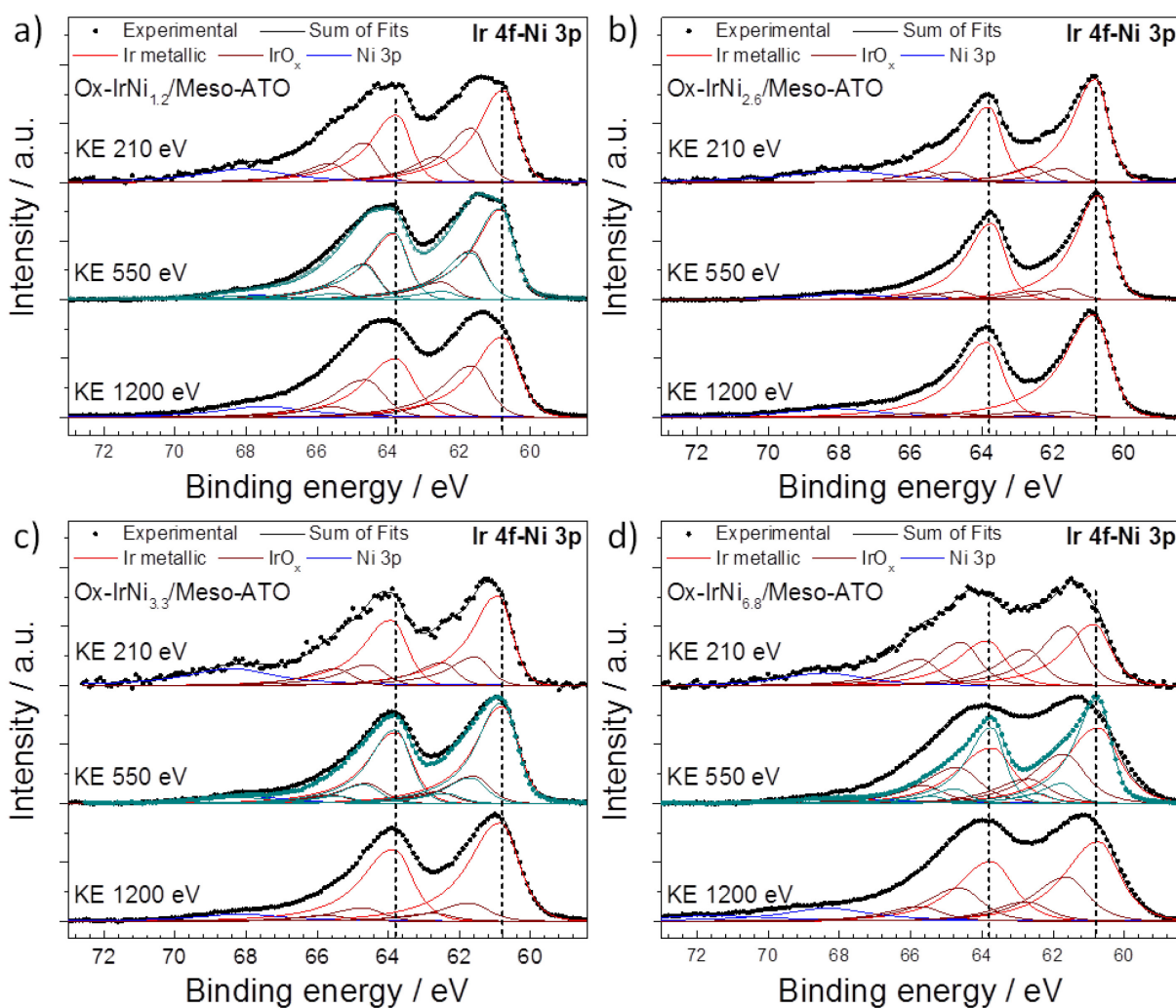


Figure 62. Ir 4f-Ni 3p XPS depth profiles of oxidized IrNi_x nanoparticles supported on mesoporous antimony doped tin oxide (Ox-IrNi_x/Meso-ATO). a) Ox-IrNi_{1.2}/Meso-ATO, b) Ox-IrNi_{2.6}/Meso-ATO, c) Ox-IrNi_{3.3}/Meso-ATO, and d) Ox-IrNi_{6.8}/Meso-ATO. In black fresh beam spot spectra are shown. In cyan spectra (550 eV KE) are overlaid recorded after longer irradiation. Vertical dashed lines indicate peak position of metallic Ir.

Ox-IrNi_{1.2}/Meso-ATO: The low binding energy side rises fast until near 61 eV, where it reaches almost a plateau. At ~61.6 eV the intensity starts slowly decreasing but even at ~63 eV the intensity is high. Due to the unknown degree of asymmetry, the exact determination of peak contribution and position “by eye” is not clear, but the fitting suggests that *i*) the sharp rise of the low binding energy side is related to metallic Ir, *ii*) two oxidized Ir peaks are mandatory for satisfactory fitting, and *iii*) the binding energy of the low BE oxidized peak is ~61.7 eV and the high BE oxidized peak is ~ 62.6 - 62.7 eV. The difference is though that here the metallic Ir is the most intense species. There is weak beam sensitivity, as the high binding energy oxide is attenuated upon longer irradiation, but the other species are not.

Ox-IrNi_{2.6}/Meso-ATO: Again, we see the relative sharp rise of the low binding energy side at the energy of the metallic Ir, but the high binding energy side of the spectrum is very weak, and the oxidized Ir species are in the minority. With this sample the longer beam exposed spectrum is not included, as it is identical to the fresh spot spectrum.

Ox-IrNi_{3.3}/Meso-ATO: Here again we find a small hint of a plateau, but this is smaller than Ox-IrNi_{1.2}/Meso-ATO, which indicates only an intermediate oxide contribution. The metallic peak is the dominating one and we find some beam sensitivity in the high binding energy oxide side.

Ox-IrNi_{6.8}/Meso-ATO: The spectra are much broader than the others and there are indications that this is caused by differential charging of instable materials. The spectrum after longer beam exposure (cyan line) is much narrower, which is in line with the narrower Sn 3d peak after the same longer beam exposure (**Figure 63b**). Actually the strong low binding energy tailing is a clear sign that we deal with differential charging here. Since metallic Ir should not charge, the strong broadening is most probably related to the support. On the other hand, the strong metallic peak after long beam exposure is probably partially a result of beam induced degradation of some oxidized species.

Ni 2p (3/2) XPS of oxidized samples (**Figure 63a**) show that Ox-IrNi_x/Meso-ATO samples contain again both metallic and oxidized Ni species, though the metallic contribution of Ox-IrNi_{3.3}/Meso-ATO and Ox-IrNi_{6.8}/Meso-ATO is low. Ni content in Ox-IrNi_x/Meso-ATO samples decreased compared to Ni content in corresponding PA-IrNi_x/Meso-ATO samples, evidenced by decreased signal to noise ratio.

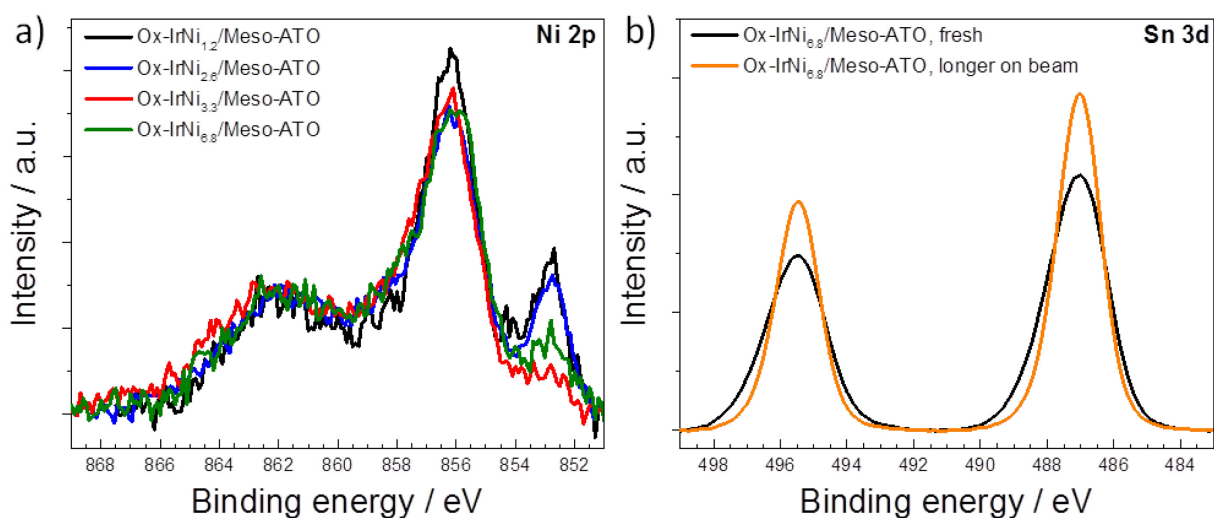


Figure 63. a) Ni 2p XPS comparison of electrochemically oxidized IrNi_x nanoparticles supported on mesoporous antimony doped tin oxide (Ox-IrNi_x/Meso-ATO). All Ni 2p spectra are area normalized. b) Sn 3d XPS comparison of oxidized Ox-IrNi_{6.8}/Meso-ATO in a fresh beam spot and after longer irradiation.

The quantitative XPS results of oxidized samples and OER tested samples are compiled in **Table 12**.

Table 12. Quantitative XPS results of Ox-IrNi_x/Meso-ATO samples. KE: 550 eV. Molar ratios are shown.

Samples	Ni/Ir	Ir/(Sb+Sn)	Sb/Sn	O/(Ir+Ni+Sb+Sn)
Ox-IrNi _{1.2} /Meso-ATO	0.43	0.11	0.09	2.0
Ox-IrNi _{2.6} /Meso-ATO	0.8	0.12	0.07	1.9
Ox-IrNi _{3.3} /Meso-ATO	1.0	0.11	0.05	2.0
Ox-IrNi _{6.8} /Meso-ATO	0.8	0.16	0.06	1.5

After electrochemical oxidation in acidic medium, Ni was effectively removed from surface of the nanoparticles. Interestingly, Ni content of oxidized samples is not directly correlated to the initial Ni content in the corresponding precursor alloy. Ni/Ir ratio reduces to ~ 0.8 – 1 after oxidation, although the initial surface Ni/Ir ratios varied from 3.2 to 11.2 (**Table 10**). For the Ox-IrNi_{1.2}/Meso-ATO sample, Ni/Ir ratio

decreases to 0.43, since Ni was removed from the initial ratio of 1.7. The Ir loading appears relatively stable after oxidation. The Sb/Sn ratio of Ox-IrNi_x/Meso-ATO decreases compared to that of corresponding precursor alloy, indicating that Sb is quite unstable in ATO network. The oxygen content of the samples increases during sample oxidation, which is related to Ir oxidation.

To investigate the structural changes of IrNiO_x core-shell nanoparticles supported on Meso-ATO under OER conditions, XPS of the two most active catalysts (discussed in the section 7.3) after 3 hours of OER tests at 1.54 V vs. RHE (referred to as IrNi_{3.3}/Meso-ATO-OER and IrNi_{6.8}/Meso-ATO-OER) were measured. Ir 4f depth resolved profiles of IrNi_{3.3}/Meso-ATO-OER and IrNi_{6.8}/Meso-ATO-OER are presented in **Figure 64**.

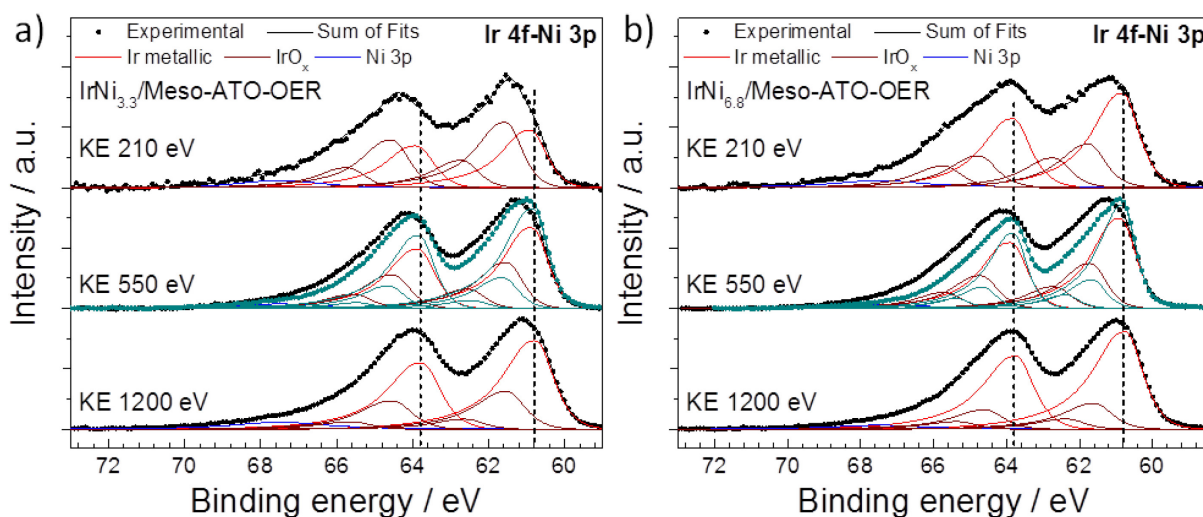


Figure 64. Ir 4f-Ni 3p depth profiles of OER tested samples a) IrNi_{3.3}/Meso-ATO-OER and b) IrNi_{6.8}/Meso-ATO-OER. In black fresh beam spot spectra are shown. In cyan spectra (550 eV KE) are overlaid recorded after longer irradiation. Vertical dashed lines indicate peak position of metallic Ir.

Compared to corresponding oxidized samples, OER treated samples showed higher oxidation degree.

IrNi_{3.3}/Meso-ATO-OER: The low binding energy side indicates a shoulder that fits to metallic Ir. However the maximum is reached at higher binding energies as compared to Ox-IrNi_{3.3}/Meso-ATO, and thus the contribution of oxidized Ir is higher. There is some beam sensitivity, as both oxidized species, but especially the high binding energy one is attenuated upon longer irradiation.

IrNi_{6.8}/Meso-ATO-OER: Interestingly, this sample is less affected by broadening than Ox-IrNi_{6.8}/Meso-ATO. We find surprisingly high metallic Ir contribution, but notice that the peak even at 210 eV is quite broad (compare to PA-IrNi_{6.8}/Meso-ATO). Irrespective of the fit parameter constraints, we have a significant amount of metallic Ir in this sample. The long beam exposure spectrum suggests again beam sensitivity of the oxidized species.

Lower ratio of signal to noise in XPS Ni 2p of IrNi_{3.3}/Meso-ATO-OER and IrNi_{6.8}/Meso-ATO-OER suggests further leaching of Ni (**Figure 65**). In IrNi_{3.3}/Meso-ATO-OER metallic Ni is further attenuated while somewhat larger metallic Ni is observed in IrNi_{6.8}/Meso-ATO-OER, showing small amount of metallic Ni remains in the alloy phase.

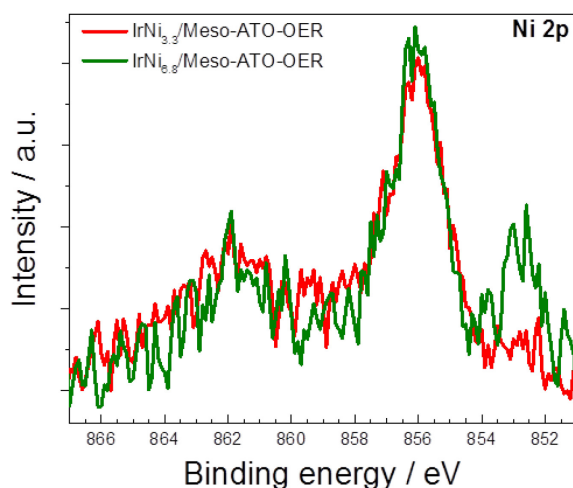


Figure 65. Ni 2p XPS comparison of samples after OER (IrNi_{3.3}/Meso-ATO-OER and IrNi_{6.8}/Meso-ATO-OER). All Ni 2p spectra are area normalized.

Quantitative XPS results of OER-treated IrNi_x/Meso-ATO ($x = 3.3$ and 6.7) show that upon OER testing, Ni was further leached out (**Table 13**).

Table 13. Quantitative XPS results of OER treated IrNi_x/Meso-ATO samples. KE: 550 eV. Molar ratios are shown.

Samples	Ni/Ir	Ir/(Sb+Sn)	Sb/Sn	O/(Ir+Ni+Sb+Sn)
IrNi _{3.3} /Meso-ATO-OER	0.3	0.1	0.045	2.0
IrNi _{6.8} /Meso-ATO-OER	0.2	0.14	0.045	1.9

The surface Sb/Sn ratio further decreased, thus antimony, at least to a certain degree, is not stable during electrochemistry. Concerning stability of the oxide support as well as dispersion of alloyed nanoparticles on support materials, further investigation is necessary.

7.3. Oxygen evolution reaction activities of the oxidized IrNi_x nanoparticles correlated to Ni content in the corresponding precursor alloys

Oxygen evolution reaction activities of Ox-IrNi_x/Meso-ATO samples were tested in highly acidic electrolyte environment using a cyclic voltammetry protocol (see section 2.3.3). Linear sweep voltammetry (iR corrected) and Ir-based mass activity at 300 mV overpotential (iR and capacitance corrected) as a function of the initial Ni content in the corresponding precursor alloys of all samples are presented in **Figure 66** with pure electrochemically oxidized IrO_x/Meso-ATO as a benchmark.

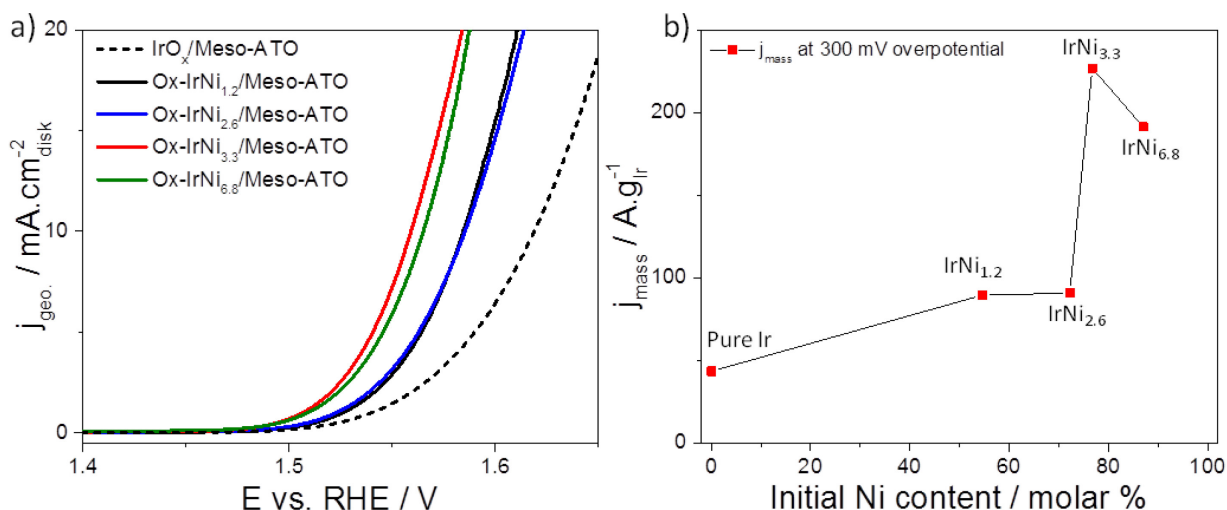


Figure 66. a) Electrocatalytic oxygen evolution reaction (OER) activities of mesoporous ATO supported oxidized IrNi_x core-shell nanoparticles (Ox-IrNi_x/Meso-ATO) prepared from precursor alloy IrNi_x/Meso-ATO, and pure oxidized IrO_x nanoparticles (IrO_x/Meso-ATO, Pure Ir) measured using linear sweep voltammetry, b) Ir-mass based activity at $\eta=300\text{mV}$ overpotential of IrO_x/Meso-ATO, and Ox-IrNi_x/Meso-ATO as a function of the initial Ni content in the corresponding precursor alloy. Measurement conditions: 25 °C, 0.05M H₂SO₄, 1600 rpm. The loading of Ir was 10.2 $\mu\text{g cm}^{-2}$.

Ni-containing samples show clearly higher OER activity compared to pure IrO_x/Meso-ATO, especially for Ni-rich samples (IrNi_{3.3} and IrNi_{6.8}). At 300 mV overpotential, Ox-IrNi_{3.3}/Meso-ATO shows ~5.2 fold of enhancement in mass activity compared to pure IrO_x/Meso-ATO. This implies a 5.2x times higher electrolyzer hydrogen output at the constant voltage. Interestingly, Ox-IrNi_{3.3}/Meso-ATO shows

~ 2.5 fold of enhancement in mass activity at 300 mV overpotential compared to Ox-IrNi_{2.6}/Meso-ATO, although the Ni content in corresponding precursors are not much different. The OER activity of Ox-IrNi_{6.8}/Meso-ATO is, however, only slightly less than that of Ox-IrNi_{3.3}/Meso-ATO. A similar trend was observed for IrNi_x/C with different Ni content in precursor alloys, where DO-IrNi_{3.3} showed ~ 2 times higher mass activity at 250 mV compared to DO-IrNi_{2.3}, but not much higher than DO-IrNi_{5.7} (see chapter 4).

While we are aware that the values in **Figure 61** likely represent an upper bound of the active OER sites, we used them to calculate charge-based specific activity, equivalent to lower bounds of the OER activity (**Figure 67**). All Ni-containing samples show higher specific activity than pure IrO_x/Meso-ATO. The Ox-IrNi_x/Meso-ATO samples show quite similar specific activities, although the Ni content in the precursor alloys varied from 72.2 to 87.2 molar %, the most active sample is Ox-IrNi_{3.3}/Meso-ATO. The enhancement remains below the mass-based value. This is explained by the fact that ECSA of Ni-containing samples are higher than pure IrO_x/Meso-ATO and the charge is an upper bound, rendering the specific activities a lower bound of actual OER rate. Ox-IrNi_x/Meso-ATO samples show ca. 2 to 2.3 fold of enhancement in specific activity compared to pure IrO_x/Meso-ATO. This confirms the positive effect of Ni on OER activity of IrNi alloy nanoparticles.

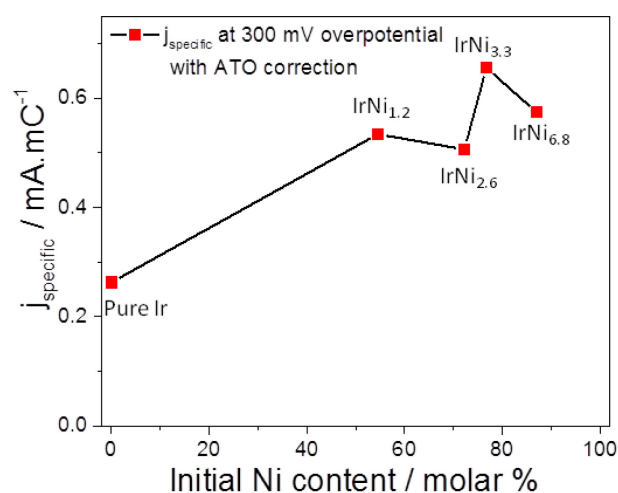


Figure 67. Specific activities (j_{specific}) at 300 mV overpotential of electrochemically oxidized IrNi_x nanoparticles supported on mesoporous ATO as a function of the initial Ni content in the corresponding precursor alloy.

If we compare the surface Ni/Ir ratios of the Ox-IrNi_x/Meso-ATO (**Table 12**), there is no direct correlation with the specific OER activity, similar to IrNi_x supported on

carbon (chapter 4). In order to explain the enhanced specific OER activity of the Ox-IrNi_x/Meso-ATO, we recall that after oxidation, lattice parameter of IrNiO_x/ATO (prepared from PA-IrNi_{3.1}/ATO) remained mostly unchanged compared to that of the precursor alloy, which helped to improve specific OER activity of the core-shell catalyst due to strain effect (see chapter 6). Similarly, electrochemical oxidation removed Ni from surface of IrNi_x nanoparticles in Ox-IrNi_x/Meso-ATO, but might not change the lattice contraction which was obtained in the precursor alloys, thereby, improve the OER activity. In fact, lattice parameters of PA-IrNi_x/Meso-ATO samples evaluated from $d_{(111)}$ (**Figure 57a**) are in range of 3.62 to 3.69 Å, much contracted compared to that of pure Ir (3.84 Å). This might explain for the similar high specific activity of Ox-IrNi_x/Meso-ATO samples but much higher than that of pure IrO_x/Meso-ATO.

In order to highlight the importance of the oxide support compare to carbon support for OER, OER stability tests at a current density of 1 mA cm⁻² of IrNi@IrO_x core-shell nanoparticles supported on carbon and Meso-ATO and pure IrO_x/C were compared in **Figure 68**.

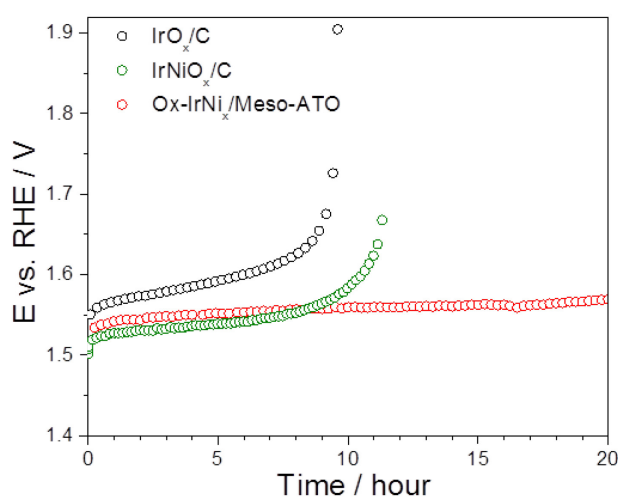


Figure 68. Stability tests at a current density of 1 mA cm⁻² of electrochemical oxidized IrNi_x core-shell nanoparticles supported on carbon and mesoporous antimony doped tin oxide (referred to as IrNiO_x/C and Ox-IrNi_x/Meso-ATO, respectively) compared to pure IrO_x supported on carbon (referred to as IrO_x/C). Measurement conditions: 25 °C, 0.05M H₂SO₄, 1600 rpm. The loading of Ir was 10.2 μg cm⁻².

Pure IrO_x/C showed the least OER activity (highest overpotential) and was the most unstable catalysts among the tested ones. It was completely degraded after about 9 hours of the stability test. IrNiO_x/C showed the best OER activity at the beginning of

the stability test with the lowest overpotential; however was the next catalyst to degrade, after about 12 hours. The most stable catalyst was Ox-IrNi_x/Meso-ATO, which combined high activity of the core-shell nanoparticles with stability of the Meso-ATO, evidencing the beneficial employment of the stable support material.

7.4. Summary

Using the optimized polyol method that was developed in chapter 3, the oxide supported IrNi_x nanoparticles were successfully synthesized with wide range of Ni content, from Ir-rich nanoparticles to Ni-rich nanoparticles without any big deviation from nominal compositions. All as-prepared samples were quite homogeneous nanoparticle alloys with the surface slightly enriched with Ni due to the annealing step in synthetic air during the synthesis process.

After electrochemical pretreatment, Ni was largely removed to form the Ir-rich surfaces. As observed previously with other ATO supported samples, Ir in IrNi_x/Meso-ATO samples underwent struggling oxidation during electrochemical treatment.

The Ir-mass based OER activity of the Ni-containing nanoparticles enhanced significantly compared to the pure Ir nanoparticles supported on the same Meso-ATO due to the high active surface area and the higher specific activity, which might be resulted from the strain effect due to the lattice contraction. The most active catalysts, Ox-IrNi_{3.3}/Meso-ATO showed 5.2 fold of enhancement in Ir-mass based activity and 2.3 fold of enhancement in specific activity at 300 mV overpotential compared to pure IrO_x/Meso-ATO.

8. Conclusions and Perspectives

8.1. Conclusions

The synthetic conditions of the polyol method were optimized for synthesis of IrNi nanoparticle alloys with controlled compositions and metal loadings, starting from Ir : Ni of 1 : 3 then extend to other (1 : 2, 1 : 5, etc) molar ratios. The obtained nanoparticles were quite homogeneous and small alloys with very small deviation from nominal compositions.

A family of dealloyed metal-oxide hybrid IrNi@IrO_x core@shell nanoparticles supported on carbon was presented. It was demonstrated that this structural and compositional class of nanocatalysts offers substantial advances in terms of more efficient and less expensive electrolytic water splitting for acid electrolyzer applications. We followed the evolution of the IrNi@IrO_x metal oxide core-shell particles and confirmed the structure hypothesis step-by-step from their IrNi bimetallic precursor stage, through the metallic core-shell stage to the final oxide shell/ alloy core architecture, using extensive microscopic and spectroscopic analysis. The final catalysts have a nanometer scale almost pure IrO_x surface, while the inner core region became increasingly metallic and richer in Ni. Correlating the structural characteristics with OER activity we concluded that the core-shell catalysts perform substantially more active (about 3x higher compared to electrochemically oxidized Ir, and 10x higher compared to rutile-type IrO₂) and thus thermodynamically more efficient on a noble metal mass and an active site basis during the electrocatalytic oxygen evolution.

Continuing studies toward highly active and stable OER catalysts, a novel catalyst/support couple concept was presented, which involved an electrochemically dealloyed IrNi core-IrO_x shell concept from the previous study combined with a mesoporous corrosion-resistant oxide support for highly efficient and stable OER catalysts in acidic medium. This concept builds upon the formation of an oxidized Ir shell that provided excellent OER activity at low noble metal content and the high surface area mesoporous structure of the support enabled the dispersion of the active nanoparticles, as well as provided high corrosive resistance for the catalysts. The IrNiO_x/Meso-ATO-180 core-shell water splitting catalyst supported a 2.5 times higher oxygen, and correspondingly higher hydrogen evolution rate on the

electrolyzer level, while showing negligible degradation during a 20 hour stability test unlike various Ir benchmark materials. The nanostructured core-shell catalyst/mesoporous support couples could serve as suitable coatings in realistic PEM electrolyzer anodes. Beyond their practical deployment, the presented core-shell catalyst/oxide support concept represents a quite general strategy to reduce the amount of scarce elements in catalytic nanoparticles, and could be transferred to other precious metal based oxides in the future.

For supported nanoparticle OER catalysts, not only the IrNi active phase, but also the support materials play an important role in OER activity and stability. The structure evolution of the nanoparticles under different electrochemical pretreatments was investigated and the influences of the support materials were compared. In general, the nanoparticles were not “excessively” oxidized or dealloyed in the bulk, but only on surface, suggesting that core-shell structure was formed. When supported on carbon, the alloyed nanoparticles underwent stronger structure changes because large amount of Ni was removed during electrochemical treatments, while ATO supported nanoparticles showed very little changes and Ni remained more in the nanoparticles. We found that electrochemical pretreatment played a crucial role in order to realize high OER activity of ATO supported IrNi@IrO_x nanoparticles. The IrNi_x/ATO needs to be treated at high potential before oxidation step in order to protect ATO from destruction process, while dealloying at lower potentials (from 0.05V to 0.8V) lead to destruction of ATO and show strongly negative effect on OER activity. Combined with earlier findings that OER specific activity is uncorrelated with Ni/Ir ratio, we proposed that enhanced OER activity in Ni-containing IrNi@IrO_x core-shell nanoparticles resulted from strain effect due to the lattice contraction remained largely after electrochemical pretreatments.

The evolution of IrO_x shells after different cycles of electrochemical oxidation was studied. When supported on carbon, Ir was feasible oxidized, increasing number of oxidation cycles resulted in higher oxidation degree of Ir, even in the bulk, whereas when supported on ATO, only few surface layers were oxidized and increasing number of oxidation cycles did not lead to further oxidation of Ir. Correlated the oxidized degree of the IrO_x surface with the OER activities, it was suggested that OER happened mainly on surface IrO_x, since oxidation of Ir in the bulk show no effect on OER activity. XPS studies clearly showed that ATO impedes the oxidation of Ir

and Ni leaching. Antimony is not very stable under electrochemical treatment, which might lower the electrical conductivity of the support, leading to degradation in OER activity. The degradation mechanism of the supported core-shell nanoparticles needs to be further investigated.

Using the optimized polyol method, the oxide supported IrNi_x nanoparticles were successfully synthesized with tunable Ni content, from Ir-rich nanoparticles to Ni-rich nanoparticles with only small deviation from the nominal compositions. All as-prepared samples were quite homogeneous nanoparticle alloys with surface slightly enriched by Ni. After electrochemical pretreatment, Ni was largely removed to form Ir-rich surfaces. As observed previously with other ATO supported samples, Ir in IrNi_x/Meso-ATO samples underwent struggling oxidation during electrochemical treatment. Ir-mass based OER activities of Ox-IrNi_x/Meso-ATO samples enhanced significantly compared to pure Ir nanoparticles supported on the same Meso-ATO. The enhanced OER activities were resulted from the high active surface areas and the higher specific activities, while the improvement in the specific activities most probably comes from strain effect. The most active catalysts, Ox-IrNi_{3.3}/Meso-ATO showed 5.2 fold of enhancement in Ir-mass based activity at 300 mV overpotential compared to pure IrO_x/Meso-ATO, implying 5.2x times higher hydrogen output at a constant voltage.

8.2. Perspectives

OER activity degradation of the supported catalysts can be resulted from dissolution of active component (here is Ir), from dissolution or destruction of the support, from passivation of the surface, etc. Mechanism of activity degradation needs to be uncovered, from which stability of OER catalysts can be further improved.

Structure changes under OER condition related to OER mechanism are interesting aspects. With our in-situ electrochemical cell, it is possible to apply in-situ XANES and EXAFS to follow structure evolution of catalytically active elements and study OER mechanism under real OER conditions.

Furthermore, in order to test the catalysts under conditions similar to PEM electrolyzers, we would like to apply IrNi core-shell catalysts in membrane electrode assembly (MEA) electrolyzers. The high OER activity and stability of the IrNi@IrO_x catalysts were established by RDE technique in the present work: however, the

replication and maintenance of OER activities in the single MEA electrolyzers are great challenges. Therefore, the further step is to transfer the core-shell catalysts to MEA and study the activity and long-term stability of the catalysts in the real electrolyzer stack under operating conditions.

List of references

Figure 2. was reprinted from *Electrochimica Acta*, Vol 29, Trasatti, S., Electrocatalysis in the anodic evolution of oxygen and chlorine, 1503-1512, Copyright (1984), with permission from Elsevier.

Figure 3. was reprinted from *Journal of Electroanalytical Chemistry*, Vol 607, Rossmeisl, J., Qu, Z.W., Zhu, H., Kroes, G.-J., Norskov, J.K., Electrolysis of water on oxide surfaces, 83 – 89, Copyright (2007), with permission from Elsevier.

The theoretical part of XRD in section 2.2.1 was written based on *Diffraction and Extended X-Ray Absorption Fine Structure (EXAFS)*, J. W. Niemantsverdriet, with permission from John Wiley and Sons.

The theoretical part of XPS and the **Figure 6** in section 2.2.5 was written based on *Photoemission and Auger Spectroscopy*, J. W. Niemantsverdriet, with permission from John Wiley and Sons.

The synthesis procedure in section 2.1.1 was written based on the publication from Hyung-Suk Oh, Hong Nhan Nong, Peter Strasser, Titel “Preparation of Mesoporous Sb-, F-, and In-Doped SnO₂ Bulk Powder with High Surface Area for Use as Catalyst Supports in Electrolytic Cells”, *Advanced Functional Materials*, Vol. 25, 7, 1074-1081, (2015), with permission of John Wiley and Sons.

Chapter 4 was written based on the publication from Hong Nhan Nong, Lin Gan, Elena Willinger, Detre Teschner, Peter Strasser, Title “IrO_x core-shell nanocatalysts for cost- and energy-efficient electrochemical water splitting”, *Chemical Science*, Vol. 5, 8, 2955-2963, (2014), with permission of Royal Society of Chemistry.

Chapter 5 was written based on the publication from Hong Nhan Nong, Hyung-Suk Oh, Tobias Reier, Elena Willinger, Marc-Georg Willinger, Valeri Petkov, Detre Teschner, Peter Strasser, Title “Oxide-Supported IrNiO_x Core–Shell Particles as Efficient, Cost-Effective, and Stable Catalysts for Electrochemical Water Splitting”, *Angewandte Chemie*, Vol. 127, 10, 3018-3022, (2015), with permission of John Wiley and Sons.

List of publications during PhD

1. Hong Nhan Nong, Hyung-Suk Oh, Tobias Reier, Elena Willinger, Marc-Georg Willinger, Valeri Petkov, Detre Teschner, Peter Strasser, Oxide-Supported IrNiO_x Core–Shell Particles as Efficient, Cost-Effective, and Stable Catalysts for Electrochemical Water Splitting, *Angewandte Chemie*, Vol. 127, 10, 3018-3022, **(2015)**.
2. Hyung-Suk Oh, Hong Nhan Nong, Peter Strasser, Preparation of Mesoporous Sb-, F-, and In-Doped SnO₂ Bulk Powder with High Surface Area for Use as Catalyst Supports in Electrolytic Cells, *Advanced Functional Materials*, Vol. 25, 7, 1074-1081, **(2015)**.
3. Hyung-Suk Oh, Hong Nhan Nong, Tobias Reier, Manuel Gleich, Peter Strasser, Oxide-supported Ir nanodendrites with high activity and durability for the oxygen evolution reaction in acid PEM water electrolyzers, *Chemical Science*, Vol. 6, 6, 3321-3328, **(2015)**.
4. Hong Nhan Nong, Lin Gan, Elena Willinger, Detre Teschner, Peter Strasser, IrO_x core-shell nanocatalysts for cost- and energy-efficient electrochemical water splitting, *Chemical Science*, Vol. 5, 8, 2955-2963, **(2014)**.
5. Tobias Reier, Zarina Pawolek, Serhiy Cherevko, Michael Bruns, Travis Jones, Detre Teschner, Soeren Selve, Arno Bergmann, Hong Nhan Nong, Robert Schlögl, Karl J.J. Mayrhofer, and Peter Strasser, Molecular insight in structure and activity of highly efficient, low-Ir Ir-Ni oxide catalysts for electrochemical water splitting (OER), *J. Am. Chem. Soc.*, 137 (40), 13031–13040, **(2015)**.

Bibliography

- (1) <http://www.iea.org/publications/freepublications/publication/keyworld2014.pdf>, Key World Energy Statistics, **2014**.
- (2) <https://yearbook.enerdata.net/#renewable-in-electricity-production-share-by-region.html>, Global Energy Statistical Yearbook 2015, **2015**.
- (3) <http://www.bmwi.de/English/Redaktion/Pdf/germanys-new-energy-policy>, Germany's new energy policy. Special Brochure Spotlight on Economic Policy, **2012**.
- (4) Fabbri, E.; Habereeder, A.; Waltar, K.; Kotz, R.; Schmidt, T. J. *Catal. Sci. Technol.* **2014**, *4*, 3800.
- (5) Sathre, R.; Scown, C. D.; Morrow, W. R.; Stevens, J. C.; Sharp, I. D.; Ager, J. W.; Walczak, K.; Houle, F. A.; Greenblatt, J. B. *Energy Environ. Sci.* **2014**, *7*, 3264.
- (6) Ball, M.; Wietschel, M. *Int. J. Hydrogen Energy* **2009**, *34*, 615.
- (7) *Chemical Energy Storage*; Schloeg, R., Ed.; De Gruyter: Berlin, **2013**.
- (8) Forgie, R.; Bugosh, G.; Neyerlin, K. C.; Liu, Z. C.; Strasser, P. *Electrochem. Solid State Lett.* **2010**, *13*, D36.
- (9) Reier, T.; Oezaslan, M.; Strasser, P. *ACS Catal.* **2012**, *2*, 1765.
- (10) Bergmann, A.; Zaharieva, I.; Dau, H.; Strasser, P. *Energy Environ. Sci.* **2013**, *6*, 2745.
- (11) Neyerlin, K. C.; Bugosh, G.; Forgie, R.; Liu, Z.; Strasser, P. *J. Electrochem. Soc.* **2009**, *156*, B363.
- (12) Dau, H.; Limberg, C.; Reier, T.; Risch, M.; Roggan, S.; Strasser, P. *Chemcatchem* **2010**, *2*, 724.
- (13) Carmo, M.; Fritz, D. L.; Mergel, J.; Stolten, D. *Int. J. Hydrogen Energy* **2013**, *38*, 4901.
- (14) Smolinka T; Guenther M; J., G. *Stand und Entwicklungspotenzial der Wasserelektrolyse zur Herstellung von Wasserstoff aus regenerativen Energien*, **2011**.
- (15) Hoare, J. P. *The Electrochemistry of Oxygen*; Wiley New York, **1968**.
- (16) Gileadi, E. *Electrode Kinetics for Chemists, Chemical Engineers, and Materials Scientists*; Wiley-VCH, Inc., **1993**.
- (17) Wen, T. C.; Hu, C. C. *J. Electrochem. Soc.* **1992**, *139*, 2158.
- (18) Kuznetsov, V. V.; Chepeleva, S. A.; Gol'din, M. M.; Kudryavtsev, V. N.; Fateev, V. N.; Volkov, A. G. *Russ. J. Electrochem.* **2005**, *41*, 933.
- (19) Ma, H.; Liu, C.; Liao, J.; Su, Y.; Xue, X.; Xing, W. *J. Mol. Catal. A: Chem.* **2006**, *247*, 7.
- (20) Marshall, A.; Børresen, B.; Hagen, G.; Sunde, S.; Tsytkin, M.; Tunold, R. *Russ. J. Electrochem.* **2006**, *42*, 1134.
- (21) Marshall, A.; Børresen, B.; Hagen, G.; Tsytkin, M.; Tunold, R. *Electrochim. Acta* **2006**, *51*, 3161.
- (22) Panić, V. V.; Dekanski, A. B.; Milonjić, S. K.; Mišković-Stanković, V. B.; Nikolić, B. Ž. *Russ. J. Electrochem.* **2006**, *42*, 1055.
- (23) Kanan, M. W.; Nocera, D. G. *Science* **2008**, *321*, 1072.
- (24) Kanan, M. W.; Surendranath, Y.; Nocera, D. G. *Chem. Soc. Rev.* **2009**, *38*, 109.
- (25) Lutterman, D. A.; Surendranath, Y.; Nocera, D. G. *J. Am. Chem. Soc.* **2009**, *131*, 3838.
- (26) Surendranath, Y.; Dincă, M.; Nocera, D. G. *J. Am. Chem. Soc.* **2009**, *131*, 2615.
- (27) Trasatti, S. *Electrochim. Acta* **1984**, *29*, 1503.
- (28) Bockris, J. O.; Otagawa, T. *J. Phys. Chem.* **1983**, *87*, 2960.
- (29) Bockris, J. O. M.; Otagawa, T. *J. Electrochem. Soc.* **1984**, *131*, 290.
- (30) Beer, H. B. United States, **1972**; Vol. 3,632,498.
- (31) Beer, H. B. United States, **1973**; Vol. 3, 711, 385.
- (32) Ma, L.; Sui, S.; Zhai, Y. *Int. J. Hydrogen Energy* **2009**, *34*, 678.
- (33) Millet, P.; Ngameni, R.; Grigoriev, S. A.; Mbemba, N.; Brisset, F.; Ranjbari, A.; Etievant, C. *Int. J. Hydrogen Energy* **2010**, *35*, 5043.
- (34) Millet, P.; Mbemba, N.; Grigoriev, S. A.; Fateev, V. N.; Aukauloo, A.; Etiévant, C. *Int. J. Hydrogen Energy* **2011**, *36*, 4134.
- (35) Song, S.; Zhang, H.; Ma, X.; Shao, Z.; Baker, R. T.; Yi, B. *Int. J. Hydrogen Energy* **2008**, *33*, 4955.
- (36) Lodi, G.; Sivieri, E.; De Battisti, A.; Trasatti, S. *J. Appl. Electrochem.* **1978**, *8*, 135.
- (37) Castelli, P.; Trasatti, S.; Pollak, F. H.; O'Grady, W. E. *J. Electroanal. Chem.* **1986**, *210*, 189.
- (38) Fierro, S.; Nagel, T.; Baltruschat, H.; Comninellis, C. *Electrochem. Commun.* **2007**, *9*, 1969.
- (39) Gaudet, J.; Tavares, A. C.; Trasatti, S.; Guay, D. *Chem. Mater.* **2005**, *17*, 1570.

- (40) De Pauli, C. P.; Trasatti, S. *J. Electroanal. Chem.* **2002**, 538–539, 145.
- (41) Trasatti, S. *Electrochim. Acta* **2000**, 45, 2377.
- (42) De Faria, L. A.; Boodts, J. F. C.; Trasatti, S. *Colloids and Surfaces A: Physicochem. Eng. Aspects* **1998**, 132, 53.
- (43) De Pauli, C. P.; Trasatti, S. *J. Electroanal. Chem.* **1995**, 396, 161.
- (44) Bockris, J. O. M.; Otagawa, T.; Young, V. *J. Electroanal. Chem.* **1983**, 150, 633.
- (45) Mehandru, S. P.; Anderson, A. B. *J. Electrochem. Soc.* **1989**, 136, 158.
- (46) Bockris, J. O. M. *J. Chem. Phys.* **1956**, 24, 817.
- (47) Krasilshchikov, A. I. *Zh. Fiz. Khim.* **1963**, 37, 531.
- (48) Damjanovic, A.; Dey, A.; Bockris, J. O. M. *Electrochim. Acta* **1966**, 11, 791.
- (49) Rüetschi, P.; Delahay, P. *J. Chem. Phys.* **1955**, 23, 556.
- (50) *Chemical Bonding at Surfaces and Interfaces*; Nilsson, A.; Pettersson, L.; Norskov, J., Eds.; Elsevier Science: Amsterdam, **2008**.
- (51) Nørskov, J. K.; Rossmeisl, J.; Logadottir, A.; Lindqvist, L.; Kitchin, J. R.; Bligaard, T.; Jónsson, H. *J. Phys. Chem. B* **2004**, 108, 17886.
- (52) Greeley, J.; Norskov, J. K.; Mavrikakis, M. *Annu. Rev. Phys. Chem.* **2002**, 53, 319.
- (53) Hammer, B.; Nørskov, J. K. In *Advances in Catalysis*; Bruce C. Gates, H. K., Ed.; Academic Press: **2000**; Vol. Volume 45, p 71.
- (54) Norskov, J. K.; Bligaard, T.; Rossmeisl, J.; Christensen, C. H. *Nat. Chem.* **2009**, 1, 37.
- (55) Hammer, B.; Nørskov, J. K. *Surf. Sci.* **1995**, 343, 211.
- (56) Strasser, P.; Koh, S.; Anniyev, T.; Greeley, J.; More, K.; Yu, C.; Liu, Z.; Kaya, S.; Nordlund, D.; Ogasawara, H.; Toney, M. F.; Nilsson, A. *Nat. Chem.* **2010**, 2, 454.
- (57) Man, I. C.; Su, H.-Y.; Calle-Vallejo, F.; Hansen, H. A.; Martínez, J. I.; Inoglu, N. G.; Kitchin, J.; Jaramillo, T. F.; Nørskov, J. K.; Rossmeisl, J. *Chemcatchem* **2011**, 3, 1159.
- (58) Rossmeisl, J.; Qu, Z. W.; Zhu, H.; Kroes, G. J.; Nørskov, J. K. *J. Electroanal. Chem.* **2007**, 607, 83.
- (59) Rossmeisl, J.; Dimitrievski, K.; Siegbahn, P.; Nørskov, J. K. *J. Phys. Chem. C* **2007**, 111, 18821.
- (60) Rossmeisl, J.; Logadottir, A.; Nørskov, J. K. *Chem. Phys.* **2005**, 319, 178.
- (61) Halck, N. B.; Petrykin, V.; Krtil, P.; Rossmeisl, J. *Phys. Chem. Chem. Phys.* **2014**, 16, 13682.
- (62) Hutchings, R.; Muller, K.; Kotz; Stucki, S. *J. Mater. Sci.* **1984**, 19, 3987.
- (63) Kötzt, R.; Stucki, S. *Electrochim. Acta* **1986**, 31, 1311.
- (64) Chen, G.; Chen, X.; Yue, P. L. *J. Phys. Chem. B* **2002**, 106, 4364.
- (65) Morimitsu, M.; Otagawa, R.; Matsunaga, M. *Electrochim. Acta* **2000**, 46, 401.
- (66) Terezo, A. J.; Bisquert, J.; Pereira, E. C.; Garcia-Belmonte, G. *J. Electroanal. Chem.* **2001**, 508, 59.
- (67) Lassali, T. A. F.; Boodts, J. F. C.; Bulhões, L. O. S. *Electrochim. Acta* **1999**, 44, 4203.
- (68) Zhang, J.-J.; Hu, J.-M.; Zhang, J.-Q.; Cao, C.-N. *Int. J. Hydrogen Energy* **2011**, 36, 5218.
- (69) Antolini, E. *ACS Catal.* **2014**, 4, 1426.
- (70) Ardizzone, S.; Bianchi, C. L.; Cappelletti, G.; Ionita, M.; Minguzzi, A.; Rondinini, S.; Vertova, A. *J. Electroanal. Chem.* **2006**, 589, 160.
- (71) Lee, Y.; Suntivich, J.; May, K. J.; Perry, E. E.; Shao-Horn, Y. *J. Phys. Chem. Lett.* **2012**, 3, 399.
- (72) Oh, H.-S.; Nong, H. N.; Reier, T.; Gliech, M.; Strasser, P. *Chem. Sci.* **2015**, 6, 3321.
- (73) Nakagawa, T.; Beasley, C. A.; Murray, R. W. *J. Phys. Chem. C* **2009**, 113, 12958.
- (74) Zhao, Y. X.; Hernandez-Pagan, E. A.; Vargas-Barbosa, N. M.; Dysart, J. L.; Mallouk, T. E. *J. Phys. Chem. Lett.* **2011**, 2, 402.
- (75) Marshall, A. T.; Haverkamp, R. G. *J. Mater. Sci.* **2012**, 47, 1135.
- (76) Ortel, E.; Reier, T.; Strasser, P.; Kraehnert, R. *Chem. Mater.* **2011**, 23, 3201.
- (77) Greeley, J.; Stephens, I. E. L.; Bondarenko, A. S.; Johansson, T. P.; Hansen, H. A.; Jaramillo, T. F.; Rossmeisl, J.; Chorkendorff, I.; Nørskov, J. K. *Nat. Chem.* **2009**, 1, 552.
- (78) Strasser, P.; Koh, S.; Greeley, J. *Phys. Chem. Chem. Phys.* **2008**, 10, 3670.
- (79) Ferrin, P.; Nilekar, A. U.; Greeley, J.; Mavrikakis, M.; Rossmeisl, J. *Surf. Sci.* **2008**, 602, 3424.
- (80) Stamenkovic, V.; Mun, B. S.; Mayrhofer, K. J. J.; Ross, P. N.; Markovic, N. M.; Rossmeisl, J.; Greeley, J.; Nørskov, J. K. *Angew. Chem. Int. Ed.* **2006**, 45, 2897.
- (81) Greeley, J.; Nørskov, J. K.; Kibler, L. A.; El-Aziz, A. M.; Kolb, D. M. *ChemPhysChem* **2006**, 7, 1032.

- (82) Greeley, J.; Jaramillo, T. F.; Bonde, J.; Chorkendorff, I.; Norskov, J. K. *Nat. Mater.* **2006**, *5*, 909.
- (83) Andersson, M. P.; Bligaard, T.; Kustov, A.; Larsen, K. E.; Greeley, J.; Johannessen, T.; Christensen, C. H.; Nørskov, J. K. *J. Catal.* **2006**, *239*, 501.
- (84) Greeley, J.; Nørskov, J. K. *Surf. Sci.* **2005**, *592*, 104.
- (85) Greeley, J.; Mavrikakis, M. *Nat. Mater.* **2004**, *3*, 810.
- (86) Gan, L.; Heggen, M.; Rudi, S.; Strasser, P. *Nano Lett.* **2012**, *12*, 5423.
- (87) Niemantsverdriet, J. W. In *Spectroscopy in Catalysis*; Wiley-VCH Verlag GmbH & Co. KGaA: **2007**, p 147.
- (88) Niemantsverdriet, J. W. In *Spectroscopy in Catalysis*; Wiley-VCH Verlag GmbH & Co. KGaA: **2007**, p 39.
- (89) Knop-Gericke, A.; Kleimenov, E.; Hävecker, M.; Blume, R.; Teschner, D.; Zafeirotos, S.; Schlögl, R.; Bukhtiyarov, V. I.; Kaichev, V. V.; Prosvirin, I. P.; Nizovskii, A. I.; Bluhm, H.; Barinov, A.; Dudin, P.; Kiskinova, M. In *Advances in Catalysis*; Bruce, C. G., Helmut, K., Eds.; Academic Press: **2009**; Vol. Volume 52, p 213.
- (90) Yeh, J. J.; Lindau, I. *At. Data Nucl. Data Tables* **1985**, *32*, 1.
- (91) Petkov, V. *Mater. Today* **2008**, *11*, 28.
- (92) Woods, R. *J. Electroanal. Chem.* **1974**, *49*, 217.
- (93) Sun, S. H.; Murray, C. B.; Weller, D.; Folks, L.; Moser, A. *Science* **2000**, *287*, 1989.
- (94) Ahrenstorf, K.; Albrecht, O.; Heller, H.; Kornowski, A.; Görlitz, D.; Weller, H. *Small* **2007**, *3*, 271.
- (95) Rudi, S.; Tuaeov, X.; Strasser, P. *Electrocatalysis* **2012**, *3*, 265.
- (96) Nong, H. N.; Gan, L.; Willinger, E.; Teschner, D.; Strasser, P. *Chem. Sci.* **2014**, *5*, 2955.
- (97) Baranova, E. A.; Le Page, Y.; Ilin, D.; Bock, C.; MacDougall, B.; Mercier, P. H. J. *J. Alloys Compd.* **2009**, *471*, 387.
- (98) Oezaslan, M.; Heggen, M.; Strasser, P. *J. Am. Chem. Soc.* **2012**, *134*, 514.
- (99) Cui, C. H.; Gan, L.; Li, H. H.; Yu, S. H.; Heggen, M.; Strasser, P. *Nano Lett.* **2012**, *12*, 5885.
- (100) Lassali, T. A. F.; Boodts, J. F. C.; Bulhões, L. O. S. *J. Appl. Electrochem.* **2000**, *30*, 625.
- (101) Alders, D.; Voogt, F. C.; Hibma, T.; Sawatzky, G. A. *Phys. Rev. B* **1996**, *54*, 7716.
- (102) Song, P.; Wen, D.; Guo, Z. X.; Korakianitis, T. *Phys. Chem. Chem. Phys.* **2008**, *10*, 5057.
- (103) Wertheim, G. K.; Guggenheim, H. J. *Phys. Rev. B* **1980**, *22*, 4680.
- (104) Juodkazyte, J.; Sebek, B.; Valsiunas, I.; Juodkazis, K. *Electroanalysis* **2005**, *17*, 947.
- (105) Hu, W.; Wang, Y.; Hu, X.; Zhou, Y.; Chen, S. *J. Mater. Chem.* **2012**, *22*, 6010.
- (106) Nong, H. N.; Oh, H.-S.; Reier, T.; Willinger, E.; Willinger, M.-G.; Petkov, V.; Teschner, D.; Strasser, P. *Angew. Chem.* **2015**, *127*, 3018.
- (107) Oh, H.-S.; Nong, H. N.; Strasser, P. *Adv. Funct. Mater.* **2015**, *25*, 1074.
- (108) Ahmadi, M.; Behafarid, F.; Cui, C.; Strasser, P.; Cuenya, B. R. *ACS Nano* **2013**, *7*, 9195.
- (109) Sanchez Casalongue, H. G.; Ng, M. L.; Kaya, S.; Friebel, D.; Ogasawara, H.; Nilsson, A. *Angew. Chem. Int. Ed.* **2014**, *53*, 7169.
- (110) Gan, L.; Heggen, M.; O'Malley, R.; Theobald, B.; Strasser, P. *Nano Lett.* **2013**, *13*, 1131.
- (111) Snyder, J.; McCue, I.; Livi, K.; Erlebacher, J. *J. Am. Chem. Soc.* **2012**, *134*, 8633.
- (112) Erlebacher, J.; Aziz, M. J.; Karma, A.; Dimitrov, N.; Sieradzki, K. *Nature* **2001**, *410*, 450.
- (113) Erlebacher, J. *J. Electrochem. Soc.* **2004**, *151*, C614.
- (114) Wang, J. X.; Ma, C.; Choi, Y.; Su, D.; Zhu, Y.; Liu, P.; Si, R.; Vukmirovic, M. B.; Zhang, Y.; Adzic, R. R. *J. Am. Chem. Soc.* **2011**, *133*, 13551.
- (115) Fonseca, I. T. E.; Lopes, M. I.; Portela, M. T. C. *J. Electroanal. Chem.* **1996**, *415*, 89.
- (116) Du, W. X.; Wang, Q.; Saxner, D.; Deskins, N. A.; Su, D.; Krzanowski, J. E.; Frenkel, A. I.; Teng, X. W. *J. Am. Chem. Soc.* **2011**, *133*, 15172.
- (117) Savinell, R. F.; Zeller, R. L.; Adams, J. A. *J. Electrochem. Soc.* **1990**, *137*, 489.

Abbreviations

Abbreviation	Definition
CA	Chrono-amperometry
CV	Cyclic voltammetry
D	Dealloyed
DCB	1,2-dichlorobenzene
DFT	density functional theory
DMA	Dimethylacetamide
DO	directly oxidized
DSA	dimensionally stable anode
ECSA	Electrochemically active surface area
EDX	energy dispersive X-ray spectroscopy
EG	ethylene glycol
FFT	fast Fourier transform
GC	glassy carbon
HAADF	High Angle Annular Dark Field
HE XRD	High energy X-ray diffraction
HPDO	High potential directly oxidized
H_{upd}	hydrogen underpotential deposition
ICP-OES	Inductively coupled plasma optical emission spectroscopy
IMP	Impregnation
Ir/C	Ir nanoparticles supported on carbon black Vulcan® XC72, Cabot
Ir/com.-ATO	Ir nanoparticles supported on commercial antimony doped tin oxide, Sigma Aldrich
Ir/Meso-ATO	Ir nanoparticles supported on mesoporous antimony doped tin oxide
IrM@IrO _x	core@shell nanoparticles
IrNiO _x /ATO-20hOER	IrNi@IrO _x nanoparticles supported on mesoporous antimony doped tin oxide treated under OER condition for 20 hours
IrNiO _x /ATO-5hOER	IrNi@IrO _x nanoparticles supported on mesoporous antimony doped tin oxide treated under OER condition for 5 hours

IrNiO _x /ATO-90mOER	IrNi@IrO _x nanoparticles supported on mesoporous antimony treated under OER condition for 90 minutes
IrNiO _x /C-90mOER	IrNi@IrO _x nanoparticles supported on carbon treated under OER condition for 90 hours
IrNiO _x /Meso-ATO-T	IrNi@IrO _x nanoparticles supported on mesoporous antimony doped tin oxide after electrochemical oxidation
IrNi _x /C	IrNi _x nanoparticles supported on carbon black Vulcan® XC72, Cabot
IrNi _x /Meso-ATO-OER	OER treated IrNi _x nanoparticles supported on mesoporous antimony doped tin oxide
IrO _x /C	electrochemical oxidized IrO _x nanoparticles supported on carbon black Vulcan® XC72, Cabot
IrO _x /com.-ATO	electrochemical oxidized IrO _x nanoparticles supported on commercial antimony doped tin oxide, Sigma Aldrich
KE	kinetic energy
MEA	membrane electrode assembly
Meso-ATO	mesoporous antimony doped tin oxide
NMP	N-methyl-2-pyrrolidone
OER	oxygen evolution reaction
Ox-IrNi _x /Meso-ATO	Electrochemical oxidized IrNi _x nanoparticles supported on mesoporous antimony doped tin oxide
PA	precursor alloy
PA-IrNi _x /Meso-ATO	IrNi _x nanoparticles supported on mesoporous antimony doped tin oxide as precursor alloys
PA-IrNi _x /Meso-ATO-T	IrNi _x nanoparticle precursor alloy supported on mesoporous antimony doped tin oxide annealed at temperature T
PDFs	pair distribution functions
PEIS	Potential Electrochemical Impedance Spectroscopy
PEM	polymer electrolyte membrane
PO	Polyol
RDE	rotating disk electrode
rds	rate determining step
RHE	reversible hydrogen electrode

SO	stepwise oxidized
SOECS	solid oxide electrolyzer cells
STEM	Scanning transmission electron microscopy
TDA	Tetradecylamine
TEM	Transmission electron microscopy
UHV	ultra-high vacuum
VB	valence band
XANES	X-ray Absorption Near Edge Structure
XPS	X-ray photoelectron spectroscopy
XRD	X-ray diffraction

List of Figures

- Figure 1.** Percentage of renewable energy in the electricity production of some representative countries in Europe over the past 10 years. Data obtained from Ref. 2. 1
- Figure 2.** Electrocatalytic O₂ evolution activity at various oxide electrodes as a function of the enthalpy change associated with the transition of a lower to a higher oxide state. (Alkaline and (●) acid solutions are indicated. Reprinted from Ref. 27 with permission of Elsevier, copyright (1984). 9
- Figure 3.** The theoretical activity of the four charge transferring steps of oxygen evolution is depicted as function of the oxygen binding energy for a) oxide surfaces, and b) metal surfaces. The y-axis is the activity defined as $-\Delta G_i$ of the different reaction steps, calculated from the linear relations: $\Delta G_1 = \Delta G_{\text{HO}} - \Delta G_{\text{water}} = \Delta E_{\text{HO}} + 0.35 \text{ eV}$, $\Delta G_2 = \Delta G_{\text{O}} - \Delta G_{\text{HO}} = \Delta E_{\text{O}} + 0.05 \text{ eV} - \Delta E_{\text{HO}} - 0.35 \text{ eV}$, $\Delta G_3 = \Delta G_{\text{HOO}} - \Delta G_{\text{O}} = \Delta E_{\text{HOO}} + 0.40 \text{ eV} - \Delta E_{\text{O}} - 0.05 \text{ eV}$, $\Delta G_4 = \Delta G_{\text{O}_2} - \Delta G_{\text{HOO}} = 4.96 \text{ eV} - \Delta E_{\text{HOO}} - 0.40 \text{ eV}$. The resulting volcano is indicated with dash-dot lines and the hatched areas. For the metal surfaces interaction with water has been taken into account, it results in a stabilization of HO and HOO compared to O. For the oxides the interaction with water is small. The best possible material would fall on the horizontal dashed line representing the equilibrium potential 1.23 eV. Optimal oxide catalysts are very close to this value (like RuO₂ and IrO₂). Reprinted from Ref. 58 with permission of Elsevier, copyright (2007). 10
- Figure 4.** a) Volcano curve of the theoretical overpotential for the oxygen evolution process based on DFT calculations described in the literature⁵⁷ using the second charge transfer reaction as a descriptor. The star marks the position of an ideal catalyst, the magenta circle corresponds to Ni modified ruthenia and the blue circle to Co modified ruthenia, b) The correlation between the measured current density obtained at 1.6 V (vs. RHE) and the theoretical overpotential for different oxides. For the mixed oxides a concentration of Ni or Co of 0.05 is chosen to represent the activity per site for the cation modified ruthenia. Reproduced from Ref. 61 with permission of The Royal Society of Chemistry, copyright (2014). 12
- Figure 5.** Schematic visualization of the Bragg equation. 22
- Figure 6.** Photoemission and the Auger process. Left: An incident X-ray photon is absorbed and a photoelectron emitted. Measurement of its kinetic energy allows one to calculate the binding energy of the photoelectron. The atom stays behind as an unstable ion with a hole in one of the core levels. Right: The excited ion relaxes by filling the core hole with an electron from a higher shell. The energy released by this transition is taken up by another electron, the Auger electron, which leaves the sample with an element-specific kinetic energy. In Auger spectroscopy a beam of energetic (2-5 keV) electrons creates the initial core holes. Reproduced from Ref. 88 with permission of John Wiley and Sons, copyright (2007). 24
- Figure 7.** Electrochemical setup. a) counter electrode (Pt mesh), b) reference electrode (Hg/HgSO₄ in saturated K₂SO₄), c) working electrode RDE (thin film of catalyst on glassy carbon), d) rotator, e) and f) gas inlets. 28
- Figure 8.** One duty cycle of the durability test under stepwise load increase. 31
- Figure 9.** a) XRD patterns of IrNi_x/C synthesized by impregnation, polyol, and surfactant free methods (denoted as IrNi_x-IMP, IrNi_x-PO, and IrNi_x-EG, respectively), and b) a zoom in the first two reflections of IrNi_x-IMP and IrNi_x-PO. 37

- Figure 10.** XRD patterns of IrNi_x/C synthesized by the polyol method at 240 °C using different co-solvents: 1,2-dichlorobenzene (DCB), N-methyl-2-pyrrolidone (NMP), dimethylacetamide (DMA), (denoted as IrNi_x-DCB, IrNi_x-NMP, IrNi_x-DMA, respectively). 40
- Figure 11.** TEM images of unsupported IrNi_x nanoparticles with different magnifications (a and b), and carbon supported IrNi_x nanoparticles (c) synthesized by the polyol method with optimized conditions. 41
- Figure 12.** Particle size histograms of a) unsupported IrNi_x nanoparticles, and b) carbon supported IrNi_x nanoparticles synthesized by the polyol method with optimized conditions. 41
- Figure 13.** Synthetic protocol for the preparation of SO-IrNi@IrO_x and DO-IrNi@IrO_x hybrid core-shell nanoparticle catalysts. Precursor IrNi alloys (“PA-IrNi”, and alloy scheme on left, blue: Ni, grey: Ir) are stepwise (SO) or directly (DO) dealloyed and surface oxidized. The “SO-IrNi_x” or “DO-IrNi_x” nomenclatures emphasize the original stoichiometry of the parent precursor alloy, while the “SO-IrNi@IrO_x” and “DO-IrNi@IrO_x” nomenclature stresses the chemical structure of the core-shell particles. Reprinted from Ref. 96 with permission of The Royal Society of Chemistry, copyright (2014). 45
- Figure 14.** a) Powder X-ray diffraction patterns of Ir, IrNi_{2.3}, IrNi_{3.3}, IrNi_{5.7} precursor alloy catalysts; C denotes a support reflection; vertical dashed lines indicate database reflections of pure Ir and pure Ni, and b) relationship between lattice constant and Ni composition (red symbols) compared to Vegard’s rule (dashed line). Reprinted from Ref. 96 with permission of The Royal Society of Chemistry, copyright (2014). 46
- Figure 15.** TEM images and particle size histograms of a) Ir, b) IrNi_{2.3}, c) IrNi_{3.3}, and d) IrNi_{5.7} precursor alloys. Scale bars are 10 nm in a) and b); and are 20 nm in c) and d). Reprinted from Ref. 96 with permission of The Royal Society of Chemistry, copyright (2014). 47
- Figure 16.** a) Voltammetric profiles of the precursor alloy PA-IrNi_x nanoparticles (dashed) and dealloyed D-IrNi_x nanoparticles (solid) in N₂-saturated 0.05 M H₂SO₄ aqueous solution at 20 mV s⁻¹, and b) Comparison of the electrochemically active surface areas (ECSA) of PA-IrNi_x and D-IrNi_x nanoparticles. Reprinted from Ref. 96 with permission of The Royal Society of Chemistry, copyright (2014). 49
- Figure 17.** HAADF-STEM images of a) PA-IrNi_{3.3} and b) D-IrNi_{3.3} nanoparticles. Reprinted from Ref. 96 with permission of The Royal Society of Chemistry, copyright (2014). 50
- Figure 18.** STEM-EDX line profiles of Ir and Ni in a) PA-IrNi_{3.3}, b) and c) D-IrNi_{3.3}. The red arrows in the corresponding nanoparticles (see insets) indicate the directions of the EDX line profiles. Reprinted from Ref. 96 with permission of The Royal Society of Chemistry, copyright (2014). 51
- Figure 19.** (a) Voltammetric surface oxidation D-IrNi_{3.3} catalyst and (b) Ir (III-IV) redox peaks of SO-IrNi_x and DO-IrNi_x. Reprinted from Ref. 96 with permission of The Royal Society of Chemistry, copyright (2014). 52
- Figure 20.** Estimated molar amount of electrochemically accessible Ir redox sites (active sites) per mg of Ir on electrode of stepwise oxidized (SO-IrNi_x) and directly oxidized (DO-IrNi_x) samples. 52
- Figure 21.** Survey XP spectra of IrNi_{3.3} series: precursor alloy, dealloyed, stepwise oxidized, and directly oxidized IrNi_{3.3} (denoted as PA-, D-, SO-, and DO-IrNi_{3.3}, respectively).

- Reprinted from Ref. 96 with permission of The Royal Society of Chemistry, copyright (2014). 54
- Figure 22.** a) Ir 4f and b) Ni 2p core levels of the IrNi_{2.3} series: precursor alloy (PA-IrNi_{2.3}), stepwise oxidized (SO-IrNi_{2.3}) and directly oxidized (DO-IrNi_{2.3}) samples at kinetic energy 550 eV. Vertical dashed lines indicate peak position of metallic Ir. 55
- Figure 23.** Ir 4f depth profiles of a) stepwise oxidized (SO-IrNi_{2.3}) and b) directly oxidized (DO-IrNi_{2.3}). Vertical dashed lines indicate peak position of metallic Ir. 55
- Figure 24.** C 1s core levels of the IrNi_{2.3} series (precursor alloy (PA-IrNi_{2.3}), stepwise oxidized (SO-IrNi_{2.3}) and directly oxidized (DO-IrNi_{2.3}) samples) at kinetic energy 550 eV. 56
- Figure 25.** a) Ni 2p of precursor alloy (PA-IrNi_{3.3}), dealloyed (D-IrNi_{3.3}), stepwise oxidized (SO-IrNi_{3.3}) and directly oxidized IrNi_{3.3} (DO-IrNi_{3.3}), and b) Ir 4f XP spectra of PA-IrNi_{3.3} and D-IrNi_{3.3} at kinetic energy (KE) of 210 eV and 550 eV. Vertical line in a) marks the core level shift of metallic Ni. Reprinted from Ref. 96 with permission of The Royal Society of Chemistry, copyright (2014). 57
- Figure 26.** a) Ni L-edge XANES of the IrNi_{3.3} series: precursor alloy, dealloyed, stepwise oxidized, and directly oxidized IrNi_{3.3} (denoted as PA-, D-, SO, and DO-IrNi_{3.3}, respectively), and b) a zoom on a tiny shoulder around 859 eV. Reprinted from Ref. 96 with permission of The Royal Society of Chemistry, copyright (2014). 58
- Figure 27.** Ir 4f core level spectra of (a) SO-IrNi_{3.3} and (b) DO-IrNi_{3.3} at KE 210, 550 and 1200 eV. Dashed lines indicate peak position of metallic Ir as found in PA-IrNi_{3.3}. Reprinted from Ref 96 with permission of The Royal Society of Chemistry, copyright (2014). 58
- Figure 28.** a) Ir 4f and b) Ni 2p core levels of the IrNi_{5.7} series (precursor alloy (PA-IrNi_{5.7}), stepwise oxidized (SO-IrNi_{5.7}) and directly oxidized (DO-IrNi_{5.7}) samples) at kinetic energy 550 eV. Vertical dashed lines indicate peak position of metallic Ir. 59
- Figure 29.** Ir 4f depth profile of a) stepwise oxidized (SO-IrNi_{5.7}) and b) directly oxidized (DO-IrNi_{5.7}). Vertical dashed lines indicate peak positions of metallic Ir. 59
- Figure 30.** C 1s core level spectra of the IrNi_{5.7} series (precursor alloy (PA-IrNi_{5.7}), stepwise oxidized (SO-IrNi_{5.7}) and directly oxidized (DO-IrNi_{5.7}) samples) at kinetic energy 550 eV. 60
- Figure 31.** Linear sweep voltammetry as catalytic oxygen evolution reaction (OER) activities of a) stepwise oxidized (SO) IrNi_x and b) directly oxidized (DO) IrNi_x core-shell nanoparticle catalysts, in comparison to pure Ir nanoparticles. c) Ir mass based activities and d) specific activities at 0.25V overpotential. Conditions: 0.05 M H₂SO₄, 1600 rpm, scan rate 5 mV s⁻¹. “r-IrO₂” denotes the Ir-mass based activity of IrO₂ rutile-type nanoparticles at 0.25V overpotential.⁷¹ Reprinted from Ref. 96 with permission of The Royal Society of Chemistry, copyright (2014). 62
- Figure 32.** Chronopotentiometric measurements of pure Ir and directly oxidized (DO) IrNi_{3.3} core-shell nanoparticles at a current density of 1 mA cm⁻². Reprinted from Ref. 96 with permission of The Royal Society of Chemistry, copyright (2014). 63
- Figure 33.** Ir 4f XPS of directly oxidized IrNi_{3.3} at KE 550 eV before (bottom graph, denoted “DO-IrNi_{3.3}”) and after the stability test (top graph, denoted “DO-IrNi_{3.3}-Stabil”) with Ir 4f peak position derived from PA-IrNi_{3.3} at KE 550 eV (dash lines) as standard for the metallic Ir component. Reprinted from Ref. 96 with permission of The Royal Society of Chemistry, copyright (2014). 64

- Figure 34.** TEM images of a) mesoporous antimony doped tin oxide (Meso-ATO), b) Meso-ATO supported $\text{IrNi}_{3.3}$ nanoparticle precursor alloy annealed at 180 °C (PA- $\text{IrNi}_{3.3}$ /Meso-ATO-180), inset: particle size distribution of $\text{IrNi}_{3.3}$ nanoparticles in PA- $\text{IrNi}_{3.3}$ /Meso-ATO-180. Reprinted from Ref. 106 with permission of John Wiley and Sons, copyright (2015). 68
- Figure 35.** XRD patterns of mesoporous antimony doped tin oxide (Meso-ATO) supported IrNi_x precursor alloys annealed at different temperatures T (T is given by each data set), vertical dashed lines indicate (111) database reflections of pure metallic Ir and Ni; open circles and stars indicate database main reflections of NiO and antimony doped tin oxide, respectively. Reprinted from Ref. 106 with permission of John Wiley and Sons, copyright (2015). 69
- Figure 36.** XP spectra of supported IrNi_x precursor alloys annealed at different temperatures T (T is given by each data set). a) Ir 4f Ni 3p XPS, and b) Ni 2p XPS. All spectra were measured at a kinetic energy of 550 eV. Vertical dashed lines indicate peak positions of metallic Ir. Reprinted from Ref. 106 with permission of John Wiley and Sons, copyright (2015). 70
- Figure 37.** Atomic pair distribution functions (PDFs) of supported IrNi_x precursor alloys annealed at different temperatures T (T is given by each data set). a) Experimental atomic PDFs. Radius of first atomic coordination sphere in nanoparticles is given by each data set. Signatures of NiO nanophase appear with samples treated at 300 °C and above (green vertical broken arrows), and the NiO nanophase fully developed in the sample annealed at 500 °C (solid green line represents a fit of NiO nanophase). b) Experimental (symbols) and model (solid lines) atomic PDFs for IrNi_x /Meso-ATO-T. Models feature fcc-type (line in red) metallic alloy and NiO nanophase (line in blue). Refined “fcc-lattice parameters” are given by each data set (in red). Respective fcc model agreement/fit quality factors (R_w) are also given (in %). Reprinted from Ref. 106 with permission of John Wiley and Sons, copyright (2015). 72
- Figure 38.** Depth-resolved Ir 4f-Ni 3p XP spectra of a) PA- $\text{IrNi}_{3.3}$ /Meso-ATO-180 and b) the corresponding IrNiO_x /Meso-ATO-180 OER catalyst after dealloying and oxidation (50 CV cycles, 0.05 - 1.5V). Top to bottom spectra were measured at photoelectron kinetic energies of 210, 550, and 1200 eV. The dash vertical lines indicate peak position of metallic Ir. Note, the broader spectra at higher photon energy are due to the lower resolution of the beamline. Reprinted from Ref. 106 with permission of John Wiley and Sons, copyright (2015). 74
- Figure 39.** a) HRTEM image of $\text{IrNi}_{3.3}$ /Meso-ATO-180 with FFTs (insets) of IrNi_x and Meso-ATO, b) and c) HAADF-STEM images of hollow core-shell (red arrows) and solid core-shell (blue arrows) IrNiO_x /Meso-ATO-180 nanoparticles. Reprinted from Ref. 106 with permission of John Wiley and Sons, copyright (2015). 74
- Figure 40.** a) HAADF-STEM image of the IrNiO_x /Meso-ATO-180 core-shell nanoparticle catalyst synthesized from Meso-ATO supported $\text{IrNi}_{3.3}$ nanoparticle precursor alloy annealed at 180 °C (PA- $\text{IrNi}_{3.3}$ /Meso-ATO-180), b) corresponding elemental mapping. c) d) c, e) f) corresponding elemental mappings of Ir, Ni, Sn, and O, respectively. Reprinted from Ref. 106 with permission of John Wiley and Sons, copyright (2015). 75
- Figure 41.** Scheme of the oxygen evolution reaction on the IrO_x shell of IrNiO_x core-shell nanoparticles supported on Meso-ATO. Reprinted from Ref. 106 with permission of John Wiley and Sons, copyright (2015). 77
- Figure 42.** a) Cyclic voltammogram of IrNiO_x /Meso-ATO-T annealed at different temperatures, (T = 180, 250, 300, 400, 500 °C), and b) one duty cycle of the durability test under stepwise

- load increase. Reprinted from Ref. 106 with permission of John Wiley and Sons, copyright (2015). 78
- Figure 43.** a) Electrocatalytic oxygen evolution reaction (OER) activities of IrNiO_x core-shell nanoparticles supported on mesoporous ATO (IrNiO_x/Meso-ATO-T), pure Ir supported on carbon (IrO_x/C), and on commercial ATO (IrO_x/com.-ATO) measured using linear sweep voltammetry, b) Ir-mass based activity at $\eta=280\text{mV}$ overpotential of IrO_x/C, IrO_x/com.-ATO, and IrNiO_x/Meso-ATO-T. The temperature at which nanoparticles have been treated is given for each data set. Measurement conditions: 25 °C, 0.05M H₂SO₄, 1600 rpm. The loading of Ir was 10.2 $\mu\text{g cm}^{-2}$. Reprinted from Ref. 106 with permission of John Wiley and Sons, copyright (2015). 79
- Figure 44.** Electrocatalytic OER stability of IrNiO_x core-shell nanoparticles supported on mesoporous ATO (IrNiO_x/Meso-ATO-T), pure Ir supported on carbon (IrO_x/C), and on commercial ATO (IrO_x/com.-ATO) a) Constant current chronopotentiometric stability measurements at a current density of 1 mA cm⁻², and b) Potential at 1 mA cm⁻² using linear sweep voltammetry after duty cycles of IrO_x/C and IrNiO_x/Meso-ATO-T. Temperature at which nanoparticles have been treated is given for each data set. Measurement conditions: 25 °C, 0.05M H₂SO₄, 1600 rpm. The loading of Ir was 10.2 $\mu\text{g cm}^{-2}$. Reprinted from Ref. 106 with permission of John Wiley and Sons, copyright (2015). 80
- Figure 45.** a) High energy X-ray diffraction patterns, and b) the corresponding experimental (black symbols) and model (red lines) atomic pair distribution functions (PDFs) for IrNi_x and IrNiO_x nanoparticles supported on carbon. Radius of first atomic coordination sphere in nanoparticles and refined “lattice parameters” are given by each data set. The pure Ir, precursor alloy, dealloyed, stepwise oxidized, and directly oxidized samples are denoted as pure Ir/C, PA-IrNi_x/C, D-IrNi_x/C, SO-IrNiO_x/C, and DO-IrNiO_x/C, respectively. 84
- Figure 46.** a) High energy X-ray diffraction patterns, and b) corresponding experimental (black symbols) and model (red lines) atomic PDFs for IrNi_x and IrNiO_x nanoparticles supported on ATO. Radius of first atomic coordination sphere in nanoparticles and refined “lattice parameters” are given by each data set. The precursor alloy, dealloyed, stepwise oxidized, and directly oxidized samples are denoted as PA-IrNi_x/ATO, D-IrNi_x/ATO, SO-IrNiO_x/ATO, and DO-IrNiO_x/ATO, respectively. 85
- Figure 47.** Dealloying cyclic voltammograms of a) IrNi_x supported on carbon (IrNi_x/C) and b) IrNi_x supported on ATO (IrNi_x/ATO) from 0.05 to 0.8 V vs. RHE in 0.05 M H₂SO₄, 200 cycles, scan rate 500 mV s⁻¹. The 1st and the 200th CVs are shown to clarify the direction of change during dealloying. Black arrows indicate the irreversible transformation process of ATO. 87
- Figure 48.** Oxidation cyclic voltammograms of a), b) stepwise- and directly oxidized IrNiO_x supported on carbon (denoted as SO-IrNiO_x/C and DO-IrNiO_x/C, respectively), c), d), e) stepwise-, direct, and high potential directly oxidized IrNiO_x supported on ATO (denoted as SO-IrNiO_x/ATO, DO-IrNiO_x/ATO, and HPDO-IrNiO_x/ATO, respectively). The 1st and 50th CVs are shown to clarify the direction of changes during electrochemical oxidation. The arrows indicate according to which y axis the CVs are plotted. f) Comparison of Ir^{III/IV} redox peaks of all oxidized samples. Condition: 0.05M H₂SO₄, a) to e) scan rate of 500 mV s⁻¹, f) scan rate of 20 mV s⁻¹. 88
- Figure 49.** Ir 4f-Ni 3p depth profiles of a) PA-IrNi_x/C, b) IrNiO_x/C -10Cyc, c) IrNiO_x/C-25Cyc, and d) IrNiO_x/C-50Cyc. Vertical dashed lines represent the Ir 4f peak position found in PA-IrNi_x (metallic Ir)..... 91

- Figure 50.** Ir 4f-Ni 3p depth profiles of a) PA-IrNi_x/ATO, b) IrNiO_x/ATO-10Cyc, c) IrNiO_x/ATO-25Cyc, and d) IrNiO_x/ATO-50Cyc. Vertical dashed lines represent the peak position of the metallic Ir 4f signals found in PA-IrNi_x..... 92
- Figure 51.** Ni 2p comparison of PA-IrNi_x, IrNiO_x oxidized at 10, 25, and 50 cycles on a) carbon (denoted as PA-IrNi_x/C, IrNiO_x/C-10Cyc, IrNiO_x/C-25Cyc, and IrNiO_x/C-50Cyc, respectively), and b) ATO support (denoted as PA-IrNi_x/ATO, IrNiO_x/ATO-10Cyc, IrNiO_x/ATO-25Cyc, and IrNiO_x/ATO-50Cyc, respectively). All Ni 2p spectra are area normalized. 93
- Figure 52.** Oxygen evolution reaction (OER) activity of stepwise and directly oxidized IrNiO_x core-shell nanoparticles supported on carbon (denoted as SO-IrNiO_x/C and DO-IrNiO_x/C, respectively), and of stepwise, directly, and high potential directly oxidized IrNiO_x core-shell nanoparticles supported on antimony doped tin oxide (denoted as SO-IrNiO_x/ATO, DO-IrNiO_x/ATO, and HPDO-IrNiO_x/ATO, respectively). a) Linear sweep voltammetry in 0.05M H₂SO₄ at scan rate 5 mV s⁻¹, iR corrected, and b) Ir-mass based activities at 300 mV overpotential, iR- and capacitance corrected. 95
- Figure 53.** Specific activity at 300 mV overpotential of stepwise-, directly-, and high potential directly- oxidized IrNiO_x core-shell nanoparticles supported on antimony doped tin oxide (denoted as SO-IrNiO_x/ATO, DO-IrNiO_x/ATO, and HPDO-IrNiO_x/ATO, respectively). The specific activity at 300 mV overpotential of directly oxidized IrO_x supported on ATO (DO-IrO_x) was included as a benchmark. 96
- Figure 54.** OER activity of a) directly oxidized IrNiO_x supported on carbon after 10, 25 and 50 cycles (denoted as IrNiO_x/C-10Cyc, IrNiO_x/C-25Cyc, and IrNiO_x/C-50Cyc, respectively), and b) high potential directly oxidized IrNiO_x supported on antimony doped tin oxide after 10, 25 and 50 cycles (denoted as IrNiO_x/ATO-10Cyc, IrNiO_x/ATO-25Cyc, and IrNiO_x/ATO-50Cyc, respectively). The measurements were performed in 0.05M H₂SO₄ at a scan rate of 5 mV s⁻¹ and were iR corrected. Ir loading 10.2 μg cm⁻². 97
- Figure 55.** Relation between nominal and actual Ni content (molar %) in IrNi_x nanoparticles supported on mesoporous ATO (PA-IrNi_x/Meso-ATO) and on carbon (PA-IrNi_x/C)..... 100
- Figure 56.** a) XRD patterns of IrNi_x nanoparticles (x = 0.28, 1.2, 2.6, 3.3, and 6.8) supported on mesoporous ATO (PA-IrNi_x/Meso-ATO), and b) a zoom on reflections between 40 ° and 45 ° 2θ. Black and red vertical dashed lines indicate database (111) reflections of pure Ir and pure Ni, respectively. 101
- Figure 57.** The relationship between interplane distance of (111) planes (d₍₁₁₁₎) and Ni content (red symbols) of a) mesoporous ATO supported IrNi_x nanoparticles (x = 0.28, 1.2, 2.6, 3.3, and 6.8) (denoted as PA-IrNi_x/Meso-ATO), and b) carbon supported IrNi_x nanoparticles (x = 0, 2.3, 3.3, and 5.7) (denoted as PA-IrNi_x/C) compared to Vegard's rule (dashed lines)..... 101
- Figure 58.** Ir 4f Ni 3p XPS depth profiles of precursor alloy IrNi_x nanoparticles supported on mesoporous ATO (PA-IrNi_x/Meso-ATO). a) PA-IrNi_{1.2}/Meso-ATO, b) PA-IrNi_{2.6}/Meso-ATO, c) PA-IrNi_{3.3}/Meso-ATO, and d) PA-IrNi_{6.8}/Meso-ATO. Vertical dashed lines indicate peak position of metallic Ir. 102
- Figure 59.** a) Ni 2p XPS comparison of the precursor alloy IrNi_x nanoparticles supported on mesoporous antimony doped tin oxide (PA-IrNi_x/Meso-ATO). All Ni 2p spectra are area normalized. b) Sn 3d comparison of PA-IrNi_{6.8}/Meso-ATO in a fresh beam spot and after longer irradiation. 103

- Figure 60.** Cyclic voltammograms from 0.4 to 1.4 V vs. RHE at scan rate 20 mV s^{-1} of oxidized IrNi_x nanoparticles supported on mesoporous antimony doped tin oxide ($\text{Ox-IrNi}_x/\text{Meso-ATO}$, x represents molar ratio of Ni in the corresponding precursor alloys, $x = 1.2, 2.6, 3.3,$ and 6.8). Conditions: $0.05\text{M H}_2\text{SO}_4$, Ir loading $10.2 \mu\text{g cm}^{-2}$ 105
- Figure 61.** Meso-ATO corrected charge of $\text{Ox-IrNi}_x/\text{Meso-ATO}$ ($x = 1.2, 2.6, 3.3,$ and 6.8) samples as function of the initial Ni content in the corresponding precursor alloys. Charge of the pure oxidized Ir supported on Meso-ATO is shown as the 0% Ni benchmark. Conditions: $0.05\text{M H}_2\text{SO}_4$, Ir loading $10.2 \mu\text{g cm}^{-2}$ 107
- Figure 62.** Ir 4f-Ni 3p XPS depth profiles of oxidized IrNi_x nanoparticles supported on mesoporous antimony doped tin oxide ($\text{Ox-IrNi}_x/\text{Meso-ATO}$). a) $\text{Ox-IrNi}_{1.2}/\text{Meso-ATO}$, b) $\text{Ox-IrNi}_{2.6}/\text{Meso-ATO}$, c) $\text{Ox-IrNi}_{3.3}/\text{Meso-ATO}$, and d) $\text{Ox-IrNi}_{6.8}/\text{Meso-ATO}$. In black fresh beam spot spectra are shown. In cyan spectra (550 eV KE) are overlaid recorded after longer irradiation. Vertical dashed lines indicate peak position of metallic Ir 108
- Figure 63.** Ni 2p comparison of electrochemical oxidized IrNi_x nanoparticles supported on mesoporous antimony doped tin oxide ($\text{Ox-IrNi}_x/\text{Meso-ATO}$). All Ni 2p spectra are area normalized. b) Sn 3d comparison of oxidized $\text{Ox-IrNi}_{6.8}/\text{Meso-ATO}$ in a fresh beam spot and after longer irradiation. 110
- Figure 64.** Ir 4f-Ni 3p depth profiles of OER tested samples a) $\text{IrNi}_{3.3}/\text{Meso-ATO-OER}$ and b) $\text{IrNi}_{6.8}/\text{Meso-ATO-OER}$. In black fresh beam spot spectra are shown. In cyan spectra (550 eV KE) are overlaid recorded after longer irradiation. Vertical dashed lines indicate peak position of metallic Ir 111
- Figure 65.** XPS Ni 2p comparison of samples after OER ($\text{IrNi}_{3.3}/\text{Meso-ATO-OER}$ and $\text{IrNi}_{6.8}/\text{Meso-ATO-OER}$). All Ni 2p spectra are area normalized. 112
- Figure 66.** a) Electrocatalytic oxygen evolution reaction (OER) activities of mesoporous ATO supported oxidized IrNi_x core-shell nanoparticles ($\text{Ox-IrNi}_x/\text{Meso-ATO}$) prepared from precursor alloy $\text{IrNi}_x/\text{Meso-ATO}$, and pure oxidized IrO_x nanoparticles ($\text{IrO}_x/\text{Meso-ATO}$, Pure Ir) measured using linear sweep voltammetry, b) Ir-mass based activity at $\eta=300\text{mV}$ overpotential of $\text{IrO}_x/\text{Meso-ATO}$, and $\text{Ox-IrNi}_x/\text{Meso-ATO}$ as a function of the initial Ni content in the corresponding precursor alloy. Measurement conditions: $25 \text{ }^\circ\text{C}$, $0.05\text{M H}_2\text{SO}_4$, 1600 rpm . The loading of Ir was $10.2 \mu\text{g cm}^{-2}$ 113
- Figure 67.** Specific activities (j_{specific}) at 300 mV overpotential of electrochemical oxidized IrNi_x nanoparticles supported on mesoporous ATO as a function of the initial Ni content in the corresponding precursor alloy 114
- Figure 68.** Stability tests at a current density of 1 mA cm^{-2} of electrochemical oxidized IrNi_x core-shell nanoparticles supported on carbon and mesoporous antimony doped tin oxide (referred to as IrNiO_x/C and $\text{Ox-IrNi}_x/\text{Meso-ATO}$, respectively) compared to pure IrO_x supported on carbon (referred to as IrO_x/C). Measurement conditions: $25 \text{ }^\circ\text{C}$, $0.05\text{M H}_2\text{SO}_4$, 1600 rpm . The loading of Ir was $10.2 \mu\text{g cm}^{-2}$ 115

List of Tables

Table 1. Actual Ir : Ni ratios and Ir weight loadings derived from ICP-OES of samples synthesized by different methods compared to the nominal compositions	36
Table 2. Actual Ir : Ni ratios and Ir weight loadings derived from ICP-OES measurements of IrNi _x /C-200, IrNi _x /C-220, and IrNi _x /C-240 compared to the nominal compositions.....	38
Table 3. Actual Ir : Ni ratios and Ir weight loadings derived from ICP-OES of IrNi _x -DCB, IrNi _x -NMP, and IrNi _x -DMA compared to nominal compositions.	39
Table 4. Atomic composition of supported pure Ir and IrNi _x materials and their XRD, TEM based crystallite and particle size analysis.....	48
Table 5. Quantitative XPS results of IrNi _x series (x = 2.3, 3.3, and 5.7): precursor alloy (PA-IrNi _x), stepwise oxidized (SO-IrNi _x) and directly oxidized (DO-IrNi _x) measured in UHV at kinetic energy 550 eV.....	61
Table 6. Ir loadings (wt. %), bulk composition (molar ratios) derived from ICP-OES and surface composition (molar ratios) derived from XPS (photoelectron kinetic energy: 550 eV) of PA-IrNi _x /Meso-ATO-T annealed at different temperatures and IrNiO _x /Meso-ATO-180 prepared from PA-IrNi _x /Meso-ATO-180.....	71
Table 7. Quantitative XPS results (molar ratios) of PA-IrNi _x /C and IrNiO _x /C series samples. KE: 550 eV.....	94
Table 8. Quantitative XPS results (molar ratios) of PA-IrNi _x /ATO and IrNiO _x /ATO series samples. KE: 550 eV.....	94
Table 9. Nominal and actual atomic compositions derived from ICP-OES of PA-IrNi _x /Meso-ATO samples.....	99
Table 10. Quantitative XPS results of PA-IrNi _x /Meso-ATO samples. KE: 550 eV. Molar ratios are shown.....	104
Table 11. Charge contribution of Meso-ATO in each sample calculated from mass of Meso-ATO on electrode and a charge density of 0.01025 mC μg ⁻¹ _{Meso-ATO}	106
Table 12. Quantitative XPS results of Ox-IrNi _x /Meso-ATO samples. KE: 550 eV. Molar ratios are shown.....	110
Table 13. Quantitative XPS results of OER treated IrNi _x /Meso-ATO samples. KE: 550 eV. Molar ratios are shown.....	112